



THE HONG KONG
POLYTECHNIC UNIVERSITY

香港理工大學

Pao Yue-kong Library

包玉剛圖書館

Copyright Undertaking

This thesis is protected by copyright, with all rights reserved.

By reading and using the thesis, the reader understands and agrees to the following terms:

1. The reader will abide by the rules and legal ordinances governing copyright regarding the use of the thesis.
2. The reader will use the thesis for the purpose of research or private study only and not for distribution or further reproduction or any other purpose.
3. The reader agrees to indemnify and hold the University harmless from and against any loss, damage, cost, liability or expenses arising from copyright infringement or unauthorized usage.

IMPORTANT

If you have reasons to believe that any materials in this thesis are deemed not suitable to be distributed in this form, or a copyright owner having difficulty with the material being included in our database, please contact lbsys@polyu.edu.hk providing details. The Library will look into your claim and consider taking remedial action upon receipt of the written requests.

**ANALYSIS OF HEAT TRANSFER IN A BUILDING
STRUCTURE ACCOUNTING FOR THE
REALISTIC EFFECT OF THERMAL RADIATION
HEAT TRANSFER**

TAM WAI CHEONG

Ph.D

THE HONG KONG POLYTECHNIC UNIVERSITY

2014

The Hong Kong Polytechnic University

Department of Mechanical Engineering

**ANALYSIS OF HEAT TRANSFER IN A BUILDING
STRUCTURE ACCOUNTING FOR THE
REALISTIC EFFECT OF THERMAL RADIATION
HEAT TRANSFER**

TAM WAI CHEONG

A thesis
submitted in partial fulfillment of the requirements for
the degree of Doctor of Philosophy

June 2013

CERTIFICATE OF ORIGINALITY

I hereby declare that this thesis is my own work and that, to the best of my knowledge and belief, it reproduces no material previously published or written nor material which has been accepted for the award of any other degree or diploma, except where due acknowledgement has been made in the text.

(Signed)

TAM Wai Cheong (Name of student)

To my parents,
Shek-Non Tam and Wai-Kuen Li
and my grandparents,
Siu-Chi Tam and Siu-Kuen Lok, and Wei-Guang Li and Rui-Mei Wu.

Abstract

A computer code BERHT (Building Energy with Radiative Heat Transfer) is developed to simulate the effect of heat and mass transfer in a building structure. The code uses many of the programming structure of a well-known whole-building energy analysis code, ENERGY-PLUS. A realistic model for interior longwave radiative heat transfer is implemented. The model accounts for the absorption/emission of participating species (CO_2 , H_2O , and small particles) in a building environment and the geometric effect of a building structure. Spectroscopic data from RADCAL, a narrow band model, is used to simulate the absorption effect of the two participating gases. Neural network is utilized to provide accurate and efficient correlations which can be readily implemented in a heat and mass transfer calculation for a three-dimensional building structure.

A series of numerical studies for a single room building structure are conducted. Numerical data are generated. For nominal concentration of CO_2 , H_2O , and small particles, results show that the presence of an absorbing/emitting medium has important effects on the distribution of the total heat transfer between convection and radiation. The presence of a participating medium, however, has only a minimal effect on the overall heat transfer and the temperature of the interior air. It is shown that the overall energy balance is strongly influenced by external parameters. The “greenhouse” effect is simulated numerically. Results confirm that the absorption of short-wave radiation by

the surface and the subsequent heat transfer from the surface to the air mixture in the room is the primary mechanism for the greenhouse effect.

To study the effect of radiation in a higher temperature environment, a computer code FRTF-RAD (Fire Resistance Test Furnace with Radiation) is developed. The radiative heat transfer in a fire resistance test furnace is simulated. Results show that emission and reflection from the wall boundaries have major effects on the radiative heat flux measurement in a test sample. The data which demonstrated the scalability of the test furnaces are shown to be limited to isothermal furnaces only. From the perspective of a compartment fire, numerical data also shows that particle emission and emission from the wall are essential in the initiation of flashover.

Acknowledgements

I would like to express my heartfelt gratitude to my chief supervisor, Professor Walter W. Yuen, for his continuous guidance, encouragement, care, support, and patience throughout my entire graduate study. Professor Yuen is not only the advisor of mine, but also the turning-point of my life. He is one of the most important persons in my life. Without him, I may end up in a completely different path.

I am grateful to my co-supervisors, Professor W.K. Chow and Professor C.W. Leung, for their support and advice over the years.

In addition, a thank you to my dearest friends: JCACKS (Jun Tham, Corey Jia, Charles He, my love one (Kiki Wu), and Sheena Wang), it is wonderful to have you in my life at HKPU.

Finally and most importantly, I would like to sincerely thank my parents and family for their unconditional love, support, and tolerance.

My thesis would not have been possible without having these people in my life. I truthfully appreciate them.

Table of Contents

Dedication	i
Abstract	iii
Acknowledgements	v
Table of Contents	vii
List of Tables	x
List of Figures	xi
Nomenclature	xv
Chapter 1: Introduction	1
Chapter 2: RAD-NETT and its Implementation in a Rectangular Enclosure	5
2.1: Mathematical Formulation	5
2.2: Radiative Properties of a CO ₂ /H ₂ O/small particles Mixture	12
Chapter 3: BERHT – A Thermal Building Energy Program with Radiative Heat Transfer	15
3.1: Introduction	15
3.2: Mathematical Formulation	16
3.2.1: Energy balance	16
3.2.1a: Opaque Wall Surfaces	17
3.2.1b: Glazing Surface	25
3.2.2: Mass Balance	27
3.3: Results	31
3.3.1: Benchmarking Cases	31
3.3.2: Effect of Participating Medium	34

Chapter 4: Analysis of Heat Transfer in a Fire Resistance Test Furnace	43
4.1: Analysis and Results	44
Chapter 5: Conclusions	49
Reference	R-1
Tables	T-1
Figures	F-1
Appendix A: Neural Network Correlation for the Evaluation of Mean Beam Lengths for Radiative Heat Transfer Between Perpendicular Surfaces in a Rectangular Enclosure	A-1
List of Tables (Appendix A)	A-3
Tables	A-7
List of Figures (Appendix A)	A-43
Figures	A-44
Appendix B: Model Description for BERHT	B-1
B.1: Solar Gains	B-1
B.1.1: Solar Geometry	B-1
B.1.2: Shortwave Solar Incidence	B-4
B.1.2a: Beam Solar Incidence	B-5
B.1.2b: Sky Diffuse Solar Incidence	B-6
B.1.2c: Ground Reflected Diffuse Solar Incidence	B-8
B.1.2d: Solar Gain for Exterior Surfaces	B-9
B.1.3: Solar Gain for Exterior Surfaces	B-9
B.1.4: Solar Gain for Interior Surfaces	B-10
B.1.4a: Optical Properties for Glazing	B-11
B.1.4b: Transmitted Solar Radiation	B-13

B.2: Climate Condition	B-15
B.2.1: Drybulb Temperature	B-15
B.2.2: Sky Temperature	B-15
B.2.3: Ground Temperature	B-16
B.2.4: Local Wind Speed	B-16
B.3: Building Thermal Models	B-16
B.3.1: Conduction in Opaque Surfaces	B-16
B.3.2: Convective Heat Transfer for Exterior Surfaces	B-17
B.3.3: Convective Heat Transfer for Interior Surfaces	B-19
B.3.4: Radiative Heat Transfer On Exterior Surfaces	B-20
List of Tables (Appendix B)	B-23
Tables	B-24
List of Figures (Appendix B)	B-27
Figures	B-28

List of Tables

Table 2.1: The geometry and area identification used in the model for a fire resistance test furnace	T-1
Table 3.1: Site Information and Location	T-2
Table 3.2: Site Weather conditions	T-3
Table 3.3: Dimension of Building Enclosure	T-4
Table 3.4: Construction of building envelopes	T-5
Table 3.5: Construction material properties	T-6
Table 3.6: Window Optical Properties in Case 1.....	T-7
Table 3.7: Window Optical Properties in Case 2.....	T-8

List of Figures

Figure 2.1: Geometry of building enclosure	F-1
Figure 2.2: The mixture mean beam length for perpendicular areas for the considered fire resistance test furnace for small and moderate mixture optical thicknesses	F-1
Figure 2.3: The emissivity of the mixture for the considered fire resistance test furnace with black surrounding wall	F-2
Figure 2.4a: Effective of wall emissivity on the mixture emissivity in the considered fire resistance test furnace for a pure gas mixture	F-3
Figure 2.4b: Effective of wall emissivity on the mixture emissivity in the considered fire resistance test furnace for a gas-particle mixture	F-3
Figure 2.5a: The absorptivity of the mixture for the considered fire resistance test furnace at different wall temperature (the emissivity of the mixture is also shown in the figure for comparison)	F-4
Figure 2.5b: The absorptivity of a gas-particle mixture for the considered fire resistance test furnace at different wall temperature (the emissivity of the mixture is also shown in the figure for comparison)	F-4
Figure 3.1: Geometry of building enclosure	F-5
Figure 3.2: Comparison of total absorbed shortwave solar radiation (BERHT and Eplus) for different exterior surfaces in benchmark case 1	F-6
Figure 3.3: Comparison of exterior surface temperatures (BERHT and Eplus) for benchmark case 1.....	F-6
Figure 3.4: Comparison of interior surface temperatures (BERHT and Eplus) for benchmark case 1	F-7
Figure 3.5: Comparison of zone air temperature (BERTHT and Eplus) for benchmark case 1	F-7

Figure 3.6: Comparison of total absorbed shortwave solar radiation (BERHT and Eplus) for different exterior surfaces in benchmark case 2.....	F-8
Figure 3.7: Comparison of total absorbed shortwave solar radiation (BERHT and Eplus) for different interior surfaces in benchmark case 2	F-8
Figure 3.8: Comparison of exterior surface temperatures (BERHT and Eplus) for benchmark case 2	F-9
Figure 3.9: Comparison of interior surface temperatures (BERHT and Eplus) for benchmark case 2	F-9
Figure 3.10: Comparison of zone air temperature (BERHT and Eplus) for benchmark case 2	F-10
Figure 3.11a: Heat transfer (radiation, convection, and total) between surfaces and case 1 with room air with an absorbing/emitting gas/particle for mixture different emissivity	F-11
Figure 3.11b: Heat transfer (radiation, convection and total) between surfaces and room air with an absorbing/emitting gas mixture only for case 1 with different emissivity	F-11
Figure 3.11c: Heat transfer (radiation, convection and total) between surfaces and room air with a transparent medium for case 1 with different emissivity	F-12
Figure 3.12: Temperature of the air within the room for the three modes of radiative absorption for case 1 with different emissivity	F-12
Figure 3.13a: Total heat transfer to the zone air for different level of convection heat transfer with different emissivity	F-13
Figure 3.13b: Temperature of the zone air for different level of convection heat transfer with different emissivity	F-13
Figure 3.14: Convective heat transfer coefficients to the different surfaces for the case with normal convection and increased convection (by a factor of 2).....	F-14
Figure 3.15a: Heat transfer (radiation, convection and total) between surfaces and room air with an absorbing/emitting gas/particle mixture for case 1 with reduced convection (1/10) and different emissivity	F-15

Figure 3.15b: Heat transfer (radiation, convection and total) between surfaces and room air with an absorbing/emitting gas mixture only for case 1 with reduced convection (1/10) and different emissivity	F-15
Figure 3.15c: Heat transfer (radiation, convection and total) between surfaces and room air with a transparent medium for case 1 with reduced convection (1/10) and different emissivity	F-16
Figure 3.16: Temperature of the air within the room for the three modes of radiative absorption for case 1 with reduced convection (1/10) and different emissivity	F-16
Figure 3.17a: Heat transfer (radiation, convection and total) between surfaces and room air with an absorbing/emitting gas/particle mixture for case 1 with reduced convection (1/100) and different emissivity	F-17
Figure 3.17b: Heat transfer (radiation, convection and total) between surfaces and room air with an absorbing/emitting gas mixture only for case 1 with reduced convection (1/100) and different emissivity	F-17
Figure 3.17c: Heat transfer (radiation, convection and total) between surfaces and room air with a transparent medium for case 1 with reduced convection (1/100) and different emissivity	F-18
Figure 3.18: Temperature of the air within the room for the three modes of radiative absorption for case 1 with reduced convection (1/100) and different emissivity	F-18
Figure 3.19: Heat transfer to the zone air and the air temperature within the room for the three modes of radiative absorption for case 1 with $\epsilon_{\text{floor}} = 0.9$ and $\epsilon_{\text{other-surfaces}} = 0.1$	F-19
Figure 3.20: Heat transfer (radiation, convection and total) between surfaces and room air with the two absorbing/emitting mixtures for case with $\epsilon_{\text{floor}} = 0.9$ and $\epsilon_{\text{other-surfaces}} = 0.1$	F-19
Figure 3.21: Comparison of the temperature at the difference surfaces and the zone air temperature for cases with different emissivity, transparent vs. absorbing/emitting mixtures	F-20
Figure 3.22: Comparison of the convective and radiative heat transfer from the difference surfaces to the zone air temperature for cases with different emissivity with an absorbing/emitting mixture	F-21

Figure 3.23: Heat transfer (radiation, convection and total) between surfaces and room air with transparent medium for the reference case with different emissivity	F-22
Figure 3.24a: Heat transfer (radiation, convection and total) between surfaces and room air with transparent medium for different emissivity	F-22
Figure 3.24b: Heat transfer (radiation, convection and total) between surfaces and room air with an absorbing/emitting gas mixture only for different emissivity	F-23
Figure 3.24c: Heat transfer (radiation, convection and total) between surfaces and room air with an absorbing/emitting gas/particle mixture for different emissivity	F-23
Figure 3.25: Temperature of the air within the room for the reference case and the three modes of radiative heat transfer with different emissivity	F-24
Figure 4.1: Comparison between the measured furnace temperature and the ASTM E119 time-temperature curve used in the calculation	F-25
Figure 4.2: Comparison between the measured heat flux to the test specimen at the full-scale fire resistance furnace and the predicted radiative heat flux from the emission of combustion products only	F-25
Figure 4.3a: Prediction of heat flux from the different walls and the heat flux from the combustion mixture to the test specimen with $f_v = 0.0$. The wall temperature is assumed to be identical to the temperature of the mixture	F-26
Figure 4.3b: Prediction of heat flux from the different walls and the heat flux from the combustion mixture to the test specimen with $f_v = 5.0e-8$. The wall temperature is assumed to be identical to the temperature of the mixture	F-26

Nomenclature

Symbols

\vec{a}^i	Output vector of the i th layer of the neural network ($i = 1, 2, 3$)
A_i	Area of i th surface in the building structure [m^2]
A_s	Apparent solar irradiation [W/m^2]
A_{g,θ_g}	Angular absorptivity for glazing
AST	Solar time [min]
\vec{b}^i	Bias vector of the i th layer of the neural network ($i = 1, 2, 3$)
B_s	Atmospheric extinction coefficient
c_p	Specific heat [$\text{J}/\text{kg}\cdot\text{K}$]
C_s	Diffuse radiation factor
C_{soot}	Concentration of small particles [ppm-m]
C_z	Concentration of carbon dioxide [ppm-m]
d_g	Glazing thickness [m]
E_i	Longwave radiation flux incident on window [W/m^2]
ET	Equation of time [min]
f_v	Volume fraction of small particles
F_{air}	Air-to-surface view factor

F_{gnd}	Ground-to-surface view factor
F_{sky}	Sky-to-surface view factor
F_{CO_2}	Fraction of carbon dioxide
F_{ij}	View factor between i th surface and j th surface ($i = j = 1, 2, \dots, 6$)
$G_{i,j}$	Brightening coefficient factors
$GMTD$	Time difference between local site and Greenwich Mean Time [hour]
h_c	Convective heat transfer coefficient [W/m^2-K]
h_f	Forced convection component of convective heat transfer coefficient [W/m^2-K]
h_n	Natural convection component of convective heat transfer coefficient [W/m^2-K]
$h_{r,air}$	Linearized radiative heat transfer coefficient for air temperature [W/m^2-K]
$h_{r,sky}$	Linearized radiative heat transfer coefficient for sky temperature [W/m^2-K]
$h_{r,gnd}$	Linearized radiative heat transfer coefficient for ground temperature [W/m^2-K]
H_{angle}	Hour angle [deg]
I_E	Extraterrestrial irradiance [W/m^2]
$I_{Hori IR}$	Horizontal infrared radiation intensity [W/m^2]
k	Conductivity [$W/m-K$]
L	Path length [m]

$L_{c,ij}$	Center-to-center distance between area A_i and A_j in a the building structure [m]
$L_{m,ij}$	Gas-mixture mean beam length for average transmissivity between area A_i and A_j in a the building structure [m]
$L_{s,ij}$	Small particles mean beam length for average transmissivity A_i and A_j between area in a the building structure [m]
LON	Longitude of site [deg]
LST	Local standard time [min]
\dot{m}_{inf}	Mass flow rate due to infiltration [kg/s]
$m_{s,air}$	Relative air mass
n	Index of refraction
N_{day}	Number of day
N_{sl}	Total number of zone in the building structure
N_{surf}	Total number of surface in the building structure
\vec{p}_j	Input vector of the neural network
P	Partial pressure [kPa]
P_{CO_2}	Partial pressure of carbon dioxide [kPa]
P_g	Partial pressure of the CO ₂ /H ₂ O mixture [kPa]
P_{H_2O}	Partial pressure of water vapor [kPa]
q''_{beam}	Beam solar radiation [W/m ²]

q''_{gnd}	Ground reflected solar radiation [W/m ²]
$q''_{i,c}$	Convection flux on interior surfaces [W/m ²]
$q''_{int,beam}$	Transmitted-beam-solar radiation absorbed by interior surface [W/m ²]
$q''_{int,dif}$	Transmitted-diffuse-solar radiation absorbed by interior surface [W/m ²]
$q''_{int,ref}$	Total reflected transmitted-solar-radiation absorbed by interior surface [W/m ²]
q''_{ki}	Conduction flux for interior surfaces [W/m ²]
q''_{lwx}	Interior longwave radiative flux exchange between surfaces [W/m ²]
$q''_{o,c}$	Convection flux for exterior surfaces [W/m ²]
$q''_{o,lr}$	Exterior longwave radiative heat flux between surfaces and the surroundings [W/m ²]
$q''_{o,s}$	Solar gain for exterior surfaces [W/m ²]
q''_{ref}	Total reflected transmitted-solar-radiation absorbed [W/m ²]
q''_{sky}	Diffuse sky solar radiation [W/m ²]
q''_{sol}	Total solar gain for an interior surface [W/m ²]
$q''_{sources}$	Internal gains [W/m ²]
$q''_{s,beam}$	Beam solar incidence [W/m ²]
$q''_{s,gnd}$	Ground reflected solar incidence [W/m ²]
$q''_{s,sky}$	Diffuse sky incidence [W/m ²]

$q''_{s,tot}$	Total incident solar radiation on building exterior surface [W/m ²]
$q''_{ts,beam}$	Transmitted beam solar radiation [W/m ²]
$q''_{ts,dif}$	Transmitted diffuse solar radiation [W/m ²]
q_i	Heat flux to <i>i</i> th surface in the building structure [W/m ²]
Q_c	Total convective heat transfer [W]
Q_c	Heat transfer to the <i>i</i> th surface in building structure [W]
Q_{loads}	Convective internal loads [W]
Q_g	Heat transfer to the medium in the building structure [W]
Q_{sys}	Air system output [W]
R_f	Surface roughness
R_{g,θ_g}	Glazing angular reflectance
$R_{g,\cup}$	Glazing hemispherical reflectance
$R_{s,circumsolar}$	Circumsolar radiation
$R_{s,dome}$	Sky dome radiation
$R_{s,horizon}$	Horizon radiation
S_i	Number of neurons in the <i>i</i> th layer of the neural network (<i>i</i> = 1, 2, 3)
$S_{g,i}$	Radiation flux (shortwave, and longwave from other internal sources) absorbed by face <i>i</i> [W/m ²]

$S_i S_j$	Neural network exchange factors between area A_i and A_j in the building structure
t	Time [s]
T_{air}	Temperature air [$^{\circ}\text{C}$]
T_{db}	Dry-bulb temperature [$^{\circ}\text{C}$]
T_g	Temperature of medium [$^{\circ}\text{C}$]
T_{g,θ_g}	Angular transmittance for glazing
$T_{g,\cup}$	Hemispherical transmittance for glazing
T_{gnd}	Temperature of ground [$^{\circ}\text{C}$]
T_i	Interior surface temperature [$^{\circ}\text{C}$]
T_{max}	Maximum temperature of the design day [$^{\circ}\text{C}$]
$T_{multiplier}$	Temperature range multiplier
T_o	Exterior surface temperature [$^{\circ}\text{C}$]
T_{range}	Temperature range of the design day
T_{sky}	Temperature of sky [$^{\circ}\text{C}$]
T_z	Zone air temperature [$^{\circ}\text{C}$]
V_{met}	Measured wind speed from the meteorological station [m/s]
V_z	Local wind speed [m/s]
\tilde{W}^i	Weighted matrix of the i th layer of the neural network ($i = 1, 2, 3$)

W_{dir}	Wind direction
W_f	Wind modification multiplier
W_z	Humidity ratio of zone air [kg/kg]
X	Dimension of the building structure [m]
X_{CFT}	Conduction transfer function coefficients (outside)
Y	Dimension of the building structure [m]
Y_{CFT}	Conduction transfer function coefficients (cross)
z_{met}	Height of the meteorological station [m]
z_v	Height of the site [m]
Z	Dimension of the building structure [m]
Z_{CFT}	Conduction transfer function coefficients (inside)

Greek

α	Absorptivity
α_g	Absorptivity of gas-mixture
α_{met}	Wind speed profile exponent at the meteorological station
α_s	Absorptivity of small particles
α_{sol}	Solar absorptivity of building surface
α_{ij}	Average absorptivity between surfaces A_i and A_j for the building structure

α_v	Wind speed profile exponent at site
$\Delta\alpha$	Excess absorptivity
β_s	Elevation angle [deg]
δ_{met}	Wind speed profile boundary layer thickness at the meteorological station [m]
δ_s	Declination angle of sun [deg]
δ_v	Wind speed profile boundary layer thickness at site [m]
ε_i	Emissivity of building surface
ε_g	Emissivity of gas-mixture
ε_s	Sky clearness factor
ϕ_s	Solar azimuth angle [deg]
φ_s	Solar azimuth angle [deg]
κ_λ	Extinction coefficient
λ	Wavelength [μm]
$\theta_{g,i}$	Temperature of <i>i</i> th glass face [$^{\circ}\text{C}$]
θ_s	Angle of incidence [deg]
ρ_{air}	Density of air [kg/m^3]
ρ_C	Density of pure carbon [kg/m^3]
ρ_{g,θ_g}	Angular reflectivity for glazing
$\rho_{s,gnd}$	Ground reflectivity

σ	Stefan Boltzman constant [W/m ⁴ -K]
τ_{ij}	Average transmissivity between surfaces A _i and A _j in the building structure
τ_{g,θ_g}	Angular transmissivity for glazing
Δ_s	Sky brightness factor
$\Phi_{CFT,j}$	Conduction transfer function coefficient (flux history term)
Σ	Tilted angle of surface [deg]
Ω_{sd}	Distribution factor
Ω_{sf}	Fraction of beam radiation absorbed by floor surface
Ψ_s	Surface azimuth angle [deg]
\forall_z	Volume of zone [m ³]

Chapter 1: Introduction

In modeling of heat transfer within a building structure, the effect of radiative heat transfer in a participating medium is important because of the presence of the absorbing gaseous species (CO_2 and H_2O) and small particles. However, due to the mathematical complexity in modeling the effect realistically in a three-dimensional building structure, the importance of radiative heat transfer in the energy analysis of a building environment is not well understood. In this thesis, the realistic effect of radiative heat transfer is implemented in two applications of energy analysis in building structure. In the first application, a computer code BERHT (Building Energy with Radiative Heat Transfer) is developed to simulate the effect of radiation in a low temperature (i.e. room temperature) building structure environment. In the second application, a computer code FRTF-RAD (Fire Resistance Test Furnace with Radiation) is developed to simulate the effect of radiative heat transfer in a high temperature combustion environment.

Improving energy efficiency in buildings has been identified as a key step by many nations, including the United States and China, in achieving the goal of energy efficiency and the reduction of greenhouse gas (CO_2 , CH_4 , NO_2 , etc) emissions. In the U.S., building sector accounts for 40% of the total energy consumption (Lombard et al., 2008). In China, this figure is about 23% (Liang et al., 2008). These statistics indicate a vital need to improve building energy performance and a great deal of efforts have been

reported in developing computational tools for effective simulation for building energy transport (Torcellini et al., 2004).

While many building energy simulation programs have been developed over the past decades (BLAST, DeST, DOE-2, ECOTECT, IES <VE>, EnergyPlus, TAS, and TRNSYS) and many of them have implemented highly sophisticated models for conductive and convective heat transfer (e.g. transient conduction model for composite walls in EnergyPlus), the modeling of radiative heat transfer has largely been treated in a highly simplified and ad-hoc level with uncertain accuracy. For example, in DeST (DeST, 2002), DOE-2 (LBNL, 1982), ECOTECT (Taylor, 2002), and TRNSYS (Trnsys, 2012), radiative heat flux is represented by a linearized effective heat transfer coefficient and the view factor is evaluated approximately by an area ratio. In TAS (TAS, 2010) and IES <VE> (IES, 2011), radiative heat transfer is modeled by a mean radiant temperature (MRT) model with a coupling coefficient. The exact view factor is used while the effect of grey surfaces is accounted for by the Oppenheim surface resistance concept (Oppenheim, 1956). In EnergyPlus (EPlus, 2011), a net radiation method is implemented to account for the effect of diffuse gray surfaces. However, in all of these existing models, except for IES <VE> in which the emissivity of the medium is simulated by an empirical correlation, the effect of the absorbing medium (CO_2 , H_2O and small particles) are completely neglected (the medium is treated as transparent) due to the assumption of low concentration in participating components and their short mean path length (EPlus, 2011).

The lack of motivation in developing a more realistic radiative transfer model in building energy simulation programs is driven by the general expectation that at low temperatures, the effect of radiation is not significant compared to convection in a building structure. But, there has been no rigorous verification of this expectation, particularly in view of the uncertain accuracy of the radiation model in the existing building energy simulation programs. With the development of RAD-NETT (which will be described in detail in Chapter 2), it is now computationally feasible to simulate the realistic effect of radiative absorption/emission for common gases and small particles. In this thesis, a building energy simulation computer code (BERHT) is developed using RAD-NETT to simulate the radiative heat transfer. The importance of the radiative heat transfer in different scenarios will be identified computationally and discussed.

In high temperature applications for heat transfer simulation in a building structure such as a compartment fire, the current approach used in the modeling of radiative heat transfer is also relatively ad-hoc and simplistic. In the commonly used zonal model for fire safety consideration such as CCFM (Cooper and Forney, 1990), FASTLite (Portier et al., 1996), and CFAST (Jones et al., 2005) and the modeling of heat transfer in fire resistance test furnace (Harmathy, 1981; Sultan et al., 1986), for example, the effect of the absorbing gas is simulated by an empirical gray absorption coefficient assigned by the user. While radiative heat transfer is acknowledged to be important in these high temperature applications, it is still difficult, if not impossible, to make definitive and quantitative conclusions about the effect due to the uncertain accuracy of the radiation

model used in the simulation. With RAD-NETT, it is now possible to simulate the realistic effect of radiative heat transfer in these high temperature applications. Since heat transfer data for some fire resistance furnaces are available in the literature (Sultan et al., 2003), a computer code, FRTF-RAD, is developed to simulate the radiative heat transfer in a fire resistance testing furnace. Based on numerical data, the relevant radiative heat transfer mechanisms in a compartment fire environment will be identified.

The remainder of this thesis is organized into four chapters. In Chapter 2, the implementation of RAD-NETT in a rectangular geometry is presented. The neural network representation of the relevant exchange factors is formulated and the numerical data for network elements are generated. A net-radiation model, which accounts for all the non-gray effect of the absorbing medium, for an enclosure with diffuse reflecting boundaries is developed. In Chapter 3, the development of BERHT is described. The basic structure of the code will follow that of Energy-Plus. Simulation of a one-room building structure will be presented to illustrate the importance of radiative heat transfer in different scenarios. In Chapter 4, the development of FRTF-RAD is described. By comparison with data generated from a full scale test furnace, the relevant heat transfer mechanisms in a fire test resistance test furnace are identified. Finally, conclusions are presented in Chapter 5.

Chapter 2: RAD-NETT and its Implementation in a Rectangular Enclosure

In a recent work (Yuen, 2009), a computationally efficient approach was developed for the evaluation of the total absorptivity of a one-dimensional slab of combustion mixture (CO_2 , H_2O , and small particles in which the size of the particles satisfies the Rayleigh small-particle absorption limit) using narrow-band absorption data (Grosshandler, 1993). Specifically, numerical data for the total absorptivity, generated by a direct integration of the spectral data, are correlated by a neural network, RAD-NETT, as a function of the relevant physical parameters such as source temperature, absorption gas temperature, partial pressures, and particle volume fraction. Since the three-dimensional aspect of the radiative heat transfer is important in the overall energy analysis of a building structure, additional neural networks are generated to correlate the relevant surface-surface and surface-volume exchange factors for a specific geometry. These neural network based exchange factors can be used in a zonal analysis to demonstrate the radiative heat transfer characteristics of the considered building structure.

2.1 MATHEMATICAL FORMULATION

A one-zone radiation heat transfer model is developed to determine the radiative heat flux incident on one of its boundaries as a function of temperature, the nature of the combustion mixture and the geometry of the building structure (or furnace). The volume

is assumed to be a rectangular enclosure with dimensions X, Y, and Z as shown in Figure 2.1.

Even in a one-zone model in which the temperature and combustion conditions are assumed to be uniform in the furnace interior, radiative heat transfer is three-dimensional and the various exchange factors must be evaluated for the particular geometry. Specifically, the exchange factor between two surfaces is given by:

$$S_i S_j = \int_{A_i} \int_{A_j} \frac{\left[1 - \alpha(T_w, T_g, P_g L, F_{CO_2}, f_v L)\right] \cos \theta_i \cos \theta_j}{\pi L^2} dA_i dA_j \quad (2.1)$$

In Eqn. (2.1), L is the line-of-sight distance between the two integration area elements dA_i and dA_j . θ_i and θ_j are the angles between the line-of-sight and the unit normal vector of the two differential area elements. T_w is the temperature of the emitting wall and T_g the temperature of the absorbing gas. f_v is the particle volume fraction. P_g is the total partial pressure of the absorbing gas given by:

$$P_g = P_{CO_2} + P_{H_2O} \quad (2.2)$$

with P_{CO_2} and P_{H_2O} being the partial pressure of CO_2 and H_2O , respectively, and

$$F_{CO_2} = \frac{P_{CO_2}}{P_g} \quad (2.3)$$

The total absorptivity, $\alpha(T_w, T_g, F_{CO_2}, P_g L, f_v L)$, is evaluated along the line of sight between the two area elements. Utilizing the formulation of RAD-NETT, the total absorptivity is composed into two components as follow (Yuen, 2009):

$$\alpha(T_w, T_g, P_g L, F_{CO_2}, f_v L) = \Delta\alpha(T_w, T_g, P_g L, F_{CO_2}, f_v L) + \alpha_s(T_w, f_v L) \quad (2.4)$$

$\alpha_s(T_w, f_v L)$ is the absorptivity due to particle absorption only and is given by:

$$\alpha_s(T_w, f_v L) = 1 - \frac{15}{\pi^4} \psi^{(3)} \left(1 + \frac{cLT_w}{C_2} \right) \quad (2.5)$$

with

$$c = 36\pi f_v \frac{n\kappa}{(n^2 - \kappa^2 + 2)^2 + 4n^2\kappa^2} \quad (2.6)$$

C_2 is the second radiation constant and $\psi^{(3)}(z)$ is the pentagamma function. The added absorptivity, $\Delta\alpha(T_w, T_g, P_g L, F_{CO_2}, f_v L)$, is correlated by a neural network over the following range of mixture properties:

$$\begin{aligned} 0 &\leq P_g \leq 100kPa \\ 0 &\leq F_{CO_2} \leq 1.0 \\ 0 &\leq f_v \leq 1.0e-7 \\ 300K &\leq T_w, T_g \leq 1400K \end{aligned} \quad (2.7)$$

with the total pressure of the building structure (or furnace) maintained at 100kPa (1atm).

While the exchange factor can be easily evaluated for a given geometry and mixture properties with the RAD-NETT correlation and a numerical integration, it is still computationally intensive in an actual engineering calculation in which the mixture properties and the surface temperature can be changing continuously. To facilitate a more efficient computational approach, the exchange factor is written as:

$$S_i S_j = A_i F_{ij} \left[1 - \Delta\alpha(T_w, T_g, P_g L_{m,ij}, F_{CO_2}, f_v L_{m,ij}) - \alpha_{s,ij}(T_w, f_v L_{s,ij}) \right] \quad (2.8)$$

where F_{ij} is the view factor between the two surfaces, and $L_{m,ij}$ and $L_{s,ij}$ are two “mean beam length” introduced to characterize the absorption by the particle, $\alpha_{s,ij}(T_w, f_v L_{s,ij})$ and the gas mixture, $\Delta\alpha(T_w, T_g, P_g L_{m,ij}, F_{CO_2}, f_v L_{m,ij})$, respectively. The concept of mean beam length was introduced originally to separate the effect of geometry from mixture properties on the evaluation of exchange factor (Hottel and Sarofim, 1967). While this separation works for some selective geometry and also in the limit of small optical thickness, the mean beam length is generally a function of both mixture properties and geometry (Yuen, 2008). Nevertheless, the influence of geometry on the mean beam length is expected to be less and it is more efficient to develop correlations for mean beam lengths than for the exchange factors.

The development of neural networks for the different mean beam lengths is carried out for a specific geometry of $(X, Y, Z) = (4\text{m}, 5\text{m}, 3\text{m})$. These dimensions are selected because they correspond to those of a full scale fire resistance testing furnace which experimental data for the furnace heat transfer are available. This will facilitate the utilization of FRTF-RAD for the interpretation of the data which will be conducted in Chapter 4. These dimensions are also relatively typical for a room in a residential building. These numerical networks are thus useful to for implementation in BERHT, which will be presented in Chapter 3. It should be noted that the development of neural

network presented in this chapter can be readily extended to an enclosure with different dimensions.

For parallel surfaces, the three relevant mean beam lengths are observed to be independent of the mixture properties as follow:

$$\begin{aligned} L_{s,12} &= L_{m,12} = 1.165Z \\ L_{s,34} &= L_{m,34} = 1.1X \\ L_{s,56} &= L_{m,56} = 1.06Y \end{aligned} \quad (2.9)$$

For two surfaces which are perpendicular, both mean beam lengths depend strongly on the particle and mixture properties and they are tabulated over the range of properties as given by Eqn. (2.7). The numerical data are then correlated by neural networks.

The particle mean beam lengths are correlated by a two-layer neural network as follow:

$$\tilde{R}_{L_{s,ij}} = \sum_{m=1}^3 a_m^1 W_m^2 + b^2 \quad (2.10)$$

with

$$a_m^1 = \tanh \left[W_m^1 \tilde{\tau}_{s,ij} + b_m^1 \right], \quad m=1, 3 \quad (2.11)$$

where

$$\tilde{R}_{L_{s,ij}} = \frac{L_{s,ij}}{L_{c,ij}} \quad (2.12)$$

and $\tau_{s,ij}$ is the particle optical thickness between the two surfaces given by:

$$\tau_{s,ij} = \frac{cL_{c,ij}T}{C_2} \quad (2.13)$$

with $L_{c,ij}$, the characteristic length, is defined to be the center-to-center distance between the two surfaces. The symbol \tilde{x} stands for the normalized value of the variable which takes on the value of 0 and 1 corresponding to the minimum and maximum value of the variable, respectively. Numerical values of minimum and maximum value of the optical thickness and the mean beam lengths, together with the network elements are presented in Table 2.1.

For the mixture mean beam length, $L_{m,ij}$, numerical data show that for small mixture optical thickness ($P_g L_{c,ij}$), the mean beam length is only a function of the mixture optical thickness and independent of other mixture properties as shown in Figure 2.2. For $P_g L_{c,ij} > 5$, the mean beam length depends strongly on the mixture properties and neural networks are correlated by neural networks. In general, a three-layer network with dimensions similar to those used for RAD-NETT are needed for the correlation. A detailed description of the network and the associated numerical data are presented in Appendix A.

With the tabulated mean beam lengths, a zonal analysis is carried out to determine the radiative heat flux incident on the surfaces. Since the exchange factors depend both on the source temperature (T_w) and the medium (T_g), separate analyses are needed to determine the incident heat flux due to the emission from the different walls and that

due to the gas mixture. Specifically, a zonal analysis is carried out for one hot (emitting) wall (A_i), with emissivity ε_i , maintained at temperature $T_{w,i}$ while the remaining walls are assumed to be non-emitting ($T_{w,j} = 0, j \neq i$) with emissivity of ε_j . The mixture is assumed to be absorbing and non-emitting maintained at temperature T_g . Assuming that all surfaces are diffuse, the relevant equations generated from the zonal analysis (Yuen, 1990) are:

$$\frac{(\sigma T_{w,i}^4 - q_{o,i}) A_i \varepsilon_i}{(1 - \varepsilon_i)} = A_i q_{o,i} - \sum_{k \neq i} S_i S_k (T_{w,i}, T_g) q_{o,k} \quad (2.14)$$

$$\frac{(-q_{o,j}) A_j \varepsilon_j}{(1 - \varepsilon_j)} = A_j q_{o,j} - \sum_{k \neq j} S_j S_k (T_{w,i}, T_g) q_{o,k} \quad (2.15)$$

Note that in Eqns. (2.14) and (2.15), all the exchange factors are evaluated at a source temperature of $T_{w,i}$ and a medium temperature of T_g . Thus, the heat transfer to the different walls is given by:

$$Q_j (T_{w,i}, T_g) = \sum_{k \neq j} S_j S_k (T_{w,i}, T_g) q_{o,k} - A_j q_{o,j} \quad j = 1, 6 \quad (2.16)$$

and the heat transfer into the absorbing and non-emitting medium is:

$$Q_g (T_{w,i}, T_g) = \sum_{i=1}^6 \left[A_i - \sum_{j \neq i} S_i S_j (T_{w,i}, T_g) \right] q_{o,i} \quad (2.17)$$

To account for the mixture emission, another analysis is carried out for an absorbing and emitting mixture with reflecting but non-emitting walls. The relevant equations are:

$$\frac{(-q_{og,i}) A_i \varepsilon_i}{(1 - \varepsilon_i)} = A_i q_{og,i} - \sum_{j \neq i} S_i S_j (T_g, T_g) q_{og,j} - \sum_{j \neq i} \left[A_i F_{ij} - S_i S_j (T_g, T_g) \right] \sigma T_g^4 \quad (2.18)$$

for all the absorbing, non-emitting wall ($i = 1, 6$). The heat transfer to the wall is now given by:

$$Q_i = \sum_{k \neq i} S_i S_k (T_g, T_g) q_{og,k} - A_i q_{og,i} + \left[A_i - \sum_{j \neq i} S_i S_j (T_g, T_g) \right] \sigma T_g^4 \quad (2.19)$$

and the heat transfer to the medium is:

$$Q_g = \sum_{i=1}^6 \left[A_i - \sum_{j \neq i} S_i S_j (T_g, T_g) \right] [q_{og,i} - \sigma T_g^4] \quad (2.20)$$

With repeated application of Eqn. (2.14) to (2.17) to the different emitting walls and together with Eqn. (2.18) to (2.20) for the emitting medium, the radiative heat transfer to the different walls and the medium for an enclosure with different boundary conditions and properties can be readily determined.

2.2 Radiative Properties of a CO₂/H₂O/small particles Mixture

One of the important parameters which are of interest to the heat transfer community is the emissivity and absorptivity of the combustion medium. In reference (Harmathy, 1981), for example, it was suggested that for a fire resistance testing furnace and based on “measurements made with a narrow-angle radiometer viewing the gas through a porthole against a water-cooled surface installed across the furnace”, the effective absorption coefficient is estimated to be in the range of 0.18 to 0.22. For a characteristic length of 3m, these data suggest an absorptivity in the range of 0.42 to 0.48. The current model provides an opportunity to assess this important property based on fundamental physics.

For a given set of mixture properties and temperatures, the emissivity of the mixture, radiating to the test specimen (area A_I) can be obtained from the solution to the analysis of an emitting medium and reflecting and non-emitting walls (Eqn. (2.18) as:

$$\varepsilon_g = \frac{Q_1}{A_1 \sigma T_g^4} = \frac{1}{A_1} \left[1 - \sum_{j=2}^6 S_1 S_j (T_g, T_g) \right] + \frac{1}{A_1 \sigma T_g^4} \sum_{j=2}^6 \left[A_1 F_{1j} - S_1 S_j (T_g, T_g) \right] q_{og,j} \quad (2.21)$$

Note that the second term corresponds to the added emission to the test specimen due to the reflection of the surrounding walls. In general, the concept of gas absorptivity depends on the direction and orientation of the emitting surface. For a single emitting surface, A_i , with temperature $T_{w,i}$, the solutions of Eqns. (2.14) to (2.15) can be used to give:

$$\alpha_{g,i} (T_{w,i}, T_g) = \frac{1}{A_1 F_{1i} \sigma T_{w,i}^4} \sum_{j=2}^6 \left[A_1 F_{1j} - S_1 S_j (T_{w,i}, T_g) \right] q_{o,j} \quad (2.22)$$

The hemispherical absorptivity, $\alpha_g (T_w, T_g)$, which is generated by assuming all the surrounding wall are emitting at the same temperature T_w , is given by:

$$\alpha_g (T_w, T_g) = \frac{1}{A_1} \sum_{j=2}^6 A_1 F_{1j} \alpha_{g,j} (T_w, T_g) \quad (2.23)$$

For a typical gaseous concentration found in combustion products ($P_{CO_2} = 5$ kPa, $P_{H_2O} = 5$ kPa), the emissivity of the mixture as a function of gas temperature and particle volume fraction with black surrounding wall is shown in Figure 2.3. Both the mixture temperature and particle volume fraction have strong effects on the mixture emissivity. It is interesting to observe that while the emissivity is generally a decreasing function

with gas temperature for a pure gas mixture ($f_v = 0$), it becomes an increasing function with temperature for a gas-particle mixture ($f_v > 5.e-8$).

The effect of wall reflectivity on the effective mixture emissivity is shown in Figures 2.4a and 2.4b. For simplicity, all surrounding walls are assumed to be at the same emissivity, ε_w , in the calculation for these data. As expected, the “apparent” emissivity increases as the wall reflection increases.

It should be noted that as shown by data in Figures 2.3, 2.4a and 2.4b, the mixture emissivity is much less than unity even in the case of high particle concentration and high wall reflectivity. The assumption of a “black” combustion product mixture is therefore an idealization which is not supported by fundamental physics.

For a pure gas mixture, the hemispherical absorptivity as a function of wall temperature and mixture temperature is shown in Figure 2.5a. At different wall temperature, the hemispherical absorptivity decreases with increasing gas temperature, which is opposite to the trend for emissivity for a pure gas. The hemispherical absorptivity for a gas-particle mixture is shown in Figure 2.5b. The hemispherical absorptivity for a gas-particle mixture increases with wall temperature, particularly in the region of low mixture temperature. Therefore, the assumption of a gray medium with constant and equal emissivity and hemispherical absorptivity for the combustion products is not supported by the fundamental physics.

Chapter 3: BERHT – A Thermal Building Energy Program with Radiative Heat Transfer

3.1 Introduction

BERHT is a thermal building simulation program. The program structure and modeling algorithms are developed based on an existing whole-building energy simulation software, EnergyPlus (2011). With the implementation of the newly formulated neural network correlation, RAD-NETT, BERHT is capable of performing energy simulation with the presence of an absorbing/emitting non-gray medium. Thus, BERHT can be used to study the effect of thermal processes, to simulate energy flows, and to evaluate the heating and cooling energy consumption for a one-zone, multi-layer building structure with the presence of participating media. Although BERHT does not have sophisticated models for HVAC (heating, ventilation, and air conditioning) components, it does have a simple algorithm to compute the required energy input for the heating and cooling. Models for HVAC components as well as models for radiant systems, infiltration, and internal gains for heat and moisture content can be added in the future.

In BERHT, the core of the simulation modeling is primarily based on the principle of heat balance. In a design day, for example, heat balance equation is formulated for each exterior surface, interior surface, and the zone air. The set of equations at each level, namely exterior surfaces, interior surfaces, and the zone air, are solved. Thus, the

unknown temperatures at each level can be determined progressively. Once the temperatures are obtained, they can be used to study the convective and radiation heat flow between the interior surfaces and the enclosed air.

In this chapter, the mathematical formulation for the heat balance equations, the interior longwave radiative heat exchange algorithms, as well as the mass balance equations used in BERHT are presented. The remaining part of the chapter is divided into two sections. The first section presents the benchmark of BERHT against EnergyPlus and the second section presents the numerical studies of the effect of radiative heat transfer in the participating medium on the energy analysis of the enclosure.

3.2 Mathematical Formulation

3.2.1 Energy balance

To formulate the heat balance equations, a building is considered as an enclosure bounded by a number of discrete surfaces, such as walls, floors, ceilings, and windows. These surfaces and the zone air are assumed to have uniform temperatures. At each boundary, heat flux entering the boundary must equal to the heat flux leaving from the boundary. Thus, on any interior surfaces of an enclosure, the heat flow into the surfaces due to the conductive heat flux is balanced by convection from the zone air, heat gain from transmitted solar radiation and other internal sources such as lights and people, and the net radiative flux exchange with the zone air and other surfaces. Similarly, for the exterior surfaces, the absorbed solar radiation, net longwave radiation flux from the

surroundings, and the convective flux from the outdoor air are balanced by the conductive flux entering the surface. In addition, a heat balance on the zone air volume is required to describe any energy imbalance due to the net heat added from the longwave radiation exchange from interior surfaces and the zone air, infiltration, interior heat sources, and convection from interior surfaces.

3.2.1a Opaque Wall Surfaces

The heat balance equation on the exterior surface of an opaque can be written as (Eplus, 2011):

$$q''_{o,s} + q''_{o,c} + q''_{o,lr} - q''_{ko} = 0 \quad (3.1)$$

where $q''_{o,s}$ is the absorbed direct and diffuse solar radiation heat flux, $q''_{o,c}$ is the convective flux exchange with the outdoor air, $q''_{o,lr}$ is the longwave radiation flux exchange with the surroundings, and q''_{ko} is the conductive heat flux into the wall.

The heat balance equation on the interior wall can be formulated as:

$$q''_{ki} + q''_{i,c} + q''_{lwx} + q''_{sol} + q''_{sources} = 0 \quad (3.2)$$

where q''_{ki} is the conduction flux through the wall, $q''_{i,c}$ is the convective heat flux to zone air, q''_{lwx} is the net longwave radiative flux exchange between enclosure surfaces and the zone air, q''_{sol} is the transmitted solar radiation flux absorbed on surface, and $q''_{sources}$ is the sum of the heat gains from lights, equipments, and people in the zone.

The heat balance on the zone air is:

$$\rho_{air} c_p \forall_z \frac{dT_z}{dt} = \sum_{i=1}^{N_{sl}} Q_{i,loads} + \sum_{k=1}^{N_{surf}} h_{ki,c} A_k (T_{ki} - T_z) + \dot{m}_{inf} c_p (T_{air} - T_z) + Q_{sys} + Q_g \quad (3.3)$$

where

$$\rho_{air} c_p \forall_z \frac{dT_z}{dt} = \text{energy stored in zone air}$$

$$\sum_{i=1}^{N_{sl}} Q_{i,loads} = \text{sum of convective internal loads}$$

$$\sum_{k=1}^{N_{surf}} h_{ki,c} A_k (T_{ki} - T_z) = \text{convective heat transfer from zone surfaces}$$

$$\dot{m}_{inf} c_p (T_{air} - T_z) = \text{heat transfer due to infiltration of outdoor air}$$

$$Q_{sys} = \text{air system output}$$

$$Q_g = \text{net longwave radiative heat transfer from zone surfaces}$$

with

$$\rho_{air} = \text{zone air density \{kg/m}^3\}$$

$$c_p = \text{zone air specific heat \{J/kg-K\}}$$

$$\forall_z = \text{zone air volume \{m}^3\}$$

N_{surf} denotes the total number of surfaces in the zone and N_{sl} denotes the number of the different convective loads.

Even though thermal radiation processes in participating media have been well understood for many years, the effect of radiative heat transfer in absorbing/emitting

media in building simulation is often ignored due to the evaluation complexity and the assumption of low absorption coefficients of the participating components (H_2O , CO_2 , and particulates) in air (Eplus, 2011).

In EnergyPlus, Hottel's Grey Interchange Method (Hottel and Sarofim, 1967) is implemented to account for the radiative heat transfer in an enclosure with grey diffuse surfaces. The method begins with the view factor evaluation. Based on the surface area ratio, the surface-to-surface view factors are first approximated. To satisfy the requirements of reciprocity and completeness, the approximated view factors are modified in two procedures through a number of iterations. The modification takes the average of the product of the multiplication between the area and view factors ($A_i F_{ij}$) with its transpose to ensure the reciprocity. Then, each of the $A_i F_{ij}$ within a row is divided by the sum of all its $A_i F_{ij}$ to ensure the completeness. Using the radiosity approach with the modified view factors and the surface emissivity, the grey interchange factor (ScriptF matrix) can be formulated. With the known temperatures, the ScriptF matrix can be used to determine the net radiant flux on a particular surface. Even though Hottel's method does account for the radiative heat transfer from all the possible reflection and re-emission interacting between surfaces in an enclosure, it completely neglects the absorbing air and ignores the longwave radiation exchange between the surfaces and the enclosed air.

In BERHT, a net radiative exchange formulation which incorporates the effect of the absorption species (H₂O, CO₂, and particulates) as well as the geometric effect of the enclosure is implemented. In the formulation development, the medium is assumed to be one-zone with uniform temperatures and properties. The assumption is consistent with the general heat balance principle used in BERHT.

An individual subroutine, *GetRad*, is written to facilitate the evaluation of the radiative heat transfer between the interior surfaces and the enclosed air in the building energy simulation. The subroutine requires information for the following six parameters: 1) the interior surface temperatures, T_w , 2) emissivity of each surface, ε_w , 3) enclosed air temperature, T_g , 4) particle volume fraction, f_v , 5) partial pressure of H₂O, P_{H_2O} , and 6) partial pressure of CO₂, P_{CO_2} . Based on the zonal analysis presented in Chapter 2, the evaluation of the net radiative heat transfer for each of the interior surfaces and the net radiative heat transfer to the enclosed air with the presence of absorbing/emitting medium is carried out in two procedures.

First, a zonal analysis is carried out for one hot wall, assuming to be emitting, absorbing and reflecting, with emissivity ε_i maintained at temperature $T_{w,i}$ with the remaining walls being absorbing, reflecting, but non-emitting at $T_{w,j} = 0$ with emissivity of ε_i . Also, the medium is assumed to be absorbing and non-emitting at temperature T_g . Following the

development presented in Chapter 2, the heat transfer to a surface A_j and the heat transfer to the medium are given by Eqn. (2.16) and (2.17) respectively as:

$$Q_{w,j,i}^{wall}(T_{w,i}, T_g) = \sum_{k \neq j} S_j S_k (T_{w,i}, T_g) q_{o,k} - A_j q_{o,j} \quad j=1,6 \quad (3.4)$$

$$Q_{g,j}^{wall}(T_{w,i}, T_g) = \sum_{i=1}^6 \left[A_i - \sum_{j \neq i} S_i S_j (T_{w,i}, T_g) \right] q_{o,i} \quad (3.5)$$

where $S_i S_j$ is the exchange factor between two surfaces and q_o is the radiosity. The radiosities can be determined through the evaluation of the Eqn. (2.14) and (2.15) in a set of linear equations. Note that the exchange factor is evaluating at the emitting temperature, $T_{w,i}$, and the medium temperature, T_g . The evaluation of the exchange factor using neural network has already been presented in Chapter 2.

Repeating the application of Eqn. (3.4) and (3.5), the net radiative heat transfer to the interior surfaces due to all emitting surfaces is:

$$Q_{w,i}^{wall} = \sum_{j=1}^6 Q_{w,i,j}^{wall}(T_{w,j}, T_g) \quad (3.6)$$

and the heat transfer to the medium due to all emitting surfaces is:

$$Q_{g,tot}^{wall} = \sum_{k=1}^6 Q_{g,k}^{wall}(T_{w,k}, T_g) \quad (3.7)$$

Secondly, to account for the medium emission, another analysis is carried out for the absorbing and emitting medium with reflecting but non-emitting walls. Based on the formulation obtained from Eqn. (2.19), the heat transfer to the wall is given by:

$$Q_w^{gas} = \sum_{k \neq i} S_i S_k (T_g, T_g) q_{og,k} - A_i q_{og,i} + \left[A_i - \sum_{j \neq i} S_i S_j (T_g, T_g) \right] \sigma T_g^4 \quad (3.8)$$

and the heat transfer to the medium is:

$$Q_g^{gas} = \sum_{i=1}^6 \left[A_i - \sum_{j \neq i} S_i S_j (T_g, T_g) \right] [q_{og,i} - \sigma T_g^4] \quad (3.9)$$

The radiosities can be determined through the evaluation of Eqn. (2.18) in a set of linear equations. The total net heat transfer to the difference walls due to the surfaces and gas emission is:

$$Q_i = Q_{w,i}^{wall} + Q_{w,i}^{gas} = q_{lwx,i}'' A_i \quad (3.10)$$

and the total heat transfer to the medium is:

$$Q_g = Q_g^{wall} + Q_g^{gas} \quad (3.11)$$

where q_{lwx}'' is the representation of the longwave radiative flux exchange between the interior surfaces and the enclosed air used in BERHT.

The modeling description for the other terms appeared in Eqn. (3.1), (3.2), and (3.3) is presented in Appendix B. A detailed explanation for each of the models can be obtained in Eplus (2011). In this study, we would like to consider only a simple system to understand the effect of interior longwave radiative exchange. For this reason, infiltration, HVAC system, and the internal heat gains from lights, equipments, and people, are not included in the current version of BERHT.

With the utilization of the conduction transfer function (CTF) solution (Seem, 1991) and convection model from TARP algorithm (Walton, 1983) shown in appendices, Eqn. (3.1) for the exterior surface can be rewritten as:

$$\begin{aligned}
& q''_{o,s} + \left[h_{o,c} (T_{air}^t - T_o^t) \right] + \\
& \left[h_{r,air} (T_{air}^t - T_o^t) + h_{r,sky} (T_{sky}^t - T_o^t) + h_{r,gnd} (T_{gnd}^t - T_o^t) \right] - \\
& \left[-Y_{CFT,0} T_i^t - \sum_{j=1}^{N_z} Y_{CFT,j} T_i^{t-j} + X_{CFT,0} T_o^t + \sum_{j=1}^{N_z} X_{CFT,j} T_o^{t-j} + \sum_{j=1}^{N_q} \Phi_{CFT,j} q''_{ko}^{t-j} \right] = 0
\end{aligned} \tag{3.12}$$

where T_o is the exterior surface temperature, T_i is the interior surface temperature, T_{air} is the air temperature, T_{sky} is the sky temperature, T_{gnd} is the ground temperature, $h_{o,c}$ is outside convection heat transfer coefficient, and $h_{r,air}$, $h_{r,sky}$, and $h_{r,gnd}$ is linearized radiative heat transfer coefficient to air, sky, and ground, respectively. The superscript denotes the time-step.

Based on the CTF solution and the natural convection formulation, the interior surface heat balance equation in Eqn. (3.2) can be expressed as:

$$\begin{aligned}
& \left[-Z_{CTF,0} T_i^t - \sum_{j=1}^{N_z} Z_{CTF,j} T_i^{t-j} + Y_{CTF,0} T_o^t + \sum_{j=1}^{N_z} Y_{CTF,j} T_o^{t-j} + \sum_{j=1}^{N_q} \Phi_{CTF,j} q''_{ki}^{t-j} \right] + \\
& \left[h_{i,c} (T_z^t - T_i^t) \right] + q''_{lwx} + q''_{sol} + q''_{sources} = 0
\end{aligned} \tag{3.13}$$

where T_z is the zone air temperature, $h_{i,c}$ is the inside convection heat transfer coefficient, and X_{CTF} , Y_{CTF} , Z_{CTF} , and Φ_{CTF} are the conduction transfer function coefficients. N_z and N_q denote the number of required CTF terms.

To approximate the derivative term with respect to time using, the third order backward finite difference method is utilized (Taylor, 1990),

$$\frac{dT_z}{dt} \approx (\Delta t)^{-1} \left(\frac{11}{6} T_z^t - 3T_z^{t-\Delta t} + \frac{3}{2} T_z^{t-2\Delta t} - \frac{1}{3} T_z^{t-3\Delta t} \right) + O(\Delta t^3) \quad (3.14)$$

and Eqn. (3.3) can be rewritten as:

$$\frac{\rho_{air} c_p \nabla_z}{\Delta t} \left(\frac{11}{6} T_z^t - 3T_z^{t-1} + \frac{3}{2} T_z^{t-2} - \frac{1}{3} T_z^{t-3} \right) = \sum_{k=1}^{N_{surf}} h_{ki,c} A_k (T_{ki}^t - T_z^t) + Q_g \quad (3.15)$$

Note that the present form of Eqn. (3.12), (3.13), and (3.15) is implicit and highly coupled. In (3.12), for example, the determination of the convection and the linearized radiation coefficients requires the unknown exterior surface temperatures that are currently being evaluating. As seen, the heat transfer at the exterior surface is linked to the heat transfer at the interior surface through the CTFs while the heat transfer at the interior surface is substantially tied to the convective heat transfer to the zone air as well as the radiative heat transfer from all other interior surfaces. Since solving all the heat balance equations simultaneously requires significant increases in the computation required and solution time, a simplification is made. In the evaluation of Eqn. (3.12), (3.13), and (3.15), BERHT simply uses the “most updated” temperatures, following the approach by Energy-Plus (2011). With this treatment, the heat transfer coefficients can be determined based on the most current temperatures and each of the heat balance equations can be evaluated individually. The resulting errors from the use of this simplification are shown to be small (Sowell and Walton, 1980). In general, BERHT first determines the exterior surface temperatures with the “lagged” information. Then,

BERHT calculates the interior surface temperatures, allowing sequence evaluation of the room air. The same computation procedure will be carried out for the entire design day.

By applying the simplification, Eqn. (3.12), (3.13), and (3.15) are modified and rearranged to give the following expression:

$$T_o^t = \frac{\left[q_{o,s}^{m_t} + (h_{o,c}^{t-1} + h_{r,air}^{t-1})T_{air}^t + h_{r,sky}^{t-1}T_{sky}^t + h_{r,gnd}^{t-1}T_{gnd}^t + Y_{CFT,o}T_o^{t-1} - \left(-\sum_{j=1}^{N_z} Y_{CFT,j}T_i^{t-j} + \sum_{j=1}^{N_z} X_{CFT,j}T_o^{t-j} + \sum_{j=1}^{N_q} \Phi_{CFT,j}q_{ko}^{m_{t-j}} \right) \right]}{X_{CFT,o} + h_{o,c}^{t-1} + h_{r,air}^{t-1} + h_{r,sky}^{t-1} + h_{r,gnd}^{t-1}} \quad (3.16)$$

for exterior surface temperature { °C },

$$T_i^t = \frac{\left[\sum_{j=1}^{N_z} Y_{CTF,j}T_o^{t-j} - \sum_{j=1}^{N_z} Z_{CTF,j}T_i^{t-j} + \sum_{j=1}^{N_q} \Phi_{CTF,j}q_{ki}^{m_{t-j}} + \left(h_{i,c}^{t-1}T_z^{t-1} + Y_{CTF,o}T_o^{t-1} + q_{lwx}^{m_{t-1}} + q_{sol}^{m_t} \right) \right]}{Z_{CTF,o} + h_{i,c}^{t-1}} \quad (3.17)$$

for interior surface temperature { °C }, and

$$T_z^t = \frac{\sum_{k=1}^{N_{surf}} h_{ki,c}^{t-1} A_k T_{ki}^{t-1} + \left(\frac{\rho_{air} c_p \nabla_z}{\Delta t} \right) \left(3T_z^{t-1} + \frac{3}{2}T_z^{t-2} - \frac{1}{3}T_z^{t-3} \right) + Q_g}{\left(\frac{11}{6} \right) \frac{\rho_{air} c_p \nabla_z}{\Delta t} + \sum_{k=1}^{N_{surf}} h_{ki,c}^{t-1} A_k} \quad (3.18)$$

for zone air temperature { °C }.

3.2.1b Glazing Surface

The heat balance for the single-layer-windows used in BERHT is similar to the WINDOW 4 model (Finlayson et al, 1993). Based on this model, the window is divided

into 2 surfaces; 1 denotes the outside face and 2 denotes the inside face. The window is assumed to be opaque to the longwave radiant heat flux and, similarly to the wall surfaces, the window is exposed to convective and radiative flux exchange to the surrounding on both faces. Depending on its optical properties, the window will absorb, transmit, and/or reflect a portion of the shortwave solar radiation. Given with these details, the heat balance for the single-layer-glazing is:

$$E_1 \varepsilon_1 - \varepsilon_1 \sigma \theta_{g,1}^4 + k(\theta_{g,2} - \theta_{g,1}) + h_{1,c}(T_{air} - \theta_{g,1}) + S_{g,1} = 0 \quad (3.19)$$

for exterior face and

$$E_2 \varepsilon_2 - \varepsilon_2 \sigma \theta_{g,2}^4 + k(\theta_{g,1} - \theta_{g,2}) + h_{2,c}(T_z - \theta_{g,2}) + S_{g,2} = 0 \quad (3.20)$$

for interior face

where

$\theta_{g,i}$ = temperature of face i

T_{air} and T_z = outdoor and zone air temperatures

ε_i = emissivity of face i

k = conductivity of glass

$h_{1,c}$ and $h_{2,c}$ = outside and inside convection coefficient

E_1 and E_2 = exterior and interior longwave radiation incident on window

$S_{g,i}$ = radiation (shortwave, and longwave from other internal sources) absorbed by face

i.

Note that the steady state assumption is incorporated in the formulation of the window heat balance due to the fact that the window is generally thin and with relatively high conductivity. Eqn. (3.19) and (3.20) can be arranged in matrix form:

$$\begin{bmatrix} h_{1,r} + k + h_{1,c} & -k \\ -k & h_{2,r} + k + h_{2,c} \end{bmatrix} \begin{bmatrix} \theta_{g,1} \\ \theta_{g,2} \end{bmatrix} = \begin{bmatrix} S_{g,1} + \varepsilon_1 E_1 + h_1 T_{air} \\ S_{g,2} + \varepsilon_2 E_2 + h_2 T_z \end{bmatrix} \quad (3.21)$$

and the window temperature of both faces can be obtained in the following expression:

$$\begin{bmatrix} \theta_{g,1} \\ \theta_{g,2} \end{bmatrix} = \begin{bmatrix} h_{1,r} + k + h_{1,c} & -k \\ -k & h_{2,r} + k + h_{2,c} \end{bmatrix}^{-1} \begin{bmatrix} S_{g,1} + \varepsilon_1 E_1 + h_1 T_{air} \\ S_{g,2} + \varepsilon_2 E_2 + h_2 T_z \end{bmatrix} \quad (3.22)$$

where h_r is the linearized radiation coefficient.

For the evaluation of the longwave radiation heat transfer into the interior surface, the zonal approach for the opaque surface will be utilized. When the glazing surface is only a part of the full bounding wall, the exchange factor will be approximated as a fraction of the exchange factor with the full bounding wall based on the area fraction.

3.2.2 Mass Balance

The determination of the interior longwave radiation exchange between the surfaces and the enclosed participating medium requires the humidity ratio and the carbon dioxide concentration of the enclosed air, as well as the possibility of a finite particulate/particle concentration. A set of mass balance equations of these participating species are included in BERHT.

The transient air mass balance equation for the change in the zone humidity ratio, W_z , may be expressed by the following (Eplus, 2011):

$$\rho_{air} \nabla_z \frac{dW_z}{dt} = \sum_{i=1}^{N_{sl}} kg_{mass_{schedload}} + \dot{m}_{inf} (W_{air} - W_z) + \dot{m}_{sys} (W_{sup} - W_z) \quad (3.23)$$

where

$$\sum_{i=1}^{N_{sl}} kg_{mass_{schedload}} = \text{sum of scheduled internal latent load \{kg/s\}}$$

$$\dot{m}_{inf} (W_{air} - W_z) = \text{moisture transfer due to infiltration of outdoor air \{kg/s\}}$$

$$W_{air} = \text{humidity ratio in outdoor air \{--\}}$$

$$\dot{m}_{sys} (W_{sup} - W_z) = \text{moisture transfer due to system supply \{kg/s\}}$$

$$W_{sys} = \text{humidity ratio in system supply \{--\}}$$

$$\rho_{air} \nabla_z \frac{dW_z}{dt} = \text{moisture storage term in zone air \{kg/s\}}$$

with

$$\rho_{air} = \text{zone air density \{kg/m}^3\}$$

$$\nabla_z = \text{zone air volume \{m}^3\}.$$

The change in the zone carbon dioxide concentration, C_z , is equal to the sum of schedule internal carbon dioxide loads, infiltration, and output from the system and the transient mass balance equation may be expressed as follows:

$$\rho_{air} \nabla_z \frac{dC_z}{dt} = \sum_{i=1}^{N_{sl}} kg_{mass_{schedload}} \times 1.6^6 + \dot{m}_{inf} (C_{air} - C_z) + \dot{m}_{sys} (C_{sup} - C_z) \quad (3.24)$$

where

$$\rho_{air} \nabla_z \frac{dC_z}{dt} = \text{carbon dioxide storage in zone air \{ppm-kg/s\}}$$

$$\dot{m}_{inf} (C_{air} - C_z) = \text{carbon dioxide transfer due to infiltration of outdoor air \{ppm-kg/s\}}$$

$$C_{air} = \text{carbon dioxide concentration in outdoor air \{ppm\}}$$

$$\dot{m}_{sys} (C_{sup} - C_z) = \text{carbon dioxide transfer due to system supply \{ppm-kg/s\}}$$

$$C_{sys} = \text{carbon dioxide concentration in system supply \{ppm\}}$$

$$\sum_{i=1}^{N_{sl}} kg_{mass_{schedload}} = \text{sum of scheduled internal carbon dioxide loads \{ppm-kg/s\} with the}$$

coefficient of 10^6 is used to convert the units of carbon dioxide to ppm.

The transient air mass balance equation for the change in the zone particle concentration,

C_{soot} , may be expressed as the following:

$$\rho_{air} \nabla_z \frac{1}{\rho_C} \frac{dC_{soot}}{dt} = \left[\sum_{i=1}^{N_{sl}} kg_{mass_{schedload}} \times \frac{1}{\rho_C} + \frac{\dot{m}_{inf}}{\rho_{inf}} \frac{1}{\rho_C} (\rho_{inf} C_{soot,inf} - \rho_{air} C_{soot}) + \frac{\dot{m}_{sys}}{\rho_{sys}} \frac{1}{\rho_C} (\rho_{sys} C_{soot,sys} - \rho_{air} C_{soot}) \right] \quad (3.25)$$

where

$$\rho_{air} \nabla_z \frac{1}{\rho_C} \frac{dC_{soot}}{dt} = \text{particle storage term in zone air}$$

ρ_C = density of carbon at room temperature {kg/m³}

$$\frac{\dot{m}_{inf}}{\rho_{inf}} \frac{1}{\rho_C} (\rho_{inf} C_{s,inf} - \rho_{air} C_{soot}) = \text{particle transfer due to infiltration of outdoor air \{kg/s\}}$$

$C_{soot,air}$ = particle concentration in outdoor air {kg/m³}

$$\frac{\dot{m}_{sys}}{\rho_{sys}} \frac{1}{\rho_C} (\rho_{sys} C_{soot,sys} - \rho_{air} C_{soot}) = \text{particle transfer due to system supply \{kg/s\}}$$

$C_{soot,sys}$ = particle concentration in system supply {kg/m³}

$$\sum_{i=1}^{N_{sl}} kg_{mass_{schedload}} \times \frac{1}{\rho_C} = \text{sum of schedule internal particle loads \{kg/m}^3\}$$

with

particle volume fraction to be $f_v = C_{soot} / \rho_C$

In the above equation, the particle concentration is assumed to be sufficiently small so that it has no effect on the overall mixture density and the particles will always be at thermal equilibrium with the mixture.

In the same manner as described above for the zone air temperature, the third order backward finite difference method is used to approximate the derivative term with respect to time in Eqn. (3.23), (3.24), and (3.25).

The zone air update at current time-step can be expressed as:

$$W_z^t = \frac{\sum_{i=1}^{N_{sl}} kg_{mass_schedload} + \dot{m}_{inf} W_{air} + \dot{m}_{sys} W_{sup} + \left(\frac{\rho_{air} \nabla_z}{\Delta t} \right) \left(3W_z^{t-1} + \frac{3}{2}W_z^{t-2} - \frac{1}{3}W_z^{t-3} \right)}{\left(\frac{11}{6} \right) \frac{\rho_{air} \nabla_z}{\Delta t} + \dot{m}_{inf} + \dot{m}_{sys}} \quad (3.26)$$

for the humidity ratio,

$$C_z^t = \frac{\sum_{i=1}^{N_{sl}} kg_{mass_schedload} \times 1.6^6 + \dot{m}_{inf} C_{air} + \dot{m}_{sys} C_{sup} + \left(\frac{\rho_{air} \nabla_z}{\Delta t} \right) \left(3C_z^{t-1} + \frac{3}{2}C_z^{t-2} - \frac{1}{3}C_z^{t-3} \right)}{\left(\frac{11}{6} \right) \frac{\rho_{air} \nabla_z}{\Delta t} + \dot{m}_{inf} + \dot{m}_{sys}} \quad (3.27)$$

for the carbon dioxide concentration, and

$$C_{soot}^t = \frac{\sum_{i=1}^{N_{sl}} kg_{mass_schedload} + \dot{m}_{inf} C_{soot,air} + \dot{m}_{sys} C_{soot,sup} + \left(\frac{\rho_{air} \nabla_z}{\Delta t} \right) \left(3C_{soot}^{t-1} + \frac{3}{2}C_{soot}^{t-2} - \frac{1}{3}C_{soot}^{t-3} \right)}{\left(\frac{11}{6} \right) \frac{\rho_{air} \nabla_z}{\Delta t} + \dot{m}_{inf} + \dot{m}_{sys}} \quad (3.28)$$

for the particle concentration.

3.3 Results

3.3.1 Benchmarking Cases

Two case studies are set up to examine the consistency and accuracy of BERHT in regards to the energy balances at various boundaries in a non-participating media. The simulated results are compared to that obtained from EnergyPlus. The expected outputs are the total absorbed solar radiation of exterior surfaces, the transmitted solar radiation through glazing, and the temperatures of exterior surfaces, interior surfaces, and zone air.

The test building (Figure 3.1) is a rectangular 60m^3 single zone (5m wide x 4m long x 3m tall) with no interior partitions. The building as specified in the EnergyPlus document is intended to be a closed system, responding to the heat transfer driven by design day conditions specified in the document. As shown in Figure 3.1, the building is constructed with 6 surfaces: four 90° tilted (vertical) surfaces, a roof, and a floor. The vertical surfaces are oriented in four different directions: surface facing north (0° azimuth), surface facing east (90° azimuth), surface facing south (180° azimuth), and surface facing west (270° azimuth). The building is simulated as if it were located in the United States in Chicago, Illinois on a typical summer day (July, 21st). All surfaces, except the floor, are exposed to varying temperatures, wind conditions, and solar radiation. These imposed conditions are determined based on the information of the weather file obtained from EnergyPlus' weather library. The global wind speed approaching the building is maintained at 5m/s in the south direction. The temperature variation of the design day is 10.9°C with a maximum temperature of 32.8°C . The ground temperature is maintained at 20.3°C throughout the design day. As a closed system, infiltration, ventilation, and HVAC systems are not included in the test calculation. The detail of the location and weather of the site are shown in Table 3.1 and Table 3.2, respectively.

In the first case, we consider the test building with 4 walls, a roof, and a floor as shown in Figure 3.1. Dimension of each surface, construction of each envelope, and thermal

properties of each material are shown in Table 3.3, Table 3.4, and Table 3.5, respectively.

A full design day simulation, from 00:00 to 23:59, is conducted on both BERHT and EnergyPlus. All simulation results are obtained every 5 minutes. Simulated results obtained from BERHT are compared to those obtained from EnergyPlus. The total absorbed solar radiation of each surface is shown in Figure 3.2. The total solar radiation absorbed by the exterior surface consists of 1) the beam solar radiation, 2) sky diffused solar radiation, and 3) ground reflected solar radiation. Each of the exterior surface temperature profiles is plotted in Figure 3.3. Note that the floor surface temperature is expected to remain constant at 22.3°C due to its constant temperature boundary condition. The temperature profiles of interior surfaces are shown in Figure 3.4 and the temperature profile of the room air is shown in Figure 3.5. As seen, excellent agreement is obtained between the two programs.

In the second case, we consider a 4m x 3m single-layer window on the east surface. The window properties are listed in Table 3.6 and the remaining configuration of the test building is identical to that of case one.

Similar to case 1, simulated results are obtained from BERHT and EnergyPlus every 5 minutes. The total absorbed solar radiation of each surface is presented in Figure 3.6. As shown, the total solar radiation absorbed by north, south, west, and the floor surface is

identical to that observed in case 1, whereas the total solar radiation absorbed by the east surface is noticeably lower. This result is expected for a window surface because a large portion of solar radiation is either reflected or transmitted into the interior. The transmitted solar radiation for window on east surface is shown in Figure 3.7. Temperature profiles for the exterior surfaces and the interior surfaces are presented in Figure 3.8 and Figure 3.9, respectively. Note that due to the added solar gains to the interior, the temperature for each of the interior surfaces increases approximately by 4°C to 5°C. In Figure 3.10, approximately 5°C to 6°C increase in the room air temperature is observed. Interestingly, regardless of the dramatic change in temperature inside the enclosure, the exterior temperatures remain nearly identical to that obtained in case 1. Similar to case 1, excellent agreement is achieved between the two programs.

3.3.2 Effect of Participating Medium

In this section, results of numerical studies are presented to illustrate the effect of a participating medium. An isotropic homogenous absorbing/emitting medium is considered. Three participating species in the gas volume are included, namely H₂O, CO₂, and small particles. In a design day, the concentration for each of the species can be determined using Eqn. (3.26), (3.27), and (3.28). Since our goal is to examine the potential maximum radiative heat transfer effect in the participating medium, studies were conducted with a fixed partial pressure of 5 kPa for H₂O and CO₂ and a fixed volume fraction (0 or 10⁻⁶) for the small particles. Note that, the gas-mixture partial

pressure and the particle volume fraction are higher than the expected values in an indoor environment.

Two series of studies were conducted. In the first series of studies, simulations were made using the identical testing building and configurations specified in benchmark case 1 with the presence of participating medium. The objective in these studies is to examine the importance of interior longwave radiative heat transfer and its effect to the overall heat transfer. The second series of studies were carried out using the identical specifications that are specified in benchmark case 2 with the presence of participating medium. The objective of these studies is to investigate the driving mechanisms of the greenhouse effects in building enclosure with presence of participating medium.

For case 1, numerical data for the heat transfer to the medium in three cases (transparent, absorbing/emitting gas only, and absorbing/emitting gas/particle mixture) are presented in Figure 3.11a, Figure 3.11b, and Figure 3.11c, respectively. The total convective heat transfer, the total net radiative heat transfer, and the overall heat transfer (the total convective heat transfer together with the total net radiative heat transfer) between the surfaces and the room air are shown to illustrate the effect of radiative heat transfer. Numerical data are generated separately for two different wall emissivities (emissivity = 0.9 and emissivity = 0.1 which are assumed to be identical for all interior surfaces). Results show that radiative heat transfer is at the same order of magnitude as convective heat transfer. As shown in Figures 3.11b and 3.11c, the added effect of radiative heat transfer appears to be compensated by a corresponding increase or decrease in the

convective heat transfer, leading to relatively minor effect on the overall heat transfer. The added effect of radiation, which is compensated by the corresponding changes in the interior convection between the surface and the zone air, appears to have only minor effect on the zone air temperature as shown in Figure 3.12.

Physically, the lack of impact of radiative heat transfer on the overall heat transfer and the zone air temperature can be understood by noting that the zone air temperature and the overall heat transfer are not only controlled by the internal heat transfer mechanisms, they are also being influenced by the external heat transfer and boundary conditions such as solar irradiation, wind speed, and surrounding temperatures. To illustrate this interaction systematically, a series of simulations were conducted for a transparent medium with the convective heat transfer modified by a multiplicative factor. Results for the total heat transfer to the zone air and the corresponding zone air temperature for different factors (0.1 and 0.01 in reduction for convection, and 2 and 10 for increase in convection) are shown in Figures 3.13a and Figures 3.13b. It is interesting to note that over a wide range of the convective heat transfer effect (factor of 1/10, 2, and 10), the heat transfer to the zone air and the corresponding air temperature do not vary significantly. The effect of reduced convection is significant only when the multiplicative factor is 1/100.

To compare the effect of radiation and convection, the convective heat transfer coefficient to the surfaces for the normal convection case and the “double” convection

case are shown in Figures 3.14. The equivalent convective effect for radiation can be estimated by an equivalent heat transfer coefficient ($4\sigma T_w^3$). For $T_w \sim 300\text{K}$, the equivalent heat transfer coefficient is approximately $6\text{W/m}^2\text{-K}$. The radiative heat transfer effect is therefore in the order of increasing the convective heat transfer by a factor between 2 to 5. As shown in Figure 3.13a and Figure 3.13b, this enhancement is insufficient to cause significant changes on the total heat transfer and the resulting zone air temperature.

Since the actual convective heat transfer in the enclosure can be lower due to the one-zone approximation and/or the mechanisms to reduce convection, it is useful to conduct simulation to illustrate the effect of radiation heat transfer under the condition of reduced convection. Results for cases with 1/10 and 1/100 of the normal convection are shown in Figures 3.15 to Figures 3.18. It is interesting to note that the effect of radiative heat transfer is also sensitive to the surface emissivity. For the case with lower emissivity of 0.1, the zone air temperature is higher and the total heat transfer between the surfaces and the air is higher.

To further illustrate how radiation heat transfer will impact the individual distribution between radiative and convective heat transfer, a simulation was conducted with the emissivity of the floor parameterized to be at 0.9 and the remaining surfaces kept at 0.1 in case 1. The total heat transfer to the zone air and the corresponding zone air

temperature for the three radiative absorption cases are shown in Figure 3.19. While the effect of radiation is noticeable, the heat transfer and the zone temperature are not significantly different from those of the uniform emissivity case shown in Figure 3.11c and Figures 3.12. However, in terms of the individual convective and radiative heat transfer, there are significant differences as shown in Figure 3.20. Compared to the uniform emissivity cases, the case with different emissivities shows a significant increase in both convective and radiative heat transfer. It is observed that the two heat transfer modes have opposing effect. The zone air is heated by convection, due to the hot surrounding surfaces with emissivity of 0.1 while it is also being cooled by radiation, due to the cold floor with an emissivity of 0.9. The combined effect leads to a total heat transfer profile which, again, is largely controlled by the outside heating and cooling.

To understand the physical mechanisms leading to the large increase in the two heat transfer modes, the temperature at the different surfaces for the transparent case and the case with an absorbing/emitting gas/particle mixture are shown in Figure 3.21. It is apparent that the temperature distribution is largely driven by the surface to surface radiative exchange and convective heat transfer. The effect of an absorbing/emitting medium is shown to be relatively minor. The change of the floor emissivity to 0.9 and keeping the surrounding wall emissivity at 0.1 has the effect of maintaining a relatively large temperature difference between the zone air and the surrounding wall (the characteristic of emissivity of 0.1) while decreasing the temperature difference between the zone air and the floor (the characteristic of the case with emissivity of 0.9). The

effect on these temperature differences on convective and radiative heat transfer is shown in Figure 3.22. For the convective heat transfer, the reduction of temperature difference between the zone air and the floor (relative to the case of emissivity of 0.1 for all surfaces) and the relative large temperature difference between the other surfaces and the zone air leads to a net increase of the total convective heat transfer. Due to the nonlinear effect of radiation, however, the temperature difference between the zone air and the floor dominates and as the radiative heat transfer between the remaining surfaces is reduced (compare to the case of emissivity equal to 0.9 for all surfaces), the net radiative heat transfer from the zone air also increases.

In summary, the results for the different scenarios of case 1 show that the effect of radiative heat transfer on the overall heat transfer within the enclosure is not large because the total heat balance is dominated by external factors (incoming shortwave and longwave radiation, surrounding temperatures, and convective heat transfer). However, radiation has important effects on the distribution of heat transfer between convection and radiation, depending on the surface emissivity of the enclosure walls and the optical properties of the absorbing/emitting medium.

When the shortwave solar radiation strikes the glazing on a building surface, the solar radiation is being partly absorbed, reflected, and transmitted. The transmitted solar radiation is absorbed by the interior surfaces. Since the glazing generally has low transmissivity for longwave radiation, the emission from the walls and the medium will

be trapped in the enclosure, leading to a heating effect. This process is commonly known as the “greenhouse” effect.

In this second series of study, the effect of an absorbing/emitting medium on the “greenhouse” effect will be demonstrated by numerical simulation using the building configurations specified in Case 2. The results obtained for the transparent medium case and the participating medium case are compared to the results obtained for the transparent medium case with no radiation being transmitted into the interior. This special case is denoted as the reference case and its results are denoted as the reference results. The window optical properties are shown in Table 3.7.

The total heat transfer obtained for the reference case is shown in Figure 3.23 and the corresponding results for cases with transmitted shortwave radiation with a transparent medium and an absorbing/emitting gas/particle mixture medium for different wall emissivities are presented in Figure 3.24a, Figure 3.24b, and Figure 3.24c, respectively. As shown, due to the extra heat addition to the interior, the magnitude of the combined modes of heat transfer between the surfaces and the room air is nearly double. In general, the greenhouse effect is stronger for the case with lower emissivity as it leads to higher wall temperature and therefore increases convective and radiative heat transfer to the medium. Similar to the case 1, the presence of a participating medium changes the distribution of the heat transfer between convection and radiation, but not the total heat transfer. This result suggests that in an enclosure, the greenhouse effect can be sustained

by the absorption of the wall, which leads to a higher wall temperature and an increase in the subsequent heat transfer to the medium. Figure 3.25 shows the room air temperature profile of the reference case, transparent medium case, and the participating medium case.

Chapter 4: Analysis of Heat Transfer in a Fire Resistance Testing Furnace

In fire safety, the use of a fire resistance test furnace to evaluate the “destructive potential” of building materials under standardized test conditions (Harmathy, 1981, Sultan, 1986, and ASTM, 1995) is a commonly accepted practice to fulfill the various prescriptive and/or performance based fire resistance requirement. Since the “standard” required is “to expose building elements to heating in accordance with a standard temperature-time relation” (ASTM, 1995), there has been much uncertainty and controversy in relating results of the test to “real world fires”. For example, the heat load imposed on a test specimen depends strongly on the size of furnace, the conditions of the furnace wall, and the nature of the combustion gases. Even when these test conditions are known, an effective heat transfer and radiation model is needed to relate the temperature-time history to the heat load on the test specimen. Modeling thus provides an important link between the test data and the actual “destructive potential” of the test specimen.

The fundamental understanding of the various heat transfer processes in a fire resistance test furnace was first reported more than 20 years ago (Harmathy, 1981, Sultan, 1986). Over the years, while there were some efforts to come up with different engineering approaches to better characterize the measured furnace data for design applications

(Wickstrom, 2008 and Wickstrom, 2011), very few efforts have been reported to provide further quantitative understanding of the fundamental heat transfer, in spite of the significant advances in the understanding of combustion, convective heat transfer, and radiative heat transfer. The primary reason is the difficulty in simulating the realistic effect of radiation heat transfer in the combustion environment of the furnace. To account for the non-gray spectral absorption characteristics of the combustion products and the multi-dimensional effect of the furnace geometry, the computational effort is quite intensive and difficult to implement in a practical engineering calculation.

In this chapter, RAD-NETT and the neural network developed in Chapter 2 are used to develop a simulation of the radiative heat transfer characteristics in a fire resistance test furnace. By comparison with experimental data (Sultan, 2003 and Sultan 2006), the general scalability of data generated by furnaces of different scales is assessed and discussed.

4.1 Analysis and Results

A primary objective of a fire resistance test furnace is to determine the heat load on test specimen for a given combustion condition. In references (Sultan, 2003) and (Sultan 2006), for example, temperature and heat flux data were obtained from a full scale fire resistance test furnace (5m x 4m x 3m) and also from an intermediate scale (1.2m x 1.8m x 0.5m) in an attempt to resolve the difficult issue of scaling in fire resistance testing. Since full scale tests are time consuming and expensive, there are significant

interest in performing small scale tests and utilizing the data for design and safety applications. Based on measured heat fluxes obtained from the two furnaces generated with the same time-temperature heating profile generated by a propane-fired combustion, it was concluded that the heat exposure in the intermediate-scale furnace is only slightly higher (15%) than in the full-scale furnace. The authors concluded that “For fire exposure, testing an assembly in an intermediate-scale furnace will provide a conservative performance compared to a full-scale furnace”.

Even though the amount of quantitative data presented in references (Sultan, 2003) and (Sultan 2006) are limited (only furnace temperature and heat flux at the test specimen are presented), an analysis based on RAD-NETT can be used to provide a quantitative interpretation of the experimental data and to give an assessment of the relevant radiative heat transfer mechanisms in the furnace. In the experiment (Sultan, 2003), the combustion within the furnace is controlled so that the measure furnace average temperature follow the ASTM E119 time-temperature curve (ASTM, 1995) as shown in Figure 4.1. Since it is difficult to determine the exact control mechanism to maintain the furnace temperature (e.g. the amount of fuel consumed by the combustion, the mixture conditions, etc.), it is not possible to do a complete simulation of the furnace performance based on first principle. The present work thus focuses only on the radiative heat transfer. Even though convection is expected to have an important contribution to the overall heat transfer (Harmathy, 1981, Sultan, 1986), the radiation-

only analysis can still be effective in illustrating some qualitative aspects of the heat transfer process.

A computer code, FRTF-RAD (Fire Resistance Testing Furnace with Radiation), is developed to determine the incident radiative heat flux on the test specimen. The code incorporates the zonal analysis presented in Ch. 2 with all the neural network exchange factors. The mixture temperature history and the wall temperature history for all the enclosure boundaries except area A_1 are prescribed by the user as input conditions. Since the objective is to determine the incident heat flux on the test sample, the area A_1 is assumed to be a non-emitting but reflecting surface. Based on solution to Eqns. (2.14) and (2.15), the incident flux due to the emission from a single emitting wall can be generated from the radiosities as:

$$q_{inc,w,i}(T_{w,i}, T_g) = \frac{1}{A_1} \sum_{j=2}^6 S_1 S_j(T_{w,i}, T_g) q_{o,j} \quad (4.1)$$

The total incident flux due to emission from all the surrounding walls is given by:

$$q_{inc,w} = \sum_{j=2}^6 q_{inc,w,j}(T_{w,j}, T_g) \quad (4.2)$$

The incident flux due to the mixture emission can be generated from the solution to Eqns. (2.18) as:

$$q_{inc,g} = \frac{1}{A_1} \sum_{k \neq 1} S_1 S_k(T_g, T_g) q_{og,k} + \left[1 - \frac{1}{A_1} \sum_{j \neq 1} S_1 S_j(T_g, T_g) \right] \sigma T_g^4 \quad (4.3)$$

and the total incident radiative heat flux due to both wall and gas emission is given by:

$$q_{inc} = q_{inc,w} + q_{inc,g} \quad (4.4)$$

Using the ASTM E119 time-temperature curve and assuming a moderate value of partial pressure (5kPa) for H₂O and CO₂, the incident radiative heat flux to the test specimen (A_I) generated by the combustion gas/particle mixture in the full scale furnace at various particle volume fraction, together with the experimental data from three independent repeated tests (Sultan, 2003), are shown in Figure 4.2. It is apparent that emission from the combustion gases/particle mixture is insufficient to generate the observed heat flux, even when the particle volume fraction is increased to physically unrealistic large values. These results suggest strongly that the radiation from the furnace wall contributes significantly to the total heat flux at the test specimen.

Thermodynamically, it can be shown that for an isothermal furnace with the furnace walls maintained at the same temperature as the combustion medium, the heat flux to the test specimen is a maximum and corresponds to that of a blackbody at the furnace temperature. The numerical data for an isothermal furnace, together with the measured heat flux (Sultan, 2003), are presented in Figures 4.3a and 4.3b. The measured heat flux for all three cases follows the blackbody heat flux closely, suggesting that the furnace is indeed operating essentially at the isothermal condition. The slight increase in the measured temperature in tests 2 and 3 can probably be attributed to convective heat transfer and the possibility that some portion of the walls might be at a temperature higher than the combustion temperature. Indeed, given that the heat exposure for both

the full scale and intermediate scale furnace correspond closely to the blackbody heat flux (with the intermediate scale slightly higher) (Sultan, 2003 and Sultan, 2006), the test results show that both furnaces are operating isothermally. The general conclusion that “an intermediate-scale furnace will provide a conservative performance compared to a full-scale furnace” reached in reference (Sultan, 2003 and Sultan 2006) is therefore applicable only for an isothermal furnace. Additional studies are required to understand the scalability of test results generated from non-isothermal furnaces.

Finally, results in Figure 4.2 demonstrate that for a pure gas combustion product, it will be difficult to reach the flashover limit of 20kW/m^2 (Peacock, 1999) in a compartment fire, even at a high temperature ($>1000\text{K}$). This confirms the suggestion made in a previous work (Yuen and Chow, 2004) that the presence of particle in the combustion products is an important factor for the initiation of flashover in a compartment fire. In addition, results in Figures 4.3a and 4.3b also suggest that even without the presence of particle, the re-radiation from the surrounding wall can contribute significantly to the heat load, leading to the possibility of a flashover. These conclusions have potential impact in the development of strategy to suppress flashover in a compartment fire which will be considered in a future work.

Chapter 5: Conclusions

This study demonstrates the use of neural network for the evaluation of thermal radiative heat transfer and fluxes in a rectangular-shaped building structure with the presence of an isotropic homogenous absorbing/emitting medium. Neural network is shown to be an efficient tool to allow the realistic absorption/emission effect of a medium to be incorporated accurately and efficiently in a heat transfer calculation in a three-dimensional building structure. The formulation of neural network based exchange factors, accounting for the effect of the absorption species (CO_2 , H_2O , and/or small particles) and the geometric effect of the enclosure, is presented. The utilization of the neural network exchange factors in a one-zone net radiative exchange model is illustrated and the model is implemented into two computer codes to analyze the effect and characteristics of thermal radiative heat transfer in two building environments.

A computer code, BERHT, is developed to simulate and understand the thermal radiative heat transfer effect in a low temperature building structure environment. The simulation considers thermal radiation between surfaces and zone air in the enclosure, convective heat transfer between interior surfaces and zone air, transient heat conduction in the wall surfaces, and external convection and radiation on the walls, simultaneously.

Studies have been carried out in two building configurations for two different interior emissivity surfaces and four different convection conditions. Based on the interior boundary conditions considered in the numerical study, results show that the presence of participating medium has a significant effect in the distribution of the total heat transfer between convection and radiation. However, the overall energy balance is influenced strongly by external conditions such as surrounding temperatures, exterior convective heat transfer, and shortwave and longwave radiation. The presence of a participating medium has only a minimal impact on the overall heat transfer and the temperature of the zone air.

The effect of radiative heat transfer due to the influence of added solar heat gain from the solar radiation transmitted through a large window is studied. Transmitted solar radiation is shown to affect the heating characteristics of the interior and lead to a significant increase in temperature on both the interior surfaces and zone air. Increase in both radiative and convective heat transfer is observed. Numerical studies confirm that the absorption of shortwave radiation by the surface and the subsequent heat transfer from the surface to the zone air is the primary mechanism for the “greenhouse” effect. Also, the effect of participating medium on the overall heat transfer is shown to be minimal due to the strong influence of the outside heat transfer parameters.

To study the effect of thermal radiative heat transfer characteristics in a fire resistance test furnace (a high temperature application), a computer code FRTF-RAD is developed.

The code focuses only on the thermal radiative heat transfer and does analysis based on a one-zone net radiation model similar to that of used in BERHT.

In this study, a numerical analysis is carried out to understand the effect of wall reflectivity, wall temperature, mixture temperature, and particle volume fraction to the mixture emissivity and hemispherical absorptivity in a fire resistance test furnace. For pure gas mixture, the mixture emissivity is shown to be an increasing function with decreasing mixture temperature and/or increasing wall reflectivity, whereas the hemispherical absorptivity is increasing function with increasing mixture temperature and/or decreasing wall temperature. For gas-particle mixture, results show completely different characteristics for the mixture emissivity and hemispherical absorptivity. The mixture emissivity is found to be an increasing function with increasing mixture temperature and/or increasing wall reflectivity. The hemispherical absorptivity is an increasing function with increasing mixture temperature and/or increasing wall temperature. Based on this analysis, two findings are concluded, 1) the assumption of a black combustion product mixture and 2) the assumption of a gray medium with constant and equal emissivity and hemispherical absorptivity are not supported by fundamental physics.

A study is also conducted to simulate the radiative heat fluxes in a fire resistance test furnace to provide a quantitative interpretation of the experiment data and an assessment of its relevant radiative heat transfer mechanisms. Prediction of heat flux from the

different “black” walls and the heat flux from the combustion mixture to the test specimen is obtained. In comparison to the experimental data, it is shown that radiation from the furnace walls and the emission from the combustion gas-particle mixture are both important to generate the observed total heat flux at the test specimen. It is also seen that the heat exposure for the full-scale and intermediate-scale furnace corresponds closely to the blackbody heat flux. These justify that both test furnaces are operating at isothermal condition. It is found that the heat exposure for the intermediate-scale furnace is slightly higher when compared to the full-scale furnace; it confirms that tests carried out in an isothermal intermediate-scale fire resistance test furnace will provide a conservative performance compared to an isothermal full-scale furnace. In terms of fire safety, results show that particle is an important absorbing species for the radiative heat transfer assessment in a compartment fire and the re-radiation from surrounding walls can be a significant contribution to the heat load that leads to the possibility of a flashover.

The building structure taken in this study is considered a simplified geometry in comparison to real-life situations. However, it is hoped that observation made from this study can be used for the current practice of building energy design and fire safety assessment to account for the realistic effect of thermal radiative heat transfer where energy saving, thermal comfort, and control of fire and smoke spread are of prime importance.

Reference

ASHRAE. ASHRAE Handbook – Fundamentals, Atlanta: American Society of Heating, Refrigerating, and Air-Conditioning Engineers, Inc, 2005

ASHRAE. ASHRAE Handbook – Fundamentals, Atlanta: American Society of Heating, Refrigerating, and Air-Conditioning Engineers, Inc, 2009

ASTM. ASTM E119-88, Standard Methods of Fire Tests of Building Construction and Materials, ASTM, Philadelphia, PA, 1995.

Chapman, A. J., *Heat Transfer*, 4th ed., New York: Macmillan Publishing Company, 1984.

Cooper, L. Y. and Forney G. P., The Consolidated Compartment Fire Model (CCFM) computer code application CCFM.VENTS. Part 1., physical basis, NISTIR 4342, National Institute of Standards and Technology, Gaithersburg, MD, 1990.

DeST, in *DeST-h Technology Document*, DeST, 2004.

Eplus, in *EnergyPlus Documentation-Engineering Reference*, The Board of Trustees of the University of Illinois and the Regents of the University of California through the Ernest Orlando Lawrence Berkeley National Laboratory, ver. 7, pp 65-79, 2011.

Finlayson, E.U., D.K. Arasteh, C. Huizenga, M.D. Rubin and M.S. Reilly. *WINDOW 4.0: documentation of calculation procedures*, Lawrence Berkeley National Laboratory report no. LBL-33943, 1993.

Furler, R. A., Angular dependence of optical properties of homogeneous glasses, *ASHRAE Transactions*, 97(2), 1129-1133, 1991.

Grosshandler, W. L., RADCAL, A Narrow-Band Model for Radiation Calculations in a Combustion Environment, NIST-TN-1402, National Institute of Standard and Technology, April 1993.

Hagen, M. T., Demuth, H. B., and Beale, M., *Neural Network Design*, PWB Publishing Company, Boston, 1995.

Harmathy, T. Z., The Fire Resistance Test and its Relation to Real-World Fires, *Fire and Materials*, vol. 5, no. 3, pp. 112-122, 1981.

Hottel, H. C., and Sarofim, A. F., *Radiative Transfer*, McGraw Hill, New York, 1967.

IES, in *ApacheSim Calculation Methods <Virtual Environment> 6.3*, IES <VE>, 2010.

Ineichen, P., and Perez, R., Derivation of cloud index from geostationary satellites and application to the production of solar irradiance and daylight illuminance data. *Theoretical and Applied Climatology*, 64(1-2), 119-130, 1999.

Jones, W. W., Peacock, R. D., Forney, G. P., and Reneke, P. A., *CFAST, Consolidated Model of Fire Growth and Smoke Transport*, NIST Special Publication 1026, The National Institute of Standard and Technology, USA, Dec, 2005.

LBNL, in *DOE-2 Engineers Manual Version 2.1A*, Lawrence Berkeley National Laboratory's Simulation Research Group, U.S. Department of Energy, pp 46-69, 1982.

Liang, Jing, Li, Baizhan, Wu, Yong, and Yao, Runming, An investigation of the existing situation and trends in building energy efficiency management in China, *Energy and Buildings*, vol. 39, no. 10, pp 1098–1106, 2007.

Lombard, Luis Pérez, José Ortiz, and Christine Pout, A review on buildings energy consumption information, *Energy and Buildings*, vol. 40, no. 3, pp 394–398, 2008.

Oppenheim, A.K., Radiation analysis by the network method, *ASME Trans*, vol. 78, pp. 725-735, 1956.

Peacock, R. D., Reneke, P. A., Bukowski, R. W., and Babrauskas, V., Defining Flashover for Fire Hazard Calculations, *Fire Safety Journal*, vol. 32, pp. 331-345, 1999.

Perez R., Ineichen P., Maxwell E., Seals, R., and Zelenka, A., Dynamic Global-to-Direct Irradiance Conversion Models, *ASHRAE Transactions-Research Series*, 354-369, 1992.

Perez, R., Ineichen, P., Seals, R., Michalsky, J. and Stewart, R., Modeling daylight availability and irradiance components from direct and global irradiance, *Solar Energy* 44, 271-289, 1990.

Portier, R. W., Peacock, R. D., Reneke, P. A., FASTLite: Engineering Tools for Estimating Fire Growth and Smoke Transport, NIST SP 899, National Institute of Standards and Technology, Gaithersburg, MD, 1996.

Rabl, A., *Active solar collectors and their applications*, Oxford University Press, USA, 1985.

Seem, J. E., *Modeling of Heat Transfer in Buildings*, Ph.D, Thesis, University of Wisconsin, Madison, WI, 1987.

Sellers, William D. *Physical climatology*, Chicago: University of Chicago Press, 1965.

Siegel, R., and Howell, J., *Thermal Radiation Heat Transfer*, 4 ed., Taylor and Francis, New York, 2002.

Sowell, E. F., and G. N. Walton, Efficient computation of zone loads, *ASHRAE Transactions*, vol 86, no. 1, pp 49-72, 1980.

Sultan, M. A., Harmathy, T. Z., and Mehaffey, J. R., Heat Transmission in Fire Test Furnaces, *Fire and Materials*, vol. 10, pp. 47-55, 1986.

Sultan, M. A., Incident Heat Flux Measurements in Wall and Floor Furnaces of Different Sizes, *Fire and Materials*, vol. 30, No. 6, pp. 383-396, 2006.

Sultan, M. A., Benichou, N., and Min, B. Y., *Heat Exposure in Fire Resistance Furnaces: Full-Scale vs Intermediate-Scale*, Proceeding of the 2003 Fire and Materials International Conference, San Francisco, pp. 45-53, January, 2003.

TAS, in *Theory Manual*, Thermal Analysis Software. 2010.

Taylor, N., *Energy Efficiency for Everyone: Analysis and Development of an Energy Efficient Project Home*, B.S. thesis, Department of Environmental Engineering, the University of Western Australia, Australia, 2002.

Torcellini, P., Pless, S., Deru, M., Griffith, B., Long, N., and Judkoff, R., *Lessons Learned from Case Studies of Six High-Performance Buildings*, Technical Report, NREL/TP-550-37542, June, 2006.

Trnsys, in *TRNSYS 16 Documentation*, Transient System Simulation program, vol. 5, pp225-235, 2013.

Walton, G. N. *Thermal Analysis Research Program Reference Manual*. NBSSIR 83-2655. National Bureau of Standards, 1983.

Wickstrom, U., *Adiabatic Surface Temperature and the Plate Thermometer for Calculating Heat Transfer and Controlling Fire Resistance Furnaces*, Proceeding of the 9th International Symposium on Fire Safety Science, Sept., 2008.

Wickstrom, U., Robbins, A., and Baker, G., The Use of Adiabatic Surface Temperature to Design Structure for Fire Exposure, *Journal of Structural Fire Engineering*, vol. 2, no.1, pp. 21-28, 2011.

Yuen, W. W., Development of a Network Analogy and Evaluation of Mean Beam Lengths for Multi-Dimensional Absorbing/Isotropically-Scattering Media, *ASME Journal of Heat Transfer*, vol. 112, pp. 408-413, 1990.

Yuen, W. W., and Chow, W. K., The role of Thermal Radiation on the Initiation of Flashover in a Compartment Fire, *International Journal of Heat and Mass Transfer*, vol. 47, pp. 4265-4276, 2004.

Yuen, W. W., Definition and Evaluation of Mean Beam Lengths for Applications in Multi-Dimensional Radiative Heat Transfer, a Mathematically Self-Consistent Approach, *ASME Journal of Heat Transfer*, vol. 130, no.11, pp.114507, Nov. 2008.

Yuen, W. W., RAD-NETT, a Neural Network Based Correlation Developed for a Realistic Simulation of the Non-gray Radiative Heat Transfer Effect in Three-Dimensional Gas-Particle Mixture, *International Journal of Heat and Mass Transfer*, vol. 52, pp. 3159-3168, 2009.

i	j	$\tau_{s,ij,\min}$	$R_{L_{s,ij},\min}$	W^1	b^1	W^2	b^2
		$\tau_{s,ij,\max}$	$R_{L_{s,ij},\max}$				
1,2	3,4	0.05	0.117	3.304	-5.078	-2.154	3.866
		20.0	0.795	1.671	2.107	-1.877	
				-9.814	-11.07	5.024	
1,2	5,6	0.05	0.112	3.235	-5.146	-2.909	3.183
		20.0	0.704	1.659	2.062	-1.825	
				-9.625	-10.91	5.145	
3,4	5,6	0.05	0.102	3.245	-5.140	-2.704	2.957
		20.0	0.685	1.623	1.967	-1.609	
				-8.926	-10.15	4.935	

Table 2.1: Neural network data for the particle mean beam length $L_{s,ij}$ for perpendicular surfaces in the fire resistance test furnace.

Site Information and Location		
Name	Units	Object
Site Name	--	Chicago, IL, USA
Latitude	deg	41.78
Longitude	deg	-87.75
Time Zone	hr	-6
Elevation	m	190

Table 3.1: Site information and location.

Site Weather Conditions		
Name	Units	Object
Maximum Dry-Bulb Temperature	°C	32.8
Daily Dry-Bulb Temperature Range	ΔC	10.9
Humidity at Maximum Dry-Bulb	°C	23.6
Barometric Pressure	Pa	99063.21
Wind Speed	m/s	5
Wind Direction	deg	0
Day of Month	--	21
Month	--	7
Average Ground Temperature	°C	23

Table 3.2: Site weather conditions.

Dimension of Building Enclosure				
	Units	Object1	Object2	Object3
Name		North Surface	East Surface	South Surface
Vertex 1X-coordinate	m	4	4	0
Vertex 1Y-coordinate	m	5	0	0
Vertex 1Z-coordinate	m	3	3	3
Vertex 2X-coordinate	m	4	4	0
Vertex 2Y-coordinate	m	5	0	0
Vertex 2Z-coordinate	m	0	0	0
Vertex 3X-coordinate	m	0	4	4
Vertex 3Y-coordinate	m	5	5	0
Vertex 3Z-coordinate	m	0	0	0
Vertex 4X-coordinate	m	0	4	4
Vertex 4Y-coordinate	m	5	5	0
Vertex 4Z-coordinate	m	3	3	3

Dimension of Building Enclosure (Continued)				
	Units	Object4	Object5	Object6
Name		West Surface	Floor Surface	Roof Surface
Vertex 1X-coordinate	m	0	0	0
Vertex 1Y-coordinate	m	5	0	5
Vertex 1Z-coordinate	m	3	0	3
Vertex 2X-coordinate	m	0	0	0
Vertex 2Y-coordinate	m	5	5	0
Vertex 2Z-coordinate	m	0	0	3
Vertex 3X-coordinate	m	0	4	4
Vertex 3Y-coordinate	m	0	5	0
Vertex 3Z-coordinate	m	0	0	3
Vertex 4X-coordinate	m	0	4	4
Vertex 4Y-coordinate	m	0	0	5
Vertex 4Z-coordinate	m	3	0	3

Table 3.3: Dimension of building enclosure.

Table: 3.4 Construction of building envelopes				
	Units	Object1	Object2	Object3
Name		North Surface	East Surface	South Surface
Layer 1	--	Wood siding -1	Wood siding -1	Wood siding -1
Layer 2	--	Fiberglass Quilt - 1	Fiberglass Quilt - 1	Fiberglass Quilt - 1
Layer 3	--	Plasterboard - 1	Plasterboard - 1	Plasterboard - 1

Table 3.4: Construction of building envelopes (continued)				
	Units	Object4	Object5	Object6
Name		West Surface	Floor Surface	Roof Surface
Layer 1	--	Wood siding -1	HF - C5	Roof deck
Layer 2	--	Fiberglass Quilt - 1	na	Fiberglass Quilt - 2
Layer 3	--	Plasterboard - 1	na	Plasterboard - 2

Table 3.4: Construction of building envelopes.

Table 3.5: Construction material properties				
	Units	Object1	Object2	Object3
Name		Plasterboard 1	Fiberglass Quilt 1	Wood siding 1
Roughness	--	MediumSmooth	Rough	Rough
Thickness	m	0.012	0.066	0.009
Conductivity	W/m-K	0.16	0.04	0.14
Density	kg/m ³	950	840	530
Specific Heat	J/kg-K	840	840	900
Thermal Absorptance	--	0.9	0.9	0.9
Solar Absorptance	--	0.6	0.6	0.6

Construction material properties (continued)					
	Units	Object4	Object5	Object6	Object7
Name		Plasterboard 2	Fiberglass Quilt 2	Roof deck	HF C5
Roughness	--	Rough	Rough	Rough	MediumRough
Thickness	m	0.01	0.1119	0.019	0.1015
Conductivity	W/m-K	0.16	0.04	0.14	1.7296
Density	kg/m ³	950	12	530	2243
Specific Heat	J/kg-K	840	840	900	837
Thermal Absorptance	--	0.9	0.9	0.9	0.9
Solar Absorptance	--	0.6	0.6	0.6	0.65

Table 3.5: Construction material properties.

Window Optical Properties in Case 1		
	Units	Object1
Name		Clear - 6mm
Thickness	m	0.006
Solar Transmittance at Normal Incidence	--	0.2
Front Side Solar Reflectance at Normal Incidence	--	0.6
Back Side Solar Reflectance at Normal Incidence	--	0.6
Visible Transmittance at Normal Incidence	--	0.2
Front Side Visible Reflectance at Normal Incidence	--	0.6
Back Side Visible Reflectance at Normal Incidence	--	0.6
Infrared Transmittance at Normal Incidence	--	0
Front Side Infrared Reflectance at Normal Incidence	--	0.9
Back Side Infrared Reflectance at Normal Incidence	--	0.9
Conductivity	W/m-K	0.9

Table 3.6: Window optical properties in Case 1.

Window Optical Properties in Case 2		
	Units	Object1
Name		Clear - 6mm
Thickness	m	0.006
Solar Transmittance at Normal Incidence	--	0
Front Side Solar Reflectance at Normal Incidence	--	0.8
Back Side Solar Reflectance at Normal Incidence	--	0.8
Visible Transmittance at Normal Incidence	--	0
Front Side Visible Reflectance at Normal Incidence	--	0.8
Back Side Visible Reflectance at Normal Incidence	--	0.8
Infrared Transmittance at Normal Incidence	--	0
Front Side Infrared Reflectance at Normal Incidence	--	0.9
Back Side Infrared Reflectance at Normal Incidence	--	0.9
Conductivity	W/m-K	0.9

Table 3.7: Window optical properties in Case 2.

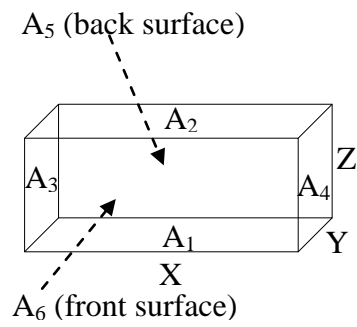


Figure 2.1: The geometry and area identification used in the model for a fire resistance test furnace.

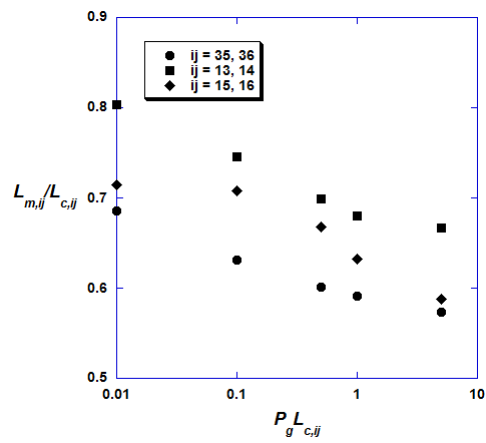


Figure 2.2: The mixture mean beam length for perpendicular areas for the considered fire resistance test furnace for small and moderate mixture optical thicknesses.

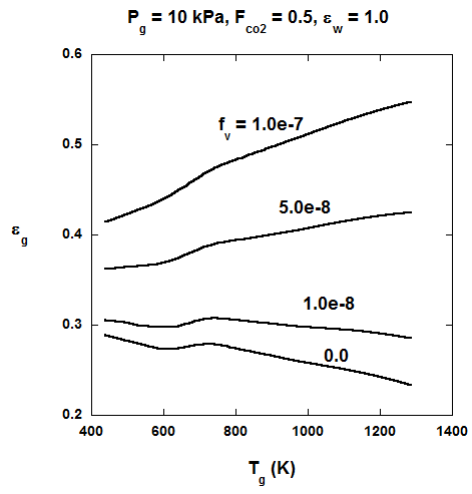


Figure 2.3: The emissivity of the mixture for the considered fire resistance test furnace with black surrounding wall.

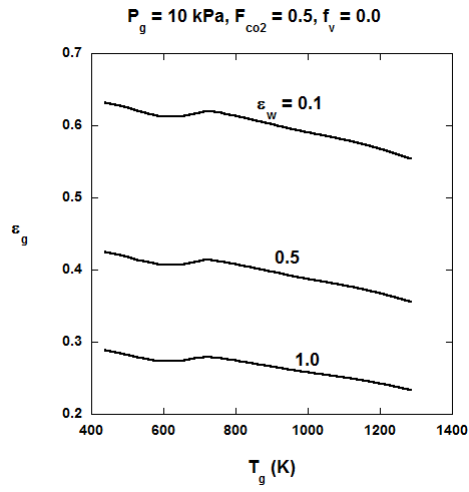


Figure 2.4a: Effective of wall emissivity on the mixture emissivity in the considered fire resistance test furnace for a pure gas mixture.

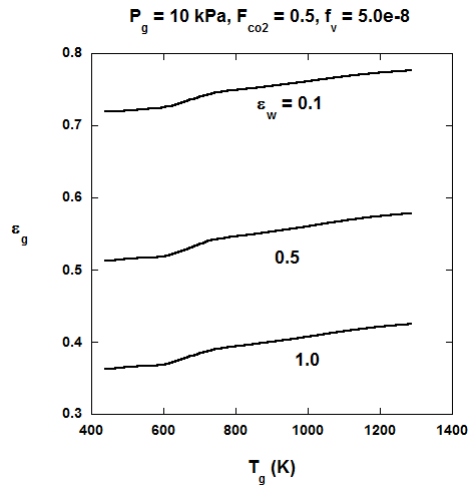


Figure 2.4b: Effective of wall emissivity on the mixture emissivity in the considered fire resistance test furnace for a gas-particle mixture.

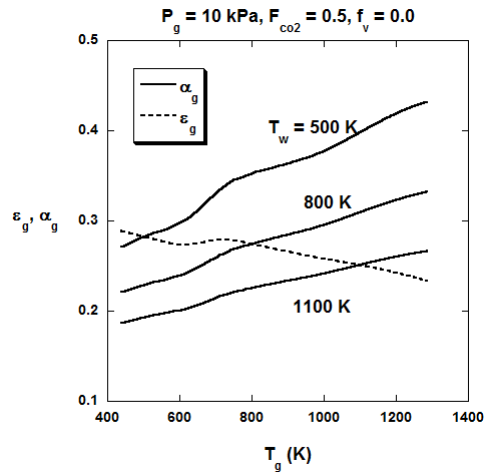


Figure 2.5a: The absorptivity of the mixture for the considered fire resistance test furnace at different wall temperature (the emissivity of the mixture is also shown in the figure for comparison).

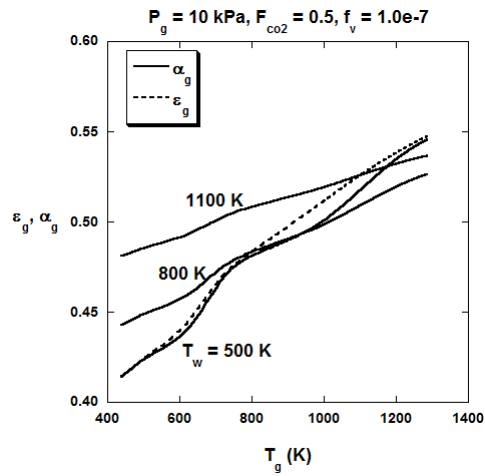


Figure 2.5b: The absorptivity of a gas-particle mixture for the considered fire resistance test furnace at different wall temperature (the emissivity of the mixture is also shown in the figure for comparison).

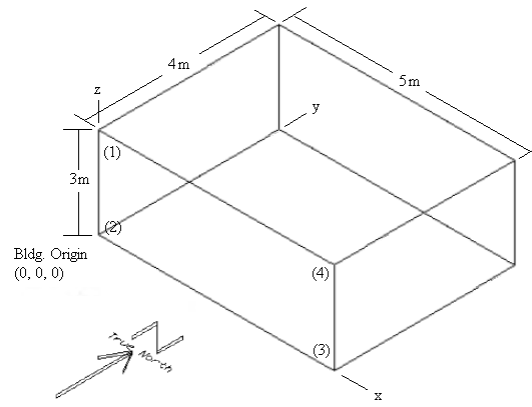


Figure 3.1: Geometry of building enclosure.

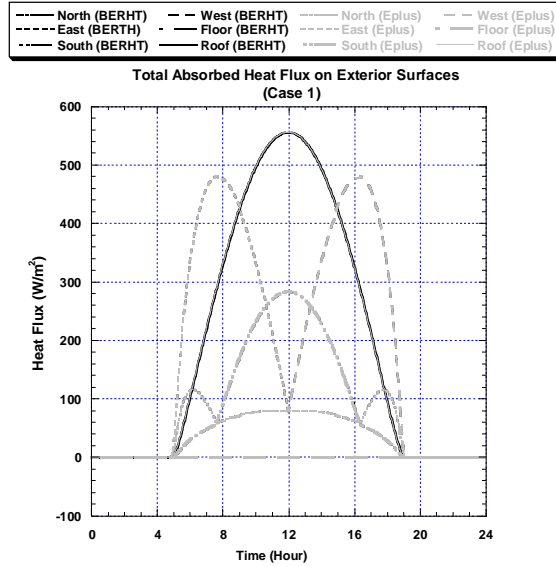


Figure 3.2: Comparison of total absorbed shortwave solar radiation (BERHT and Eplus) for different exterior surfaces in benchmark case 1.

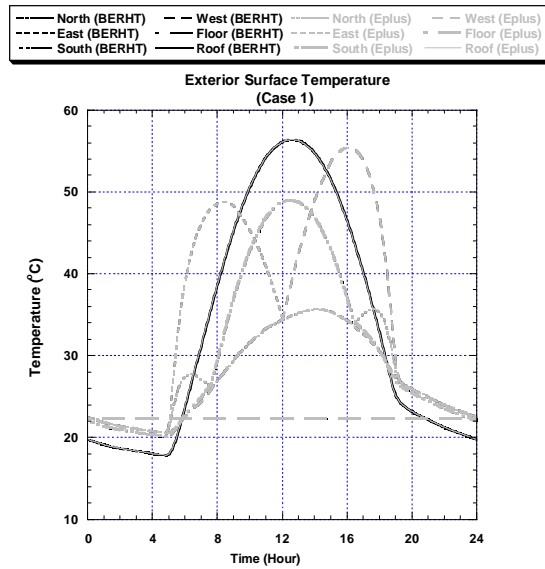


Figure 3.3: Comparison of exterior surface temperatures (BERHT and Eplus) for benchmark case 1.

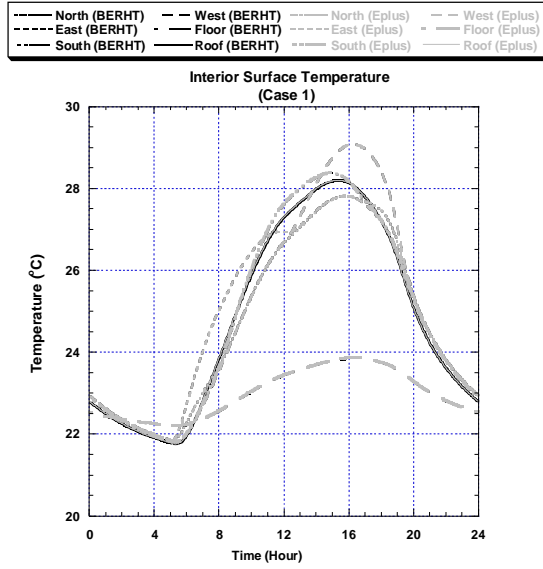


Figure 3.4: Comparison of interior surface temperatures (BERHT and Eplus) for benchmark case 1.

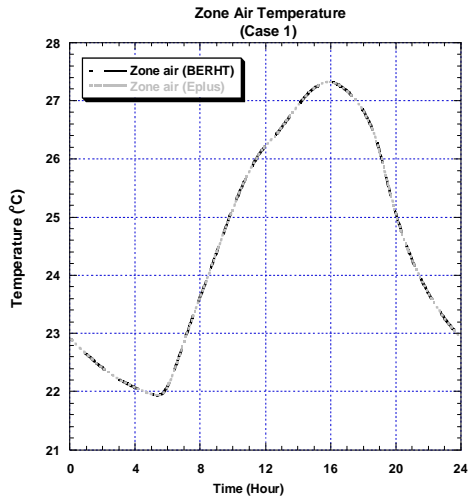


Figure 3.5: Comparison of zone air temperature (BERTHT and Eplus) for benchmark case 1.

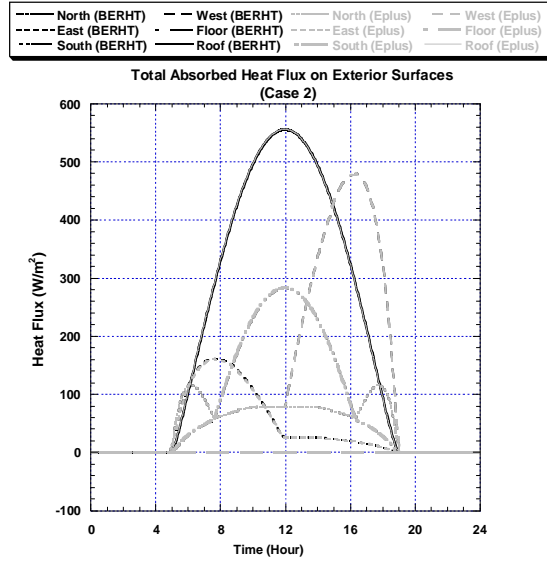


Figure 3.6: Comparison of total absorbed shortwave solar radiation (BERHT and Eplus) for different exterior surfaces in benchmark case 2.

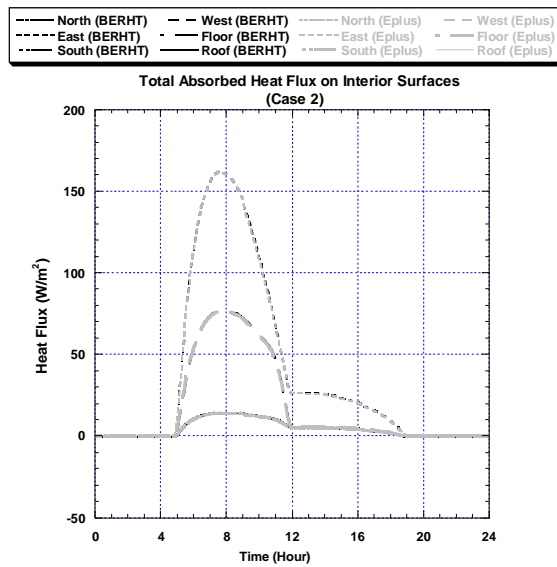


Figure 3.7: Comparison of total absorbed shortwave solar radiation (BERHT and Eplus) for different interior surfaces in benchmark case 2.

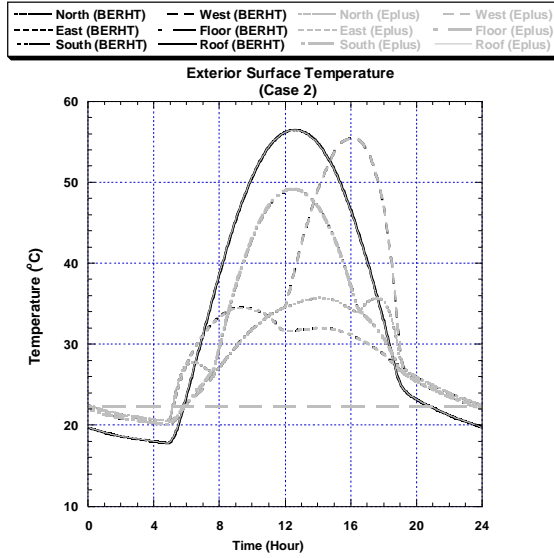


Figure 3.8: Comparison of exterior surface temperatures (BERHT and Eplus) for benchmark case 2.

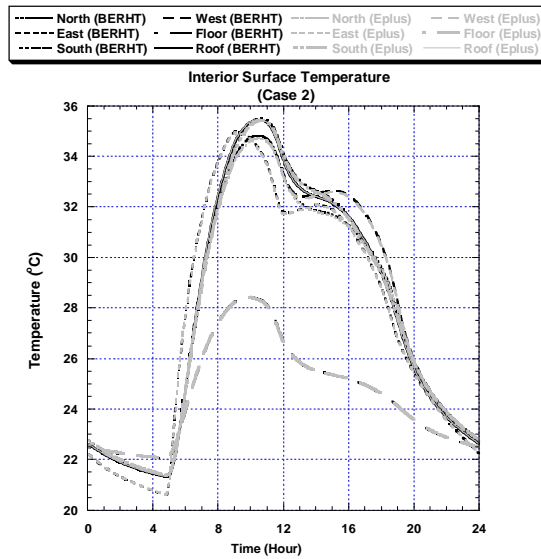


Figure 3.9: Comparison of interior surface temperatures (BERHT and Eplus) for benchmark case 2.

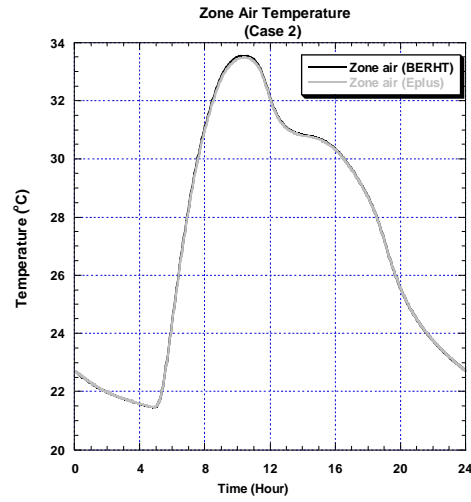


Figure 3.10: Comparison of zone air temperature (BERHT and Eplus) for benchmark case 2.

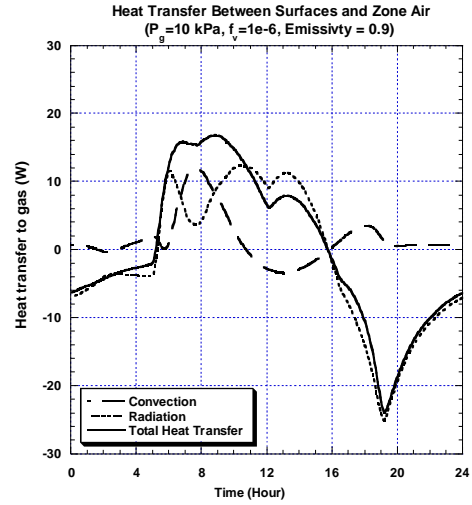
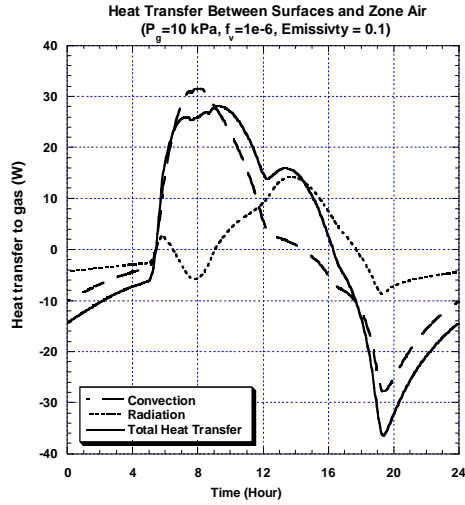


Figure 3.11a: Heat transfer (radiation, convection, and total) between surfaces and room air with an absorbing/emitting gas/particle mixture for case 1 with different emissivity.

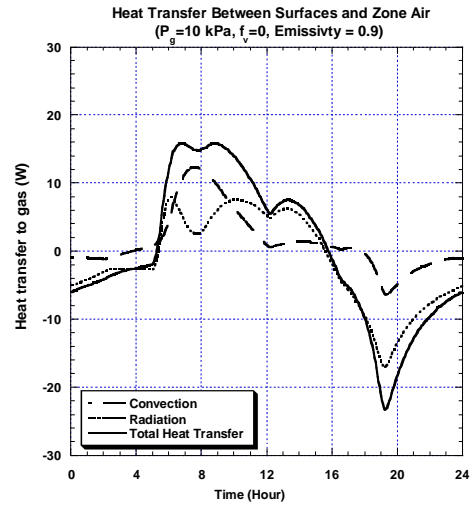
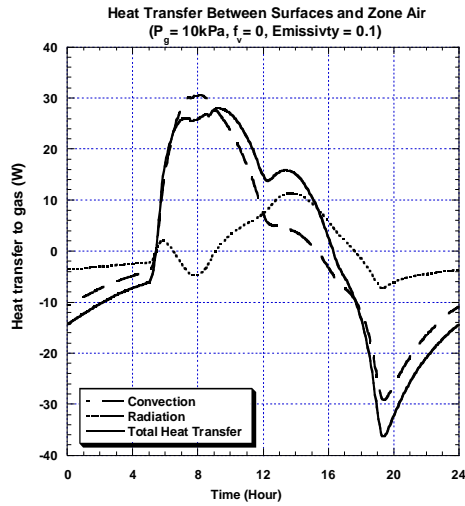


Figure 3.11b: Heat transfer (radiation, convection, and total) between surfaces and room air with an absorbing/emitting gas mixture only for case 1 with different emissivity.

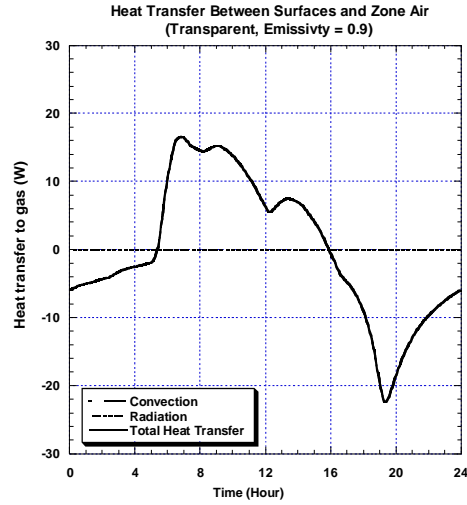
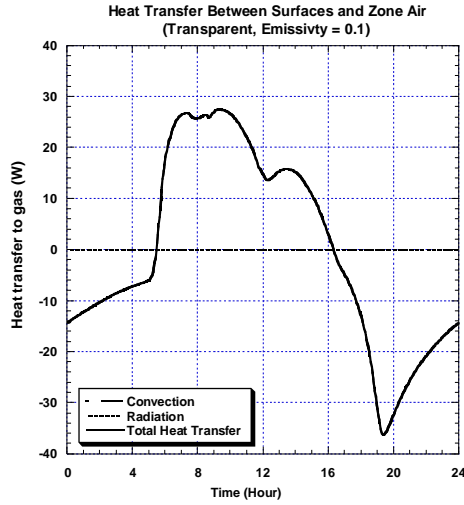


Figure 3.11c: Heat transfer (radiation, convection, and total) between surfaces and room air with a transparent medium for case 1 with different emissivity.

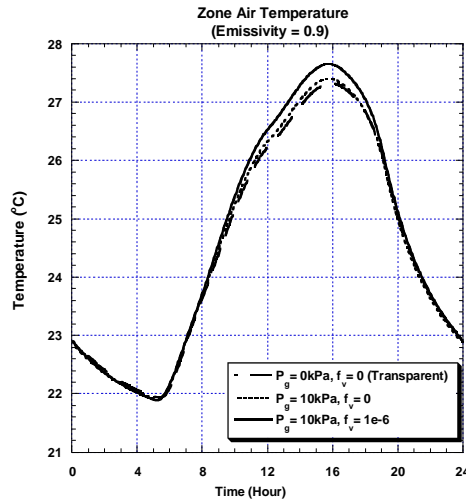
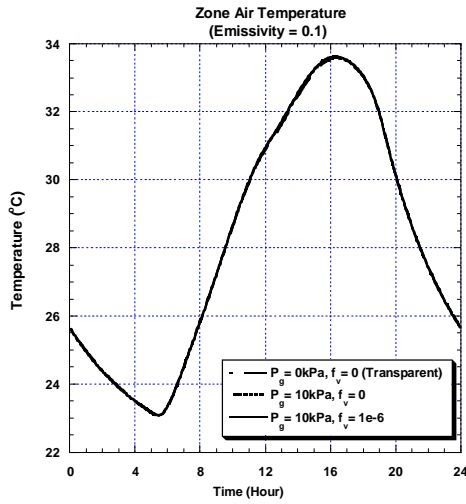


Figure 3.12: Temperature of the air within the room for the three modes of radiative absorption for case 1 with different emissivity.

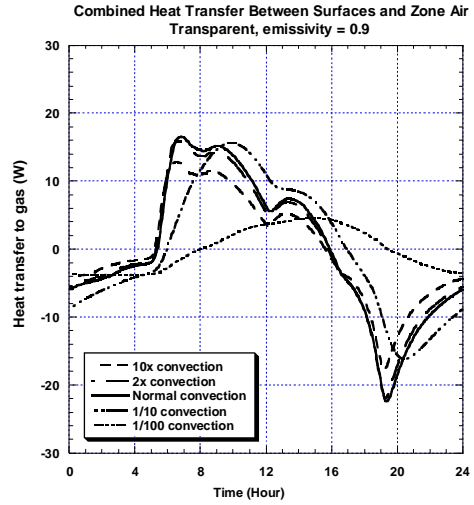
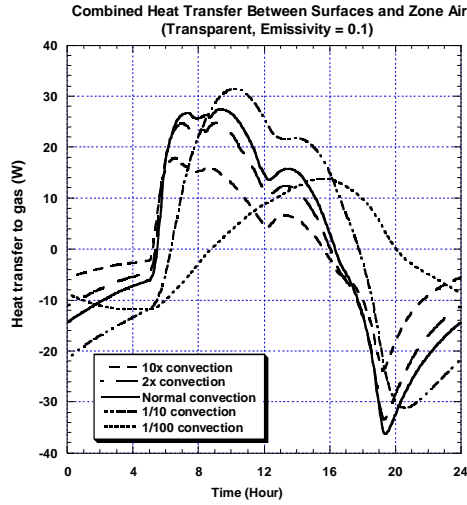


Figure 3.13a: Total heat transfer to the zone air for different level of convection heat transfer with different emissivity.

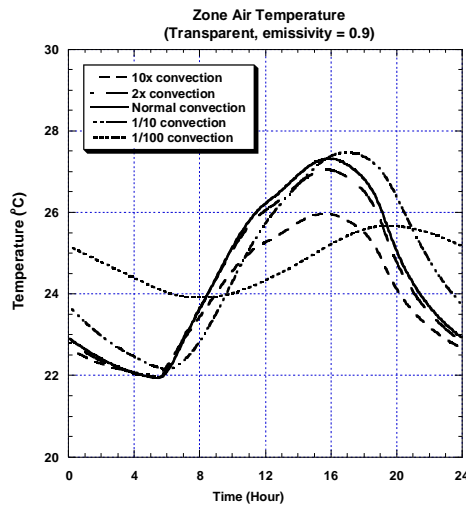
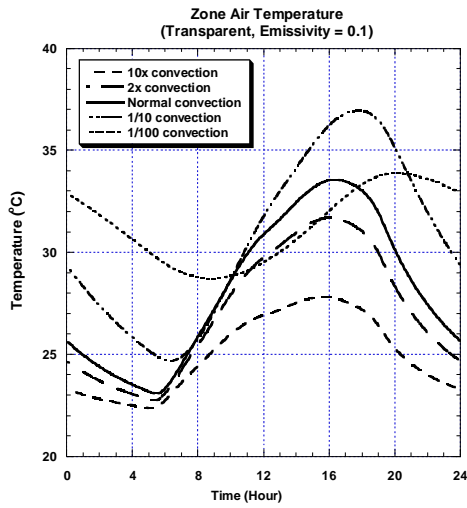


Figure 3.13b: Temperature of the zone air for different level of convective heat transfer with different emissivity.

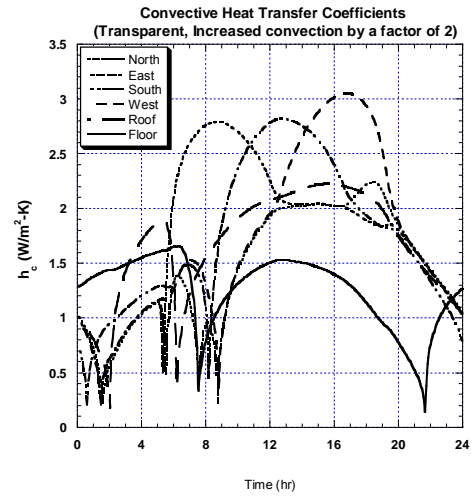
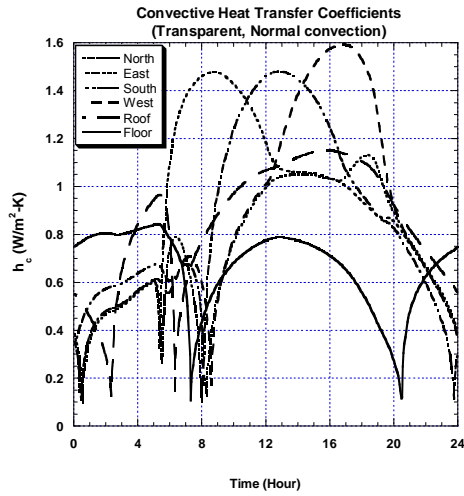


Figure 3.14: Convective heat transfer coefficients to the different surfaces for the case with normal convection and increased convection (by a factor of 2).

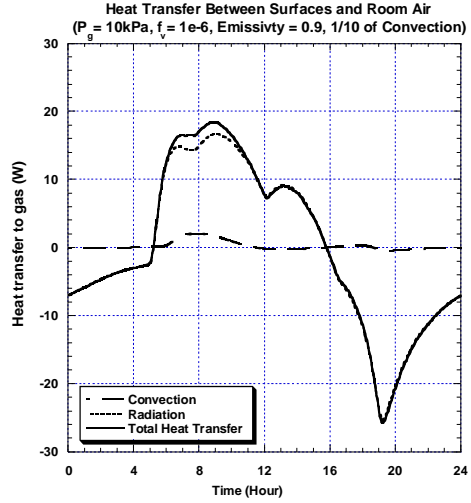
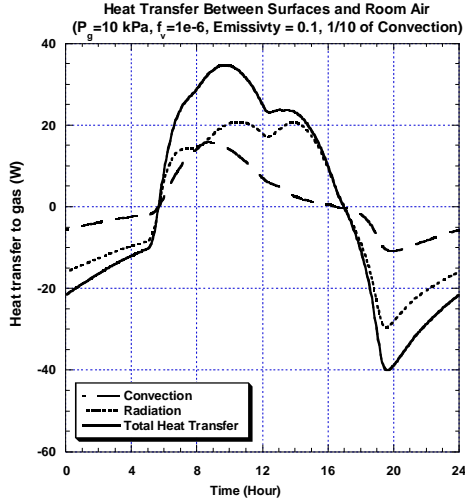


Figure 3.15a: Heat transfer (radiation, convection, and total) between surfaces and room air with an absorbing/emitting gas/particle mixture for case 1 with reduced convection (1/10) and different emissivity.

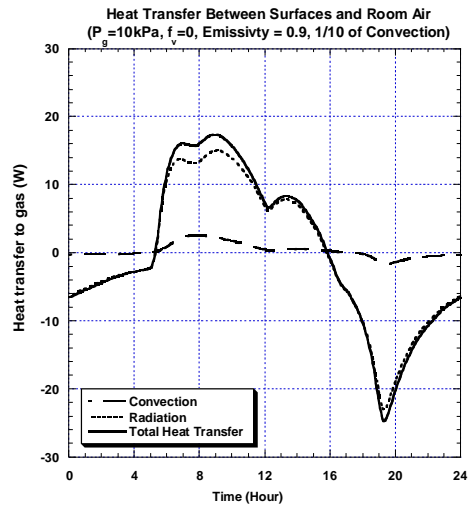
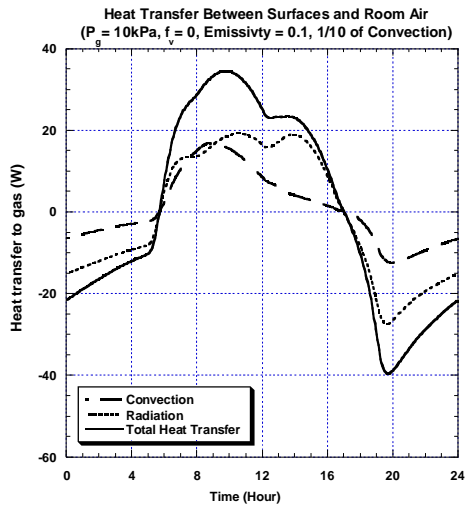


Figure 3.15b: Heat transfer (radiation, convection, and total) between surfaces and room air with an absorbing/emitting gas mixture only for case 1 with reduced convection (1/10) and different emissivity.

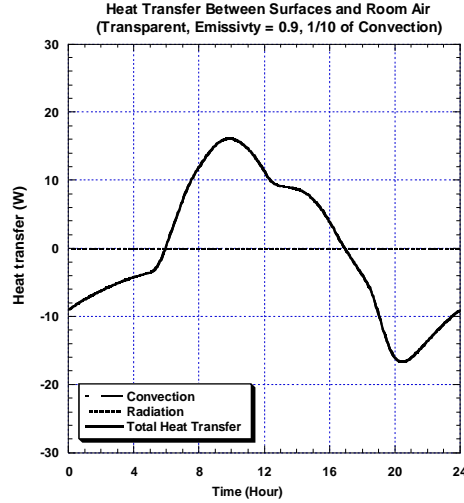
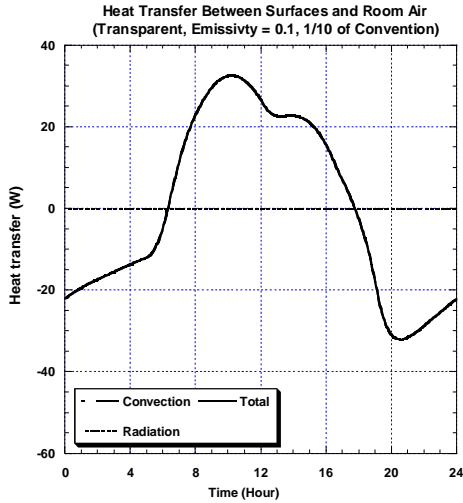


Figure 3.15c: Heat transfer (radiation, convection, and total) between surfaces and room air with a transparent medium for case 1 with reduced convection (1/10) and different emissivity.

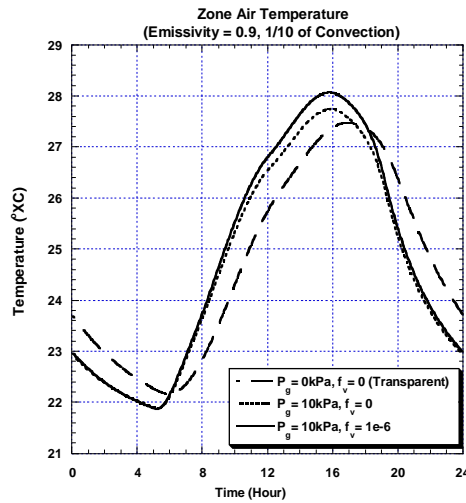
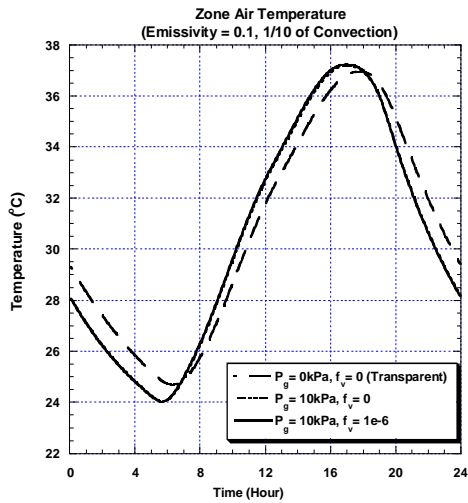


Figure 3.16: Temperature of the air within the room for the three modes of radiative absorption for case 1 with reduced convection (1/10) and different emissivity.

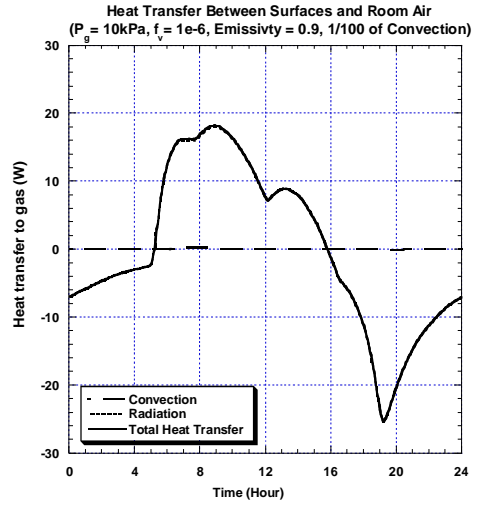
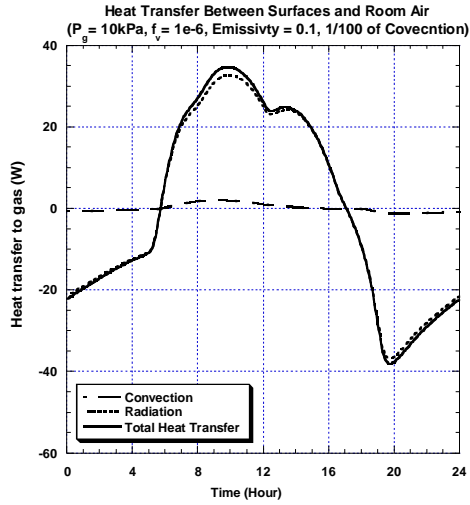


Figure 3.17a: Heat transfer (radiation, convection, and total) between surfaces and room air with an absorbing/emitting gas/particle mixture for case 1 with reduced convection (1/100) and different emissivity.

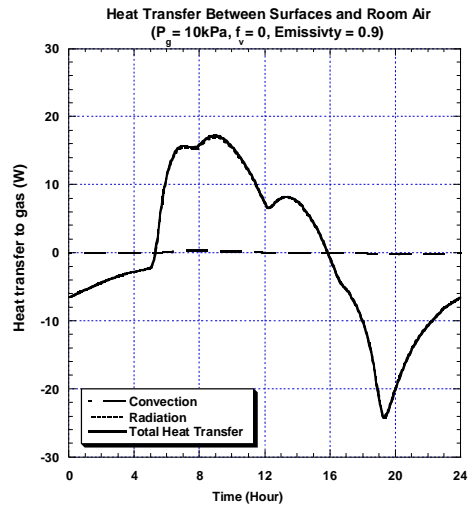
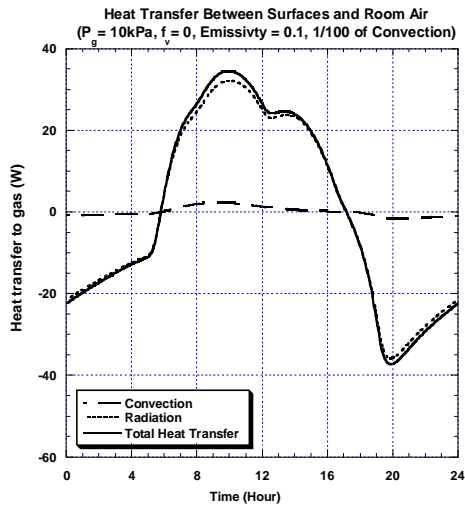


Figure 3.17b: Heat transfer (radiation, convection, and total) between surfaces and room air with an absorbing/emitting gas mixture only for case 1 with reduced convection (1/100) and different emissivity.

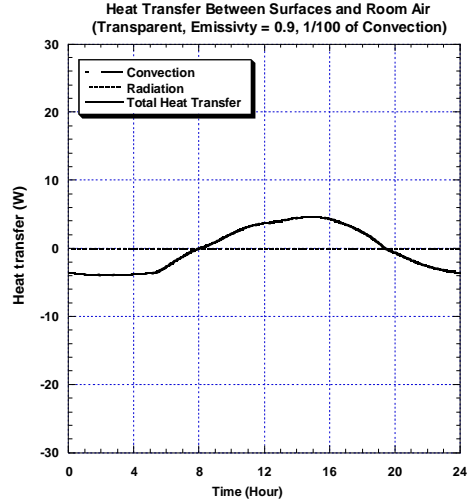
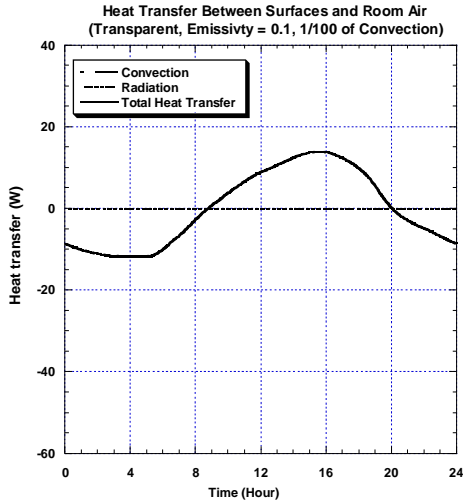


Figure 3.17c: Heat transfer (radiation, convection, and total) between surfaces and room air with a transparent medium for case 1 with reduced convection (1/100) and different emissivity.

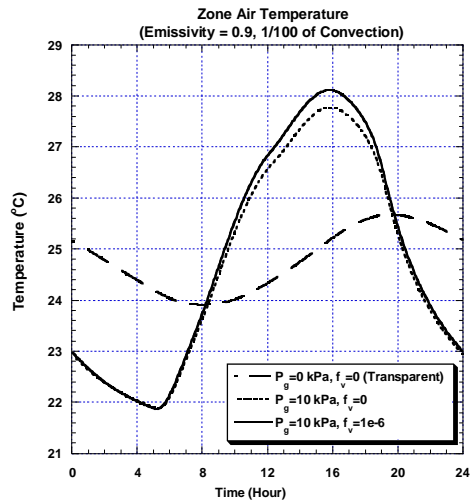
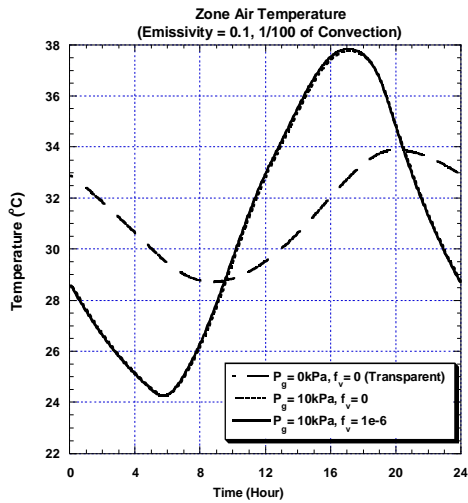


Figure 3.18: Temperature of the air within the room for the three modes of radiative absorption for case 1 with reduced convection (1/100) and different emissivity.

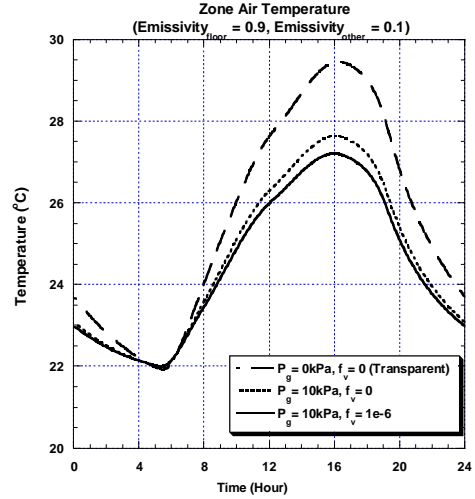
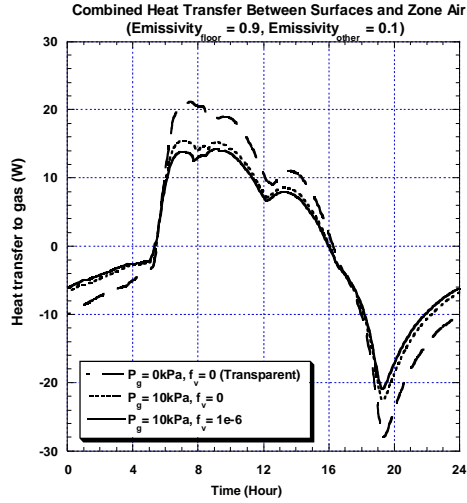


Figure 3.19: Heat transfer to the zone air and the air temperature within the room for the three modes of radiative absorption for case 1 with $\epsilon_{\text{floor}} = 0.9$ and $\epsilon_{\text{other-surfaces}} = 0.1$.

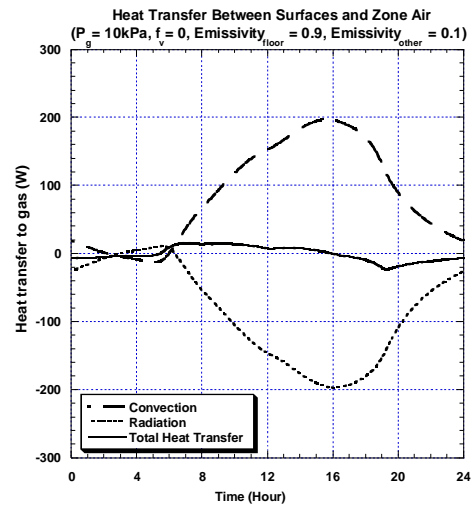
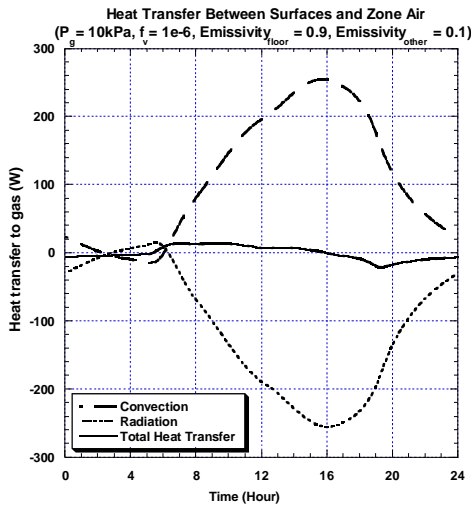


Figure 3.20: Heat transfer (radiation, convection, and total) between surfaces and room air with the two absorbing/emitting mixtures for case with $\epsilon_{\text{floor}} = 0.9$ and $\epsilon_{\text{other-surfaces}} = 0.1$.

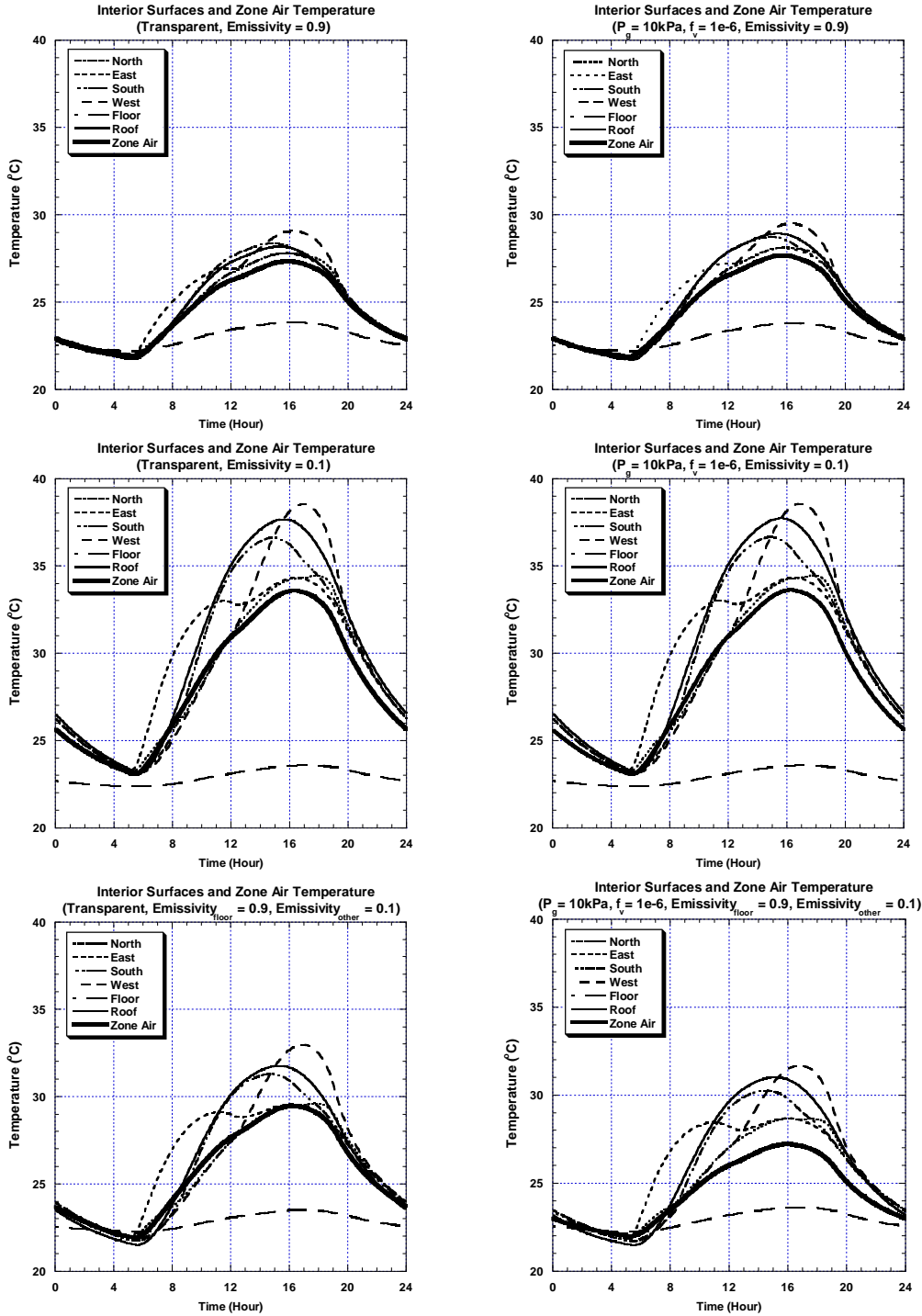


Figure 3.21: Comparison of the temperature at the difference surfaces and the zone air temperature for cases with different emissivity, transparent .vs. absorbing/emitting gas/particle mixtures.

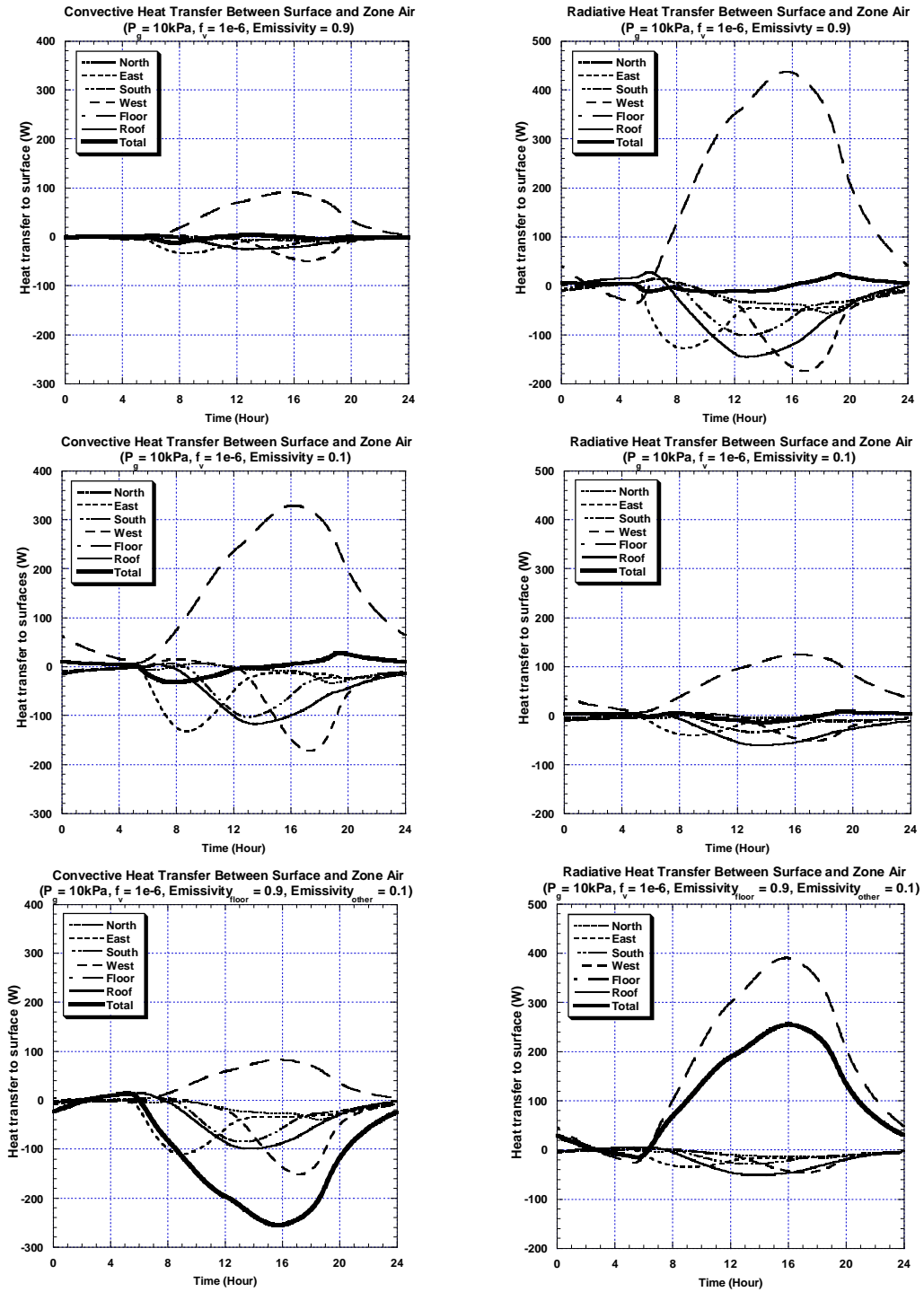


Figure 3.22: Comparison of the convective and radiative heat transfer from the difference surfaces to the zone air for cases with different emissivity with an absorbing/emitting gas/particle mixture.

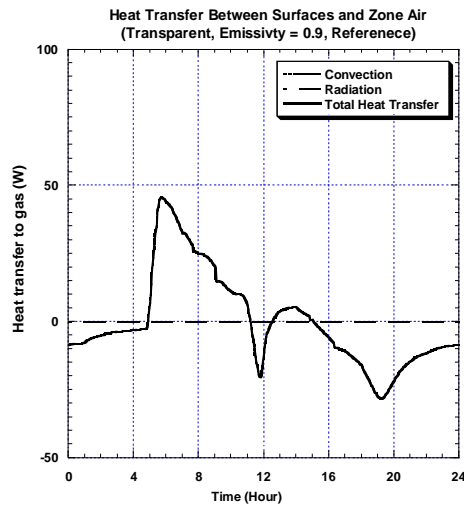
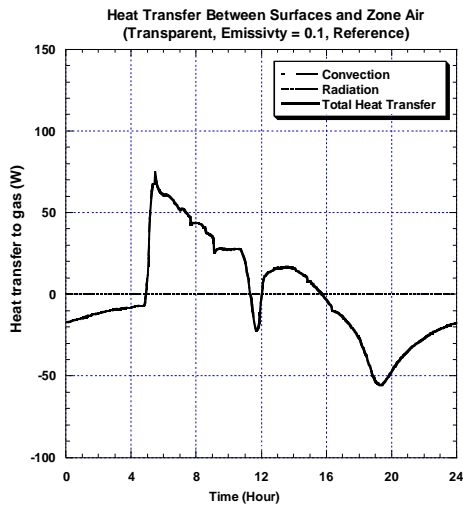


Figure 3.23: Heat transfer (radiation, convection, and total) between surfaces and room air with transparent medium for the reference case with different emissivity.

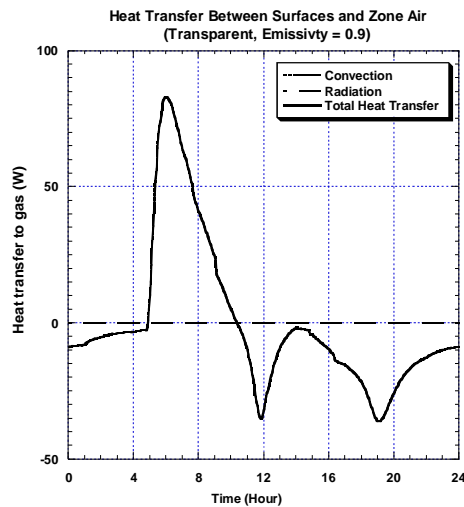
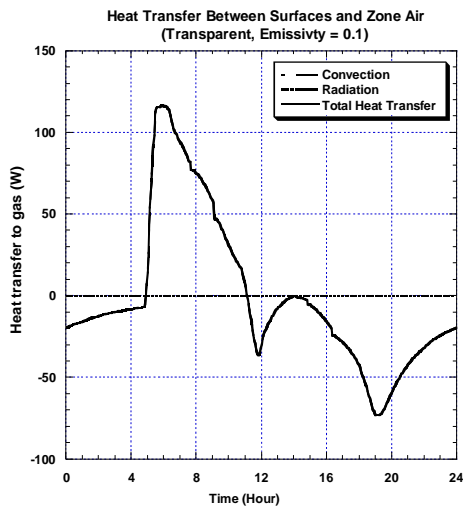


Figure 3.24a: Heat transfer (radiation, convection, and total) between surfaces and room air with transparent medium for different emissivity

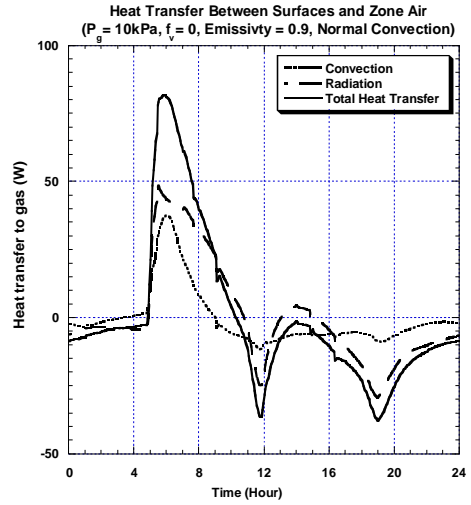
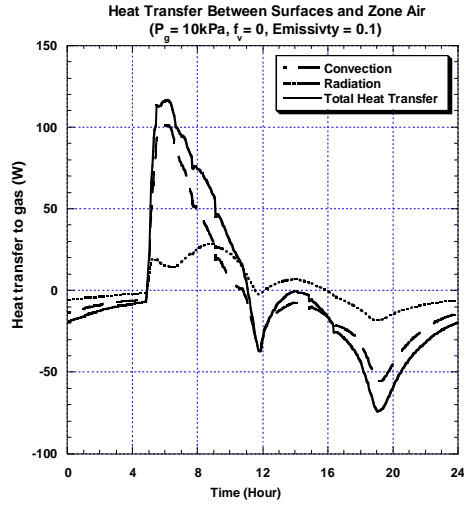


Figure 3.24b: Heat transfer (radiation, convection, and total) between surfaces and room air with an absorbing/emitting gas mixture only for different emissivity.

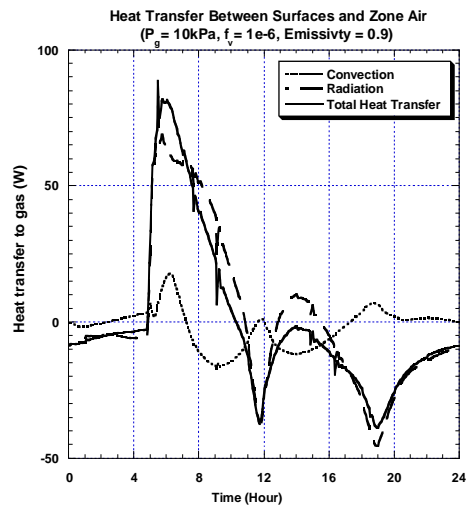
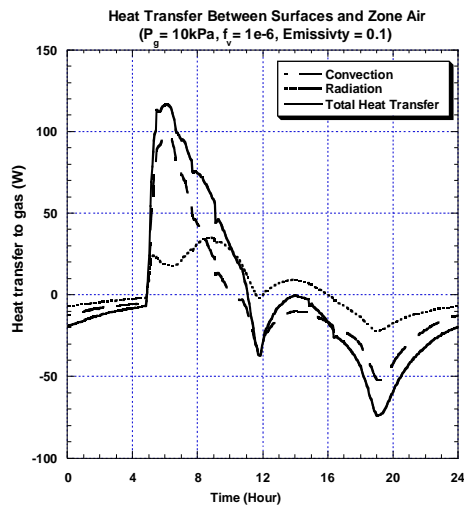


Figure 3.24c: Heat transfer (radiation, convection, and total) between surfaces and room air with an absorbing/emitting gas/particle mixture for different emissivity.

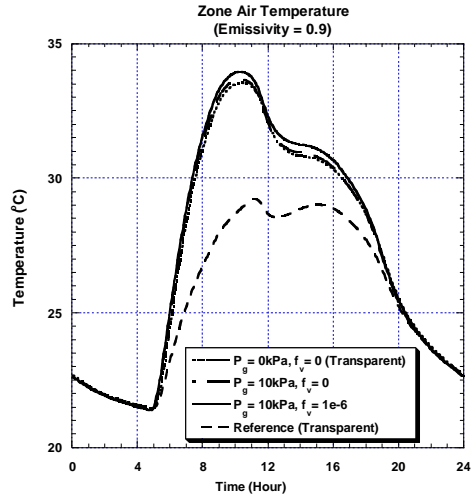
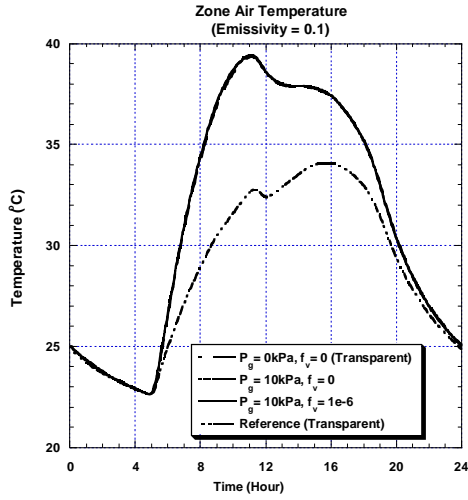


Figure 3.25: Temperature of the air within the room for the reference case and the three modes of radiative heat transfer with different emissivity.

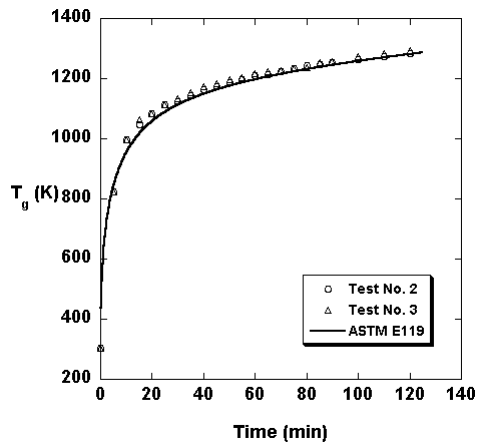


Figure 4.1: Comparison between the measured furnace temperature and the ASTM E119 time-temperature curve used in the calculation.

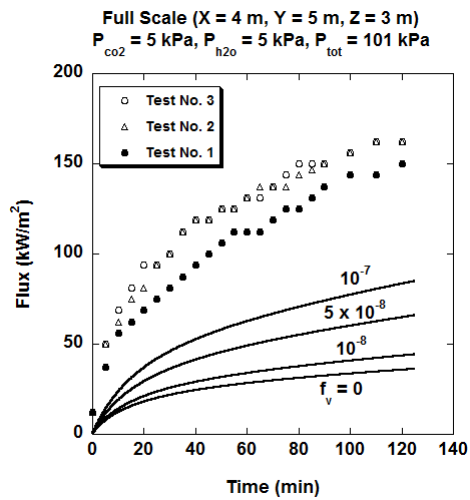


Figure 4.2: Comparison between the measured heat flux to the test specimen at the full-scale fire resistance furnace and the predicted radiative heat flux from the emission of combustion products only.

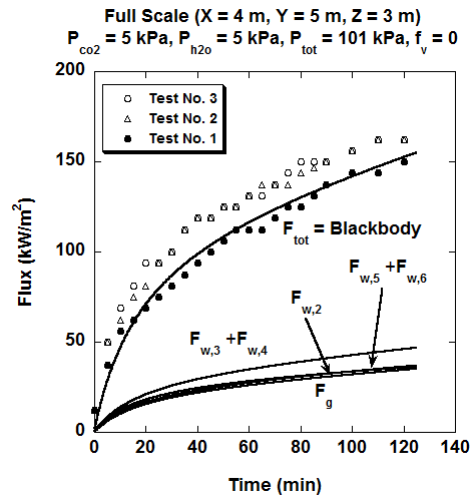


Figure 4.3a: Prediction of heat flux from the different walls and the heat flux from the combustion mixture to the test specimen with $f_v = 0.0$. The wall temperature is assumed to be identical to the temperature of the mixture.

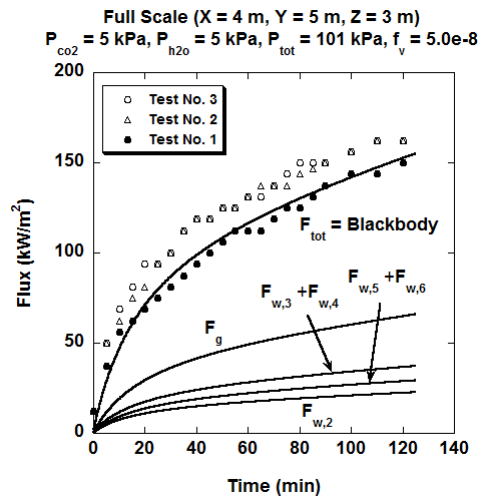


Figure 4.3b: Prediction of heat flux from the different walls and the heat flux from the combustion mixture to the test specimen with $f_v = 5.0\text{e-}8$. The wall temperature is assumed to be identical to the temperature of the mixture.

Appendix A

Neural Network Correlation for the Evaluation of Mean Beam Lengths for Radiative Heat Transfer between Perpendicular Surfaces in a Rectangular Enclosure

A three layer network, as shown in Figure A1, is used as a basis for the neural network development. The choice of a three layer network is based on the practical need to maintain the number of neurons needed for an accurate correlation to a reasonable value (say, less than 20). Numerical experiments show a three layer structure is adequate for the mean beam length data under consideration for the range of physical parameters under consideration. A “hyperbolic tangent sigmoid” function is used as the transfer function for the first two layers while a linear transfer function is used for the third layer. Using the Levenberg-Marquardt algorithm (1995), a neural network with a set of S_1, S_2 and S_3 neurons in the three layer can be “trained” to yield the values of the three weight matrices $\tilde{W}^1, \tilde{W}^2, \tilde{W}^3$ and three bias vectors $\vec{b}^1, \vec{b}^2, \vec{b}^3$ which would minimize the error between the network prediction and actual data. For the current neural network, the output vector is a scalar (mean beam length) and therefore $S_3 = 1$. Mathematically, the predicted value of the normalized output, a^3 , for a given normalized input vector \vec{p} with the currently selected set of transfer function, is given by:

$$a^3 = \sum_{i=1}^{S_3} a_i^2 W_i^3 + b^3 \quad (\text{A.1})$$

with

$$a_i^2 = \tanh \left[\left(\sum_{j=1}^{S_1} W_{ij}^2 a_j^1 \right) + b_i^2 \right], \quad i = 1, \dots, S_2 \quad (\text{A.2})$$

$$a_i^1 = \tanh \left[\left(\sum_{j=1}^N W_{ij}^1 p_j \right) + b_i^1 \right], \quad i = 1, \dots, S_1 \quad (\text{A.3})$$

and $N = 4$ being the dimension of the normalized input vector.

Two separate networks are developed for the two optical thicknesses $P_g L_{c,ij} = 10, 30 \text{ kPa}\cdot\text{m}$. The input vector, \vec{p} , is generated from the vector $(F_{CO_2}, f_v L_{c,ij}, T_w, T_g)$, normalized to $(-1.0 < p_i < 1.0)$ covering the following range:

$$\begin{aligned} 0 &\leq F_{CO_2} \leq 1.0 \\ 0 &\leq f_v L_{c,ij} \leq 5.0e-7 \text{ m} \\ 300K &\leq T_w, T_g \leq 1400K \end{aligned} \quad (\text{A.4})$$

and the output vector is

$$a^3 = \frac{L_{m,ij}}{L_{c,ij}} \quad (\text{A.5})$$

Numerical data for the scalar bias element b^3 and the maximum, minimum values of a^3 , for the three orientations, are shown in Table A1. Note that the range of the dimensionless mean beam length is quite large. This reflects the need for a neural network to correlate the dimensionless mean beam length. Numerical values of the different neural network elements are shown in the remaining tables.

List of Tables (Appendix A)

Table A1: The scalar bias parameter b^3 , the required neurons number S_1, S_2 , and the minimum, maximum values of the dimensionless mean beam length for different geometry and gas optical thicknesses.....	A-7
Table A2.1: Values of the weight matrix W_{ij}^1 between A_1, A_2 and A_3, A_4 with $P_g L_{c,ij} = 10$ kPa-m.....	A-8
Table A2.2: Values of the weight matrix W_{ij}^2 between A_1, A_2 and A_3, A_4 with $P_g L_{c,ij} = 10$ kPa-m.....	A-9
Table A2.2: Values of the weight matrix W_{ij}^2 between A_1, A_2 and A_3, A_4 with $P_g L_{c,ij} = 10$ kPa-m (continued)	A-10
Table A2.2: Values of the weight matrix W_{ij}^2 between A_1, A_2 and A_3, A_4 with $P_g L_{c,ij} = 10$ kPa-m (continued)	A-11
Table A2.2: Values of the weight matrix W_{ij}^2 between A_1, A_2 and A_3, A_4 with $P_g L_{c,ij} = 10$ kPa-m (continued)	A-12
Table A2.3: Values of the vectors W^3, b^1, b^2 between A_1, A_2 and A_3, A_4 with $P_g L_{c,ij} = 10$ kPa-m.....	A-13
Table A3.1: Values of the weight matrix W_{ij}^1 between A_1, A_2 and A_3, A_4 with $P_g L_{c,ij} = 30$ kPa-m.....	A-14
Table A3.2: Values of the weight matrix W_{ij}^2 between A_1, A_2 and A_3, A_4 with $P_g L_{c,ij} = 30$ kPa-m.....	A-15
Table A3.2: Values of the weight matrix W_{ij}^2 between A_1, A_2 and A_3, A_4 with $P_g L_{c,ij} = 30$ kPa-m (continued)	A-16

Table A3.2: Values of the weight matrix W_{ij}^2 between A_1, A_2 and A_3, A_4 with $P_g L_{c,ij} = 30$ kPa-m (continued).....	A-17
Table A3.2: Values of the weight matrix W_{ij}^2 between A_1, A_2 and A_3, A_4 with $P_g L_{c,ij} = 30$ kPa-m (continued).....	A-18
Table A3.3: Values of the vectors W^3, b^1, b^2 between A_1, A_2 and A_3, A_4 with $P_g L_{c,ij} = 30$ kPa-m.	A-19
Table A4.1: Values of the weight matrix W_{ij}^1 between A_1, A_2 and A_5, A_6 with $P_g L_{c,ij} = 10$ kPa-m.	A-20
Table A4.2: Values of the weight matrix W_{ij}^2 between A_1, A_2 and A_5, A_6 with $P_g L_{c,ij} = 10$ kPa-m.	A-21
Table A4.2: Values of the weight matrix W_{ij}^2 between A_1, A_2 and A_5, A_6 with $P_g L_{c,ij} = 10$ kPa-m (continued).....	A-22
Table A4.2: Values of the weight matrix W_{ij}^2 between A_1, A_2 and A_5, A_6 with $P_g L_{c,ij} = 10$ kPa-m (continued).....	A-23
Table A4.2: Values of the weight matrix W_{ij}^2 between A_1, A_2 and A_5, A_6 with $P_g L_{c,ij} = 10$ kPa-m (continued).....	A-24
Table A4.3: Values of the vectors W^3, b^1, b^2 between A_1, A_2 and A_5, A_6 with $P_g L_{c,ij} = 10$ kPa-m.	A-25
Table A5.1: Values of the weight matrix W_{ij}^1 between A_1, A_2 and A_5, A_6 with $P_g L_{c,ij} = 30$ kPa-m.	A-26
Table A5.2: Values of the weight matrix W_{ij}^2 between A_1, A_2 and A_5, A_6 with $P_g L_{c,ij} = 30$ kPa-m.	A-27

Table A5.2: Values of the weight matrix W_{ij}^2 between A_1, A_2 and A_5, A_6 with $P_g L_{c,ij} = 30$ kPa-m (continued).....	A-28
Table A5.2: Values of the weight matrix W_{ij}^2 between A_1, A_2 and A_5, A_6 with $P_g L_{c,ij} = 30$ kPa-m (continued).....	A-29
Table A5.2: Values of the weight matrix W_{ij}^2 between A_1, A_2 and A_5, A_6 with $P_g L_{c,ij} = 30$ kPa-m (continued).....	A-30
Table A5.3: Values of the vectors W^3, b^1, b^2 between A_1, A_2 and A_5, A_6 with $P_g L_{c,ij} = 30$ kPa-m.....	A-31
Table A6.1: Values of the weight matrix W_{ij}^1 between A_3, A_4 and A_5, A_6 with $P_g L_{c,ij} = 10$ kPa-m.....	A-32
Table A6.2: Values of the weight matrix W_{ij}^2 between A_3, A_4 and A_5, A_6 with $P_g L_{c,ij} = 10$ kPa-m.....	A-33
Table A6.2: Values of the weight matrix W_{ij}^2 between A_3, A_4 and A_5, A_6 with $P_g L_{c,ij} = 10$ kPa-m (continued).....	A-34
Table A6.2: Values of the weight matrix W_{ij}^2 between A_3, A_4 and A_5, A_6 with $P_g L_{c,ij} = 10$ kPa-m (continued).....	A-35
Table A6.3: Values of the vectors W^3, b^1, b^2 between A_3, A_4 and A_5, A_6 with $P_g L_{c,ij} = 10$ kPa-m (continued).....	A-36
Table A7.1: Values of the weight matrix W_{ij}^1 between A_3, A_4 and A_5, A_6 with $P_g L_{c,ij} = 30$ kPa-m.....	A-37
Table A7.2: Values of the weight matrix W_{ij}^2 between A_3, A_4 and A_5, A_6 with $P_g L_{c,ij} = 30$ kPa-m.....	A-38

Table A7.2: Values of the weight matrix W_{ij}^2 between A_3, A_4 and A_5, A_6 with $P_g L_{c,ij} = 30$ kPa-m (continued).....	A-39
Table A7.2: Values of the weight matrix W_{ij}^2 between A_3, A_4 and A_5, A_6 with $P_g L_{c,ij} = 30$ kPa-m (continued).....	A-40
Table A7.2: Values of the weight matrix W_{ij}^2 between A_3, A_4 and A_5, A_6 with $P_g L_{c,ij} = 30$ kPa-m (continued).....	A-41
Table A7.3: Values of the vectors W^3, b^1, b^2 between A_3, A_4 and A_5, A_6 with $P_g L_{c,ij} = 10$ kPa-m (continued).....	A-42

i	j	$P_g L_{c,ij}$ (kPa-m)	S_1	S_2	b^3	a_{\min}^3 a_{\max}^3
1,2	3,4	10	19	17	-0.244	0.0717 1.000
1,2	3,4	30	20	17	0.703	0.0697 0.995
1,2	5,6	10	19	16	-0.755	0.105 0.996
1,2	5,6	30	19	16	0.614	0.0952 0.996
3,4	5,6	10	19	16	1.281	0.123 0.995
3,4	5,6	30	19	15	-0.0277	0.100 0.999

Table A1: The scalar bias parameter b^3 , the required neurons number S_1 , S_2 , and the minimum, maximum values of the dimensionless mean beam length for different geometry and gas optical thicknesses.

	j = 1	2	3	4
i = 1	-3.122E-01	1.128E+00	-7.700E-01	7.218E-02
2	-2.194E+00	-2.318E+00	5.452E-01	-1.650E-01
3	-1.663E+00	-1.318E+00	1.309E+00	-2.102E+00
4	-1.080E+00	-2.951E+00	-2.404E-01	6.781E-01
5	8.019E-01	2.773E+00	2.697E+00	3.374E+00
6	3.582E-01	3.066E-01	-2.065E+00	2.537E-01
7	-1.687E+00	-1.420E+00	6.749E-01	2.126E+00
8	1.454E+00	9.651E-01	1.295E+00	-3.617E-01
9	-1.557E+00	2.482E-01	-1.966E+00	-2.866E-01
10	7.681E-01	1.361E+00	1.276E+00	8.042E-01
11	-1.314E+00	2.791E-01	-1.736E+00	-1.938E+00
12	-6.006E-01	-1.127E+00	-3.381E-01	5.805E-01
13	-4.374E-01	-2.324E-01	1.494E+00	-2.266E+00
14	2.651E+00	-3.197E-01	-2.198E+00	-6.596E-01
15	2.767E-01	1.296E+00	9.740E-01	4.724E-01
16	3.903E-01	5.860E-01	9.135E-01	-1.904E+00
17	-4.714E-01	-7.262E-01	1.334E+00	-2.459E+00
18	-2.836E+00	4.505E-02	7.352E-01	2.959E-01
19	6.561E-01	-2.610E+00	-1.903E+00	-1.801E+00

Table A2.1: Values of the weight matrix W_{ij}^1 between A_1 , A_2 and A_3 , A_4 with
 $P_g L_{c,ij} = 10$ kPa-m.

	j = 1	2	3	4	5
i = 1	-2.693E-01	-8.248E-01	-5.296E-02	1.905E-01	-1.958E-01
2	1.058E+00	-9.319E-01	-1.889E-01	-6.490E-01	-1.523E+00
3	4.789E-01	-2.680E-01	-1.829E+00	-6.021E-01	3.688E-01
4	-5.379E-01	7.109E-02	2.342E-01	7.247E-01	-4.752E-01
5	-9.266E-02	-3.331E-01	-1.499E-01	-7.733E-01	-3.639E-01
6	-3.413E-01	1.565E+00	2.171E-01	-7.862E-01	2.490E-01
7	2.653E-01	5.246E-02	-1.395E-01	8.669E-02	-3.190E-01
8	3.826E-01	-1.374E+00	-7.351E-03	5.694E-01	-8.851E-01
9	-8.873E-01	-2.880E-01	-1.127E+00	2.595E-01	3.199E-01
10	6.334E-01	-5.583E-01	-1.837E-01	-5.944E-01	4.852E-01
11	9.587E-01	3.065E-01	9.751E-01	8.555E-01	-4.907E-01
12	-4.935E-01	6.713E-01	2.339E-01	-7.962E-01	6.069E-01
13	8.383E-02	-1.923E-01	-8.856E-02	-1.028E+00	-6.065E-01
14	6.273E-02	2.503E-02	-9.057E-01	-2.151E+00	1.309E-01
15	-2.506E-01	9.787E-02	-1.476E-01	-1.194E+00	-5.605E-01
16	-6.290E-01	-1.026E+00	1.056E-02	3.724E-01	1.895E-01
17	4.237E-01	1.293E+00	1.063E+00	-5.353E-02	1.512E-01

Table A2.2: Values of the weight matrix W_{ij}^2 between A_1, A_2 and A_3, A_4 with
 $P_g L_{c,ij} = 10$ kPa-m.

	j = 6	7	8	9	10
i = 1	-4.790E-01	1.675E-01	1.065E+00	9.854E-02	-2.899E-01
2	-8.884E-02	7.275E-02	-5.649E-01	7.128E-01	-3.880E-01
3	4.392E-01	-1.469E+00	1.354E+00	5.366E-01	-4.759E-01
4	1.678E-01	1.373E-01	-7.452E-01	-7.274E-01	5.978E-01
5	-5.978E-03	-1.103E-03	2.314E-01	-3.002E-02	5.719E-02
6	-2.761E-01	-2.613E-02	2.873E-01	4.785E-01	-1.047E-01
7	3.665E-01	3.710E-02	-2.006E-01	-2.948E-01	6.510E-02
8	-1.446E-01	1.571E-01	7.523E-01	-5.381E-01	2.997E-01
9	1.495E+00	-2.004E-01	1.212E+00	7.740E-01	5.180E-01
10	-6.447E-02	-4.961E-02	-4.312E-01	-8.790E-01	1.253E-01
11	-3.185E-01	4.973E-01	3.537E-02	2.775E-01	-4.947E-01
12	-4.931E-01	-5.838E-02	-6.027E-01	6.031E-01	-2.904E-01
13	-4.848E-01	1.495E-01	6.284E-01	8.570E-02	1.803E-01
14	8.184E-02	-9.032E-01	6.431E-03	1.711E-01	-4.283E-02
15	-2.758E-01	-1.844E-01	-5.132E-01	-2.142E-01	3.743E-01
16	1.354E+00	-2.906E-01	9.847E-01	-4.510E-01	4.407E-01
17	-1.300E+00	7.336E-03	-1.191E+00	-1.010E+00	2.599E-02

Table A2.2: Values of the weight matrix W_{ij}^2 between A_1, A_2 and A_3, A_4 with
 $P_g L_{c,ij} = 10$ kPa-m (continued)

	j = 11	12	13	14	15
i = 1	-1.025E-01	-8.336E-02	9.143E-01	-1.366E-01	3.707E-01
2	-2.009E-02	-4.769E-01	3.510E-01	-6.118E-01	-4.598E-01
3	1.141E-01	-7.458E-01	5.124E-01	-1.096E+00	-3.379E-01
4	1.103E-01	-8.385E-02	7.094E-01	2.986E-01	2.085E-02
5	-3.059E-02	2.067E-01	-5.961E-01	-2.808E-01	-6.911E-02
6	-1.336E-01	3.260E-01	-4.060E-01	-2.200E-01	1.961E-01
7	7.431E-02	-3.520E-02	1.398E-01	-1.195E-01	-1.953E-01
8	3.644E-01	2.559E-01	-6.856E-01	-7.357E-01	9.294E-02
9	3.337E-01	-3.370E-01	2.397E-01	2.242E-01	-6.211E-01
10	-3.512E-03	7.680E-01	-6.392E-01	3.998E-01	-1.400E+00
11	-5.300E-01	5.272E-02	5.627E-01	8.164E-01	-8.819E-01
12	-2.202E-01	1.550E-02	4.833E-01	3.037E-01	3.058E-01
13	1.315E-01	1.010E-01	-1.091E+00	-7.459E-01	4.703E-01
14	-4.337E-01	6.840E-01	-1.555E+00	1.190E+00	-3.272E-02
15	6.623E-02	-2.943E-01	-4.618E-01	2.019E-01	-1.472E-02
16	-2.476E-01	2.528E-01	1.400E-01	1.308E+00	-5.148E-01
17	-1.185E-01	9.932E-01	6.924E-01	-4.785E-01	4.930E-01

Table A2.2: Values of the weight matrix W_{ij}^2 between A_1, A_2 and A_3, A_4 with $P_g L_{c,ij} = 10$ kPa-m (continued)

	j = 16	17	18	19
i = 1	1.585E-01	-7.704E-01	-5.125E-01	-2.640E-01
2	-8.168E-02	-1.386E-01	-8.903E-01	-1.119E+00
3	-1.266E+00	1.480E+00	6.872E-01	5.691E-01
4	7.455E-02	-6.775E-01	8.159E-01	-7.972E-01
5	5.716E-02	5.938E-01	-5.878E-01	5.672E-01
6	-7.964E-02	4.450E-01	-9.071E-01	-7.752E-01
7	3.339E-02	-1.387E-01	-2.252E-01	6.809E-01
8	-1.969E-03	9.709E-01	-6.136E-01	2.215E-01
9	2.337E-01	4.802E-01	-1.832E-02	1.906E-01
10	3.021E-02	-2.807E-01	3.484E-01	6.431E-01
11	8.137E-01	2.133E-02	4.274E-01	-3.581E-01
12	-7.630E-02	-5.416E-01	-4.791E-01	-7.892E-01
13	1.658E-02	1.385E+00	-1.190E+00	3.725E-01
14	-4.753E-01	3.019E+00	4.035E-01	9.564E-01
15	2.463E-02	5.039E-01	8.123E-01	5.415E-01
16	2.358E-01	-2.944E-01	2.953E-02	-1.854E-01
17	-5.262E-02	-4.102E-01	-1.032E-01	-1.957E-01

Table A2.2: Values of the weight matrix W_{ij}^2 between A_1, A_2 and A_3, A_4 with $P_g L_{c,ij} = 10$ kPa-m (continued)

	w^3	b^1	b^2
i = 1	-8.623E-01	1.571E+00	1.698E+00
2	3.757E-01	4.424E+00	-1.069E+00
3	-2.368E+00	2.245E+00	1.435E+00
4	7.132E-01	2.884E+00	7.891E-01
5	2.529E+00	-3.120E+00	4.570E-01
6	-1.835E+00	-1.184E+00	-6.058E-02
7	-2.045E+00	2.017E+00	-9.186E-01
8	1.332E+00	-1.645E+00	-6.746E-01
9	1.852E+00	4.086E-01	-3.970E-01
10	-1.077E-01	2.258E-01	-5.914E-01
11	6.131E-01	-4.081E-01	6.796E-01
12	1.617E+00	2.773E-02	6.416E-01
13	-9.612E-01	-1.862E+00	-6.232E-01
14	2.857E+00	2.381E+00	-1.465E+00
15	-5.865E-01	7.066E-01	9.572E-01
16	-9.175E-01	1.394E+00	-1.105E+00
17	1.430E+00	-2.290E+00	1.316E+00
18		-3.116E+00	
19		3.477E+00	

Table A2.3: Values of the vectors W^3, b^1, b^2 between A_1, A_2 and A_3, A_4 with $P_g L_{c,ij} = 10$ kPa-m.

	j = 1	2	3	4
i = 1	1.930E+00	1.880E+00	1.954E+00	-1.515E+00
2	3.951E-01	-8.668E-01	-1.443E+00	8.238E-01
3	-2.476E-01	-1.808E-01	2.726E+00	1.543E-03
4	-2.461E+00	4.035E-01	-1.483E-01	7.463E-01
5	2.478E+00	-8.097E-01	1.239E+00	-1.109E+00
6	-7.306E-01	1.871E+00	-7.860E-01	1.305E+00
7	1.744E+00	-7.806E-01	-1.537E+00	1.894E-02
8	7.296E-01	1.393E+00	5.978E-01	-4.563E-01
9	-2.140E-01	-2.266E+00	2.440E+00	1.149E+00
10	-1.781E-02	-1.189E+00	-3.970E-01	-4.932E-01
11	2.123E+00	5.482E-02	-3.272E+00	1.231E+00
12	5.392E-01	1.364E+00	7.036E-01	-1.448E-01
13	-7.190E-01	8.907E-01	-5.020E-01	-8.186E-01
14	8.399E-01	3.201E-01	-1.087E+00	1.299E+00
15	6.465E-01	-9.560E-01	2.049E+00	9.676E-01
16	2.774E+00	2.652E-01	5.697E-01	1.785E+00
17	5.467E-01	1.160E+00	9.493E-01	3.194E+00
18	-2.633E-01	-1.971E+00	5.512E-01	1.823E-01
19	1.398E+00	1.467E+00	4.899E-02	-1.437E+00
20	2.955E+00	-7.065E-01	9.306E-02	-8.799E-02

Table A3.1: Values of the weight matrix W_{ij}^1 between A_1 , A_2 and A_3 , A_4 with

$$P_g L_{c,ij} = 30 \text{ kPa-m.}$$

	j = 1	2	3	4	5
i = 1	-4.925E-01	-3.342E-01	-2.055E-01	8.348E-01	1.747E-01
2	6.685E-01	9.394E-02	4.417E-01	-1.261E+00	-1.052E+00
3	1.031E-01	3.111E-01	8.575E-01	1.004E+00	4.293E-02
4	5.373E-01	1.567E-01	-8.133E-01	-3.988E-01	1.484E+00
5	2.790E-01	-2.071E-02	-5.046E-01	-1.043E-01	1.275E-01
6	-2.722E-02	-4.020E-01	8.360E-02	3.472E-01	3.021E-01
7	2.329E-01	3.236E-01	-4.217E-01	8.613E-03	-3.864E-01
8	5.707E-01	-3.489E-01	1.936E-01	-3.679E-01	-3.116E-01
9	-3.935E+00	-2.037E-01	7.894E-01	-3.723E-01	-3.421E+00
10	5.648E-02	1.210E-01	-8.921E-01	8.549E-01	-4.481E-01
11	5.500E-01	-1.436E-01	4.816E-01	-4.208E-01	-2.387E-01
12	-1.512E+00	-8.526E-01	7.623E-01	7.231E-02	-1.570E+00
13	2.802E-01	1.392E-01	-5.258E-01	-9.251E-02	1.834E-01
14	3.054E-01	1.058E-02	-3.325E-01	-1.637E-01	-2.589E-01
15	-7.206E-02	-2.380E-01	4.416E-01	1.725E-01	4.530E-01
16	4.527E-01	-1.069E-01	-2.949E-01	1.994E-01	3.634E-01
17	-3.828E-02	-1.106E-01	-2.893E-01	-8.839E-01	-5.867E-01

Table A3.2: Values of the weight matrix W_{ij}^2 between A_1, A_2 and A_3, A_4 with

$$P_g L_{c,ij} = 30 \text{ kPa-m}$$

	j = 6	7	8	9	10
i = 1	1.367E-01	2.617E-02	-1.160E+00	-3.270E-01	-1.503E+00
2	8.146E-01	-9.377E-02	-6.138E-02	1.008E-01	-4.305E-01
3	3.744E-01	-2.367E-01	-1.087E-01	2.516E-01	-3.921E-01
4	-1.601E-01	4.783E-01	4.335E-01	6.020E-01	-2.215E-01
5	-5.509E-01	-5.721E-01	5.828E-01	1.491E-01	-7.142E-01
6	-4.299E-01	-4.947E-01	-4.626E-01	1.307E-01	8.704E-02
7	-6.489E-02	-8.239E-01	-7.366E-01	-4.194E-01	-4.549E-01
8	2.248E-01	-1.089E-01	-2.219E-01	-2.219E-02	2.927E-01
9	-2.095E+00	6.756E-02	8.609E-01	1.663E+00	1.513E-01
10	5.116E-02	-1.064E+00	-1.662E+00	1.266E-01	-2.081E-01
11	-3.552E-01	1.921E-01	4.429E-01	-3.126E-01	4.341E-01
12	-8.368E-01	5.814E-01	3.897E-01	3.693E-01	9.846E-02
13	4.208E-01	3.104E-01	-8.844E-01	5.119E-01	-3.512E-01
14	2.422E-01	-1.893E-01	6.010E-01	1.330E-01	-4.188E-02
15	-4.497E-01	1.984E-02	9.731E-01	1.830E-01	4.218E-01
16	-3.371E-01	1.614E-01	1.015E+00	4.133E-01	9.711E-01
17	-7.129E-02	-2.188E-01	5.496E-01	-3.064E-01	-9.304E-01

Table A3.2: Values of the weight matrix W_{ij}^2 between A_1, A_2 and A_3, A_4 with

$$P_g L_{c,j} = 30 \text{ kPa-m (continued)}$$

	j = 11	12	13	14	15
i = 1	-6.778E-01	-8.410E-01	6.667E-01	4.991E-01	5.144E-01
2	4.755E-02	5.698E-02	4.049E-01	9.391E-02	-2.008E-01
3	5.177E-01	-4.424E-01	8.192E-01	8.032E-01	8.713E-01
4	1.042E-01	7.139E-01	1.717E-01	-6.084E-01	-8.200E-01
5	-4.311E-01	-2.937E-01	1.792E-01	1.897E-01	-2.621E-01
6	-1.224E-01	8.063E-01	-6.732E-02	-2.157E-01	-5.197E-01
7	1.557E-01	5.292E-01	2.933E-01	-2.637E-01	2.379E-02
8	2.067E-01	7.873E-02	-1.028E-01	1.984E-01	2.080E-01
9	-3.197E+00	-4.442E-01	-5.160E-01	2.143E+00	-1.161E+00
10	-4.579E-01	-4.315E-01	1.756E-01	-6.589E-01	-1.441E+00
11	-6.610E-01	-6.466E-01	-3.376E-02	-4.461E-01	1.814E-01
12	-1.131E+00	1.155E-01	1.235E-01	9.505E-01	7.770E-02
13	3.150E-01	1.111E-03	5.890E-01	-9.392E-03	-7.840E-01
14	2.905E-01	3.893E-01	1.830E-01	2.160E-01	-1.969E-01
15	-2.310E-01	3.016E-01	-7.709E-01	2.657E-02	2.581E-01
16	-4.556E-01	4.857E-01	-5.858E-01	6.831E-02	-3.588E-01
17	-2.278E-01	-3.292E-01	-8.580E-01	-2.067E-01	-5.509E-01

Table A3.2: Values of the weight matrix W_{ij}^2 between A_1 , A_2 and A_3 , A_4 with

$$P_g L_{c,ij} = 30 \text{ kPa-m (continued)}$$

	j = 16	17	18	19	20
i = 1	9.455E-01	-1.215E-01	1.578E+00	-4.173E-01	2.112E-01
2	-7.956E-02	2.810E-01	7.320E-02	-2.276E-01	5.834E-01
3	5.221E-01	-7.004E-01	1.454E-01	2.193E-02	-2.942E-01
4	-2.430E-01	2.731E-01	3.527E-01	-2.153E-01	6.607E-01
5	-8.723E-01	6.251E-01	5.429E-02	-3.507E-01	-9.296E-02
6	-1.746E-01	-3.733E-01	3.708E-01	7.201E-01	5.163E-03
7	-1.970E-01	-6.801E-01	2.298E-01	-2.167E-01	1.180E-01
8	-8.954E-02	3.265E-01	2.209E-01	-1.683E-01	3.545E-01
9	2.797E+00	-1.866E+00	-3.875E-01	3.694E-01	-1.178E+00
10	4.330E-02	-2.511E-01	1.050E-01	6.839E-01	6.985E-01
11	3.272E-01	-3.752E-02	1.286E-01	2.997E-01	-4.343E-01
12	-7.354E-02	1.451E-01	-2.407E-01	-4.303E-02	2.467E-01
13	-6.613E-03	1.811E-01	9.919E-01	-6.300E-02	3.881E-01
14	-6.139E-02	1.048E-01	9.803E-02	-1.614E-01	5.020E-01
15	-4.918E-01	-4.068E-01	3.353E-02	5.224E-01	3.890E-01
16	-2.201E-01	1.290E-01	-1.195E-01	4.349E-01	4.735E-02
17	2.285E-01	-8.434E-01	-8.093E-01	3.916E-01	6.467E-01

Table A3.2: Values of the weight matrix W_{ij}^2 between A_1, A_2 and A_3, A_4 with

$$P_g L_{c,ij} = 30 \text{ kPa-m (continued)}$$

	w^3	b^1	b^2
i = 1	3.964E-01	-3.856E+00	1.551E+00
2	-3.789E-01	-2.535E+00	-1.351E+00
3	6.746E-01	2.491E+00	9.956E-01
4	8.432E-01	1.836E+00	-8.396E-01
5	6.054E-01	-2.047E+00	-9.953E-01
6	-5.741E-02	1.824E+00	-4.628E-01
7	1.289E-01	-1.449E+00	6.435E-01
8	4.152E-01	-9.395E-01	2.254E-02
9	-1.861E+00	5.816E-01	5.092E-02
10	1.460E-01	3.267E-02	1.004E+00
11	-1.311E-01	-1.120E+00	4.023E-01
12	1.350E+00	6.381E-01	-8.124E-02
13	1.874E-01	1.067E+00	9.003E-01
14	-7.362E-01	1.009E+00	1.157E+00
15	-1.720E-01	1.280E+00	-7.032E-01
16	2.011E-01	1.827E+00	1.241E+00
17	1.275E-01	-2.509E+00	-1.316E+00
18		-2.197E+00	
19		3.087E+00	
20		3.448E+00	

Table A3.3: Values of the vectors W^3, b^1, b^2 between A_1, A_2 and A_3, A_4 with $P_g L_{c,ij} = 30$ kPa-m.

	j = 1	2	3	4
i = 1	9.775E-01	1.723E+00	1.735E+00	1.965E+00
2	-8.236E-01	9.197E-01	-1.127E+00	-3.499E-01
3	-1.473E+00	-2.589E+00	-4.849E-01	4.930E-02
4	-1.574E+00	-9.982E-01	-1.877E+00	7.590E-01
5	3.675E+00	-1.170E+00	1.326E+00	-7.573E-01
6	1.377E+00	1.331E-02	-2.152E+00	6.337E-01
7	2.007E+00	6.641E-01	4.623E-02	-7.606E-01
8	-1.158E+00	1.222E+00	-1.809E+00	-5.839E-01
9	7.610E-01	-8.208E-01	-1.251E+00	-2.346E+00
10	-1.525E+00	-1.230E+00	4.720E-01	7.016E-01
11	-8.461E-01	-1.099E+00	-1.332E+00	-4.496E-01
12	4.506E-01	4.627E-01	4.253E-01	-1.005E-01
13	-5.058E-01	-6.193E-01	1.463E+00	1.809E-01
14	1.967E+00	-1.123E+00	-6.572E-01	-3.045E+00
15	6.485E-01	-3.977E-01	1.896E+00	-1.835E-01
16	-1.585E-01	-1.085E+00	2.091E+00	9.503E-01
17	1.950E+00	3.624E-01	-6.669E-01	7.977E-01
18	-9.514E-01	8.402E-01	1.281E+00	-3.569E+00
19	9.707E-01	-9.418E-01	-2.471E+00	-1.228E+00

Table A4.1: Values of the weight matrix W_{ij}^1 between A_1 , A_2 and A_5 , A_6 with

$$P_g L_{c,ij} = 10 \text{ kPa}\cdot\text{m}.$$

	j = 1	2	3	4	5
i = 1	-1.487E-01	4.833E-02	1.165E-01	-1.166E+00	1.392E+00
2	-3.209E-01	-4.548E-01	-6.917E-01	-1.680E-01	4.369E-01
3	3.058E-01	-6.447E-02	7.992E-02	2.449E-01	9.144E-01
4	4.822E-01	8.997E-01	2.002E-01	3.630E-01	-2.081E-01
5	7.526E-01	-3.909E-01	-8.526E-01	-6.739E-01	-1.112E-01
6	4.231E-01	-2.994E-01	3.360E-01	3.658E-01	-8.911E-02
7	3.019E-01	-5.805E-01	-4.790E-03	7.865E-01	1.987E-01
8	7.619E-01	-4.891E-01	3.755E-02	-2.392E-01	4.084E-01
9	-3.529E-01	2.454E-01	-1.655E+00	-1.126E+00	1.057E+00
10	-1.832E-01	1.865E-01	-1.204E+00	1.087E+00	-1.336E+00
11	-4.960E-01	9.684E-02	-9.948E-01	1.986E-01	8.206E-02
12	-3.397E-01	-1.282E+00	-2.073E-01	3.413E-01	1.891E-01
13	-1.044E+00	-9.285E-01	-6.512E-01	-9.251E-01	-2.164E-01
14	1.490E-01	2.407E-01	-1.738E+00	-6.305E-01	6.557E-01
15	-5.406E-01	4.539E-01	6.541E-01	-1.317E+00	1.240E+00
16	-8.274E-01	-4.481E-01	-9.825E-01	-3.405E-01	-3.692E-01

Table A4.2: Values of the weight matrix W_{ij}^2 between A_1, A_2 and A_5, A_6 with

$$P_g L_{c,ij} = 10 \text{ kPa}\cdot\text{m}.$$

	j = 6	7	8	9	10
i = 1	2.052E-01	-3.271E-01	2.814E-02	-1.341E-01	2.440E-01
2	5.094E-01	2.756E-01	1.455E-01	3.965E-01	-2.171E-02
3	2.026E-01	5.263E-03	4.306E-01	1.020E+00	8.441E-01
4	2.489E-01	-3.956E-01	4.113E-01	-4.399E-01	6.776E-01
5	1.950E-01	-1.284E-01	1.281E-01	6.459E-01	8.835E-03
6	1.021E-01	3.592E-01	5.650E-04	3.567E-01	1.275E-01
7	3.715E-01	3.232E-01	2.107E-01	1.620E-01	-3.192E-01
8	1.106E+00	9.501E-01	1.938E-01	1.617E-01	-2.529E-01
9	3.383E-01	-3.587E-01	2.376E-01	-1.969E-01	-7.290E-01
10	-3.451E-01	2.039E-01	8.672E-02	1.117E-02	-2.600E-01
11	-3.075E-01	6.932E-02	-7.524E-02	-1.249E+00	-2.197E-01
12	3.823E-01	3.849E-01	5.732E-01	2.857E-02	-9.642E-01
13	-4.737E-01	1.620E-01	3.336E-01	-6.997E-01	-1.617E-01
14	2.781E-01	8.923E-01	3.808E-01	-6.537E-02	-7.187E-01
15	5.407E-01	8.249E-02	5.945E-02	-4.661E-01	-4.661E-01
16	2.855E-01	-2.372E-01	1.162E-01	1.511E-01	-3.709E-01

Table A4.2: Values of the weight matrix W_{ij}^2 between A_1, A_2 and A_5, A_6 with

$$P_g L_{c,ij} = 10 \text{ kPa-m (continued)}$$

	j = 11	12	13	14	15
i = 1	-8.447E-02	-1.083E+00	-2.672E-01	2.581E-02	-4.405E-01
2	-2.906E-01	-8.836E-01	-7.891E-02	4.395E-01	-3.551E-01
3	2.008E-01	-1.237E+00	5.094E-01	-1.619E-01	-1.080E+00
4	3.925E-01	-1.626E-01	6.187E-01	1.889E-01	-3.652E-01
5	2.395E-01	-3.142E-01	-1.623E-04	1.292E-01	-2.188E-01
6	2.286E-02	-8.435E-01	1.345E-01	5.424E-05	-3.189E-02
7	1.430E-02	1.195E-02	-1.046E-01	8.170E-01	7.025E-01
8	2.081E-01	-8.453E-01	1.168E-01	1.321E+00	9.942E-01
9	4.090E-01	-3.490E-02	5.775E-01	-2.200E-02	-2.427E-01
10	2.521E-01	1.116E+00	3.642E-01	-1.400E-01	2.532E-01
11	1.649E-01	-1.947E-02	3.091E-01	4.023E-01	2.430E-01
12	-3.338E-01	-6.684E-01	3.208E-01	1.656E+00	3.302E-01
13	2.665E-01	-5.131E-02	-1.358E-01	8.912E-02	-5.454E-01
14	1.831E-01	1.951E-01	3.257E-01	9.078E-01	4.257E-01
15	1.730E-01	-4.878E-01	5.292E-01	4.120E-01	-6.194E-01
16	3.678E-01	-5.415E-01	-2.584E-01	3.925E-01	7.941E-01

Table A4.2: Values of the weight matrix W_{ij}^2 between A_1, A_2 and A_5, A_6 with

$$P_g L_{c,ij} = 10 \text{ kPa-m (continued)}$$

	j = 16	17	18	19
i = 1	-1.749E-01	-1.210E-01	1.493E-01	-1.118E-01
2	-9.991E-02	-3.681E-01	2.268E-01	1.932E-01
3	8.763E-01	5.634E-01	-9.764E-01	-2.130E-01
4	-7.226E-02	1.824E-01	8.479E-02	-1.298E-01
5	6.944E-01	-3.183E-01	-1.009E+00	6.423E-01
6	-1.225E-01	-1.190E-01	-8.507E-01	8.867E-02
7	-5.176E-01	-2.799E-01	9.809E-01	9.948E-01
8	1.365E+00	-1.063E+00	1.177E+00	1.632E-01
9	9.946E-01	-3.787E-01	1.510E+00	9.882E-01
10	4.798E-01	1.572E-01	5.353E-02	-1.533E-01
11	-8.643E-01	6.762E-01	2.058E-01	2.156E-01
12	-5.991E-01	-3.433E-01	1.677E+00	2.689E-01
13	-4.740E-01	2.108E-01	-9.696E-01	-2.679E-01
14	8.981E-01	-1.303E+00	1.688E+00	-7.264E-02
15	2.491E-01	-6.748E-01	1.401E+00	1.655E+00
16	2.876E-01	-7.420E-02	7.740E-01	1.893E-01

Table A4.2: Values of the weight matrix W_{ij}^2 between A_1, A_2 and A_5, A_6 with

$$P_g L_{c,ij} = 10 \text{ kPa-m (continued).}$$

	w^3	b^1	b^2
i = 1	1.039E+00	-3.409E+00	1.415E+00
2	2.944E-01	1.731E+00	1.310E+00
3	1.720E-01	3.887E+00	1.342E+00
4	-2.009E-01	2.571E+00	-1.177E+00
5	-8.093E-01	-2.051E+00	-6.788E-01
6	1.257E+00	-1.568E+00	-1.506E+00
7	-1.272E+00	-1.024E+00	-1.264E+00
8	2.858E-01	2.887E-01	-1.072E+00
9	2.591E+00	-4.054E-01	3.074E-01
10	1.068E+00	7.918E-02	-3.667E-01
11	2.866E-01	1.716E-01	-6.430E-01
12	6.857E-01	-4.810E-01	-5.701E-01
13	-3.179E-01	-9.430E-01	-2.136E-01
14	-1.541E+00	1.713E+00	1.698E-01
15	-1.639E+00	1.760E+00	-2.068E+00
16	4.143E-01	2.744E+00	-1.381E+00
17		9.527E-01	
18		-4.855E+00	
19		3.184E+00	

Table A4.3: Values of the vectors W^3, b^1, b^2 between A_1, A_2 and A_5, A_6 with $P_g L_{c,ij} = 10$ kPa-m.

	j = 1	2	3	4
i = 1	1.401E+00	1.520E-01	-2.961E+00	-3.353E-01
2	8.195E-03	-1.261E+00	-1.239E+00	-1.109E+00
3	3.710E+00	2.064E-01	4.426E-01	-1.375E-01
4	1.102E+00	2.738E+00	1.267E+00	-1.071E+00
5	-1.276E+00	3.190E-01	3.033E-01	3.511E+00
6	-6.149E-01	-4.110E-01	-1.469E+00	2.100E+00
7	-2.468E+00	-1.059E+00	-2.588E-01	-1.825E+00
8	-1.057E+00	-9.698E-01	2.428E+00	-1.394E+00
9	1.055E+00	-1.599E+00	1.839E+00	-1.930E+00
10	1.345E-01	5.425E-01	3.592E-01	-1.687E-01
11	-1.605E+00	1.662E+00	-1.946E+00	7.307E-01
12	-1.427E+00	4.276E-01	1.328E+00	9.809E-01
13	4.355E-01	-1.554E-01	-2.669E+00	-2.841E-01
14	-2.160E+00	4.477E-01	4.358E-01	1.456E+00
15	-2.341E+00	4.616E-01	-4.624E-02	-9.393E-02
16	-1.665E+00	-8.533E-01	6.285E-01	7.071E-01
17	7.113E-02	1.953E+00	4.629E-02	8.791E-01
18	-1.396E+00	3.119E-01	-1.817E+00	2.641E-01
19	-1.604E-01	1.077E+00	-6.200E-01	1.890E-02

Table A5.1: Values of the weight matrix W_{ij}^1 between A_1 , A_2 and A_5 , A_6 with
 $P_g L_{c,ij} = 30$ kPa-m.

	j = 1	2	3	4	5
i = 1	-3.068E-01	1.277E-01	-7.173E-02	-5.885E-01	7.843E-02
2	-9.397E-01	-2.637E-01	7.370E-01	6.392E-01	-8.143E-02
3	-3.957E-02	1.003E-01	7.409E-01	-3.270E-01	1.984E-01
4	-8.545E-01	2.148E-01	9.731E-01	1.586E-01	1.463E-01
5	-4.444E-01	-1.745E-01	-5.463E-01	-6.074E-01	-5.370E-02
6	6.554E-01	2.309E-01	-2.194E-01	-8.170E-01	-2.840E-02
7	-3.342E-01	5.758E-01	8.653E-01	9.000E-01	-5.507E-02
8	4.901E-01	3.578E-01	2.810E-01	-4.596E-01	1.535E-01
9	-3.039E-01	1.474E-01	3.943E-01	-3.315E-01	4.675E-02
10	-8.499E-01	-2.453E-01	-7.267E-01	-1.271E+00	-8.821E-02
11	5.137E-01	4.569E-01	-2.869E-01	-8.582E-02	6.173E-02
12	7.220E-01	1.650E-01	1.471E-01	2.825E-01	1.306E-02
13	5.162E-01	-1.195E-01	3.807E-02	1.860E-01	5.900E-01
14	-5.958E-01	7.472E-01	-7.020E-01	3.974E-01	-2.647E-01
15	-2.866E-01	9.830E-01	-1.257E+00	-1.004E+00	-1.521E-01
16	-2.132E+00	4.015E-02	3.201E+00	4.764E+00	1.691E+00

Table A5.2: Values of the weight matrix W_{ij}^2 between A_1 , A_2 and A_5 , A_6 with

$$P_g L_{c,ij} = 30 \text{ kPa-m.}$$

	j = 6	7	8	9	10
i = 1	-6.505E-01	-3.502E-01	6.780E-01	5.008E-01	-8.224E-02
2	-2.829E-01	3.015E-01	-3.423E-01	6.021E-02	-7.596E-02
3	-3.828E-01	-5.886E-02	-1.453E-02	3.510E-01	-9.322E-02
4	3.238E-01	3.096E-01	-3.762E-01	3.812E-01	1.456E-02
5	-5.079E-01	-2.442E-01	3.065E-01	4.657E-01	2.916E-01
6	-2.789E-01	5.497E-02	-2.823E-02	3.128E-01	4.623E-02
7	-1.031E+00	2.281E-01	-9.129E-01	-3.975E-02	-1.526E-01
8	6.134E-01	-1.080E-01	-8.853E-02	-1.111E-01	1.337E+00
9	-4.781E-01	-1.961E-02	2.702E-01	4.187E-01	5.665E-02
10	-3.419E-01	-2.805E-01	1.680E-01	2.257E-01	1.104E+00
11	-1.442E-01	3.372E-02	8.242E-02	2.976E-01	-8.514E-01
12	4.575E-01	2.575E-01	-2.073E-01	-4.736E-01	-7.570E-01
13	1.643E-01	-7.515E-02	8.249E-01	2.473E-01	-3.412E-01
14	-1.552E-01	7.277E-01	8.420E-01	2.369E-02	-5.573E-01
15	-1.149E+00	1.976E-02	-2.460E-01	4.669E-01	5.159E-02
16	-2.983E+00	2.176E+00	-4.344E+00	1.632E+00	3.223E-01

Table A5.2: Values of the weight matrix W_{ij}^2 between A_1, A_2 and A_5, A_6 with

$$P_g L_{c,ij} = 30 \text{ kPa-m (continued).}$$

	j = 11	12	13	14	15
i = 1	-1.724E-01	5.957E-02	7.299E-01	5.041E-01	-5.451E-01
2	1.006E-01	4.457E-01	-2.759E-01	7.513E-03	-6.420E-01
3	-2.259E-01	5.514E-01	2.035E-01	-2.821E-01	3.638E-02
4	2.539E-01	3.408E-01	-4.593E-01	1.443E-04	-4.863E-01
5	-1.018E-01	3.100E-01	1.945E-01	3.266E-03	6.121E-01
6	2.504E-01	-4.536E-01	1.568E-01	-1.488E-01	-1.172E-03
7	-6.198E-01	4.123E-01	-6.203E-02	4.161E-01	-3.475E-02
8	3.131E-01	-5.400E-01	8.905E-02	3.627E-01	-3.003E-01
9	-6.267E-03	8.832E-02	1.545E-02	2.295E-01	4.482E-01
10	-1.167E-01	-3.620E-01	-9.733E-02	-3.889E-02	1.580E-01
11	1.910E-01	-4.589E-01	5.853E-02	4.130E-01	8.515E-02
12	2.524E-01	-6.713E-02	-1.670E-01	-2.847E-01	-4.506E-01
13	4.093E-02	-1.817E-01	-6.088E-02	-3.279E-01	6.132E-01
14	-6.619E-01	1.131E-01	1.941E-01	-2.582E-01	2.328E-01
15	2.595E-01	-5.804E-01	-9.622E-02	-9.806E-02	-3.666E-01
16	-2.430E+00	9.393E-01	1.409E+00	1.160E+00	1.186E+00

Table A5.2: Values of the weight matrix W_{ij}^2 between A_1, A_2 and A_5, A_6 with

$$P_g L_{c,ij} = 30 \text{ kPa-m (continued).}$$

	j = 16	17	18	19
i = 1	6.703E-01	2.954E-02	1.516E-03	5.438E-01
2	-2.837E-01	-1.316E-01	6.660E-02	-6.032E-01
3	-2.879E-01	-5.446E-02	-5.667E-01	-3.179E-01
4	-3.806E-02	3.707E-01	-5.495E-01	-5.007E-01
5	-1.713E-01	-3.654E-02	-7.704E-01	-2.541E-02
6	-1.667E-01	-3.126E-01	-6.189E-01	-2.314E-01
7	-4.049E-01	-6.169E-01	4.924E-01	1.045E+00
8	5.464E-01	3.127E-01	-4.609E-01	-2.485E-01
9	-2.858E-01	2.861E-01	-1.924E-01	1.057E+00
10	8.596E-02	-2.026E-01	3.083E-01	1.766E-01
11	-1.118E-01	-2.161E-01	2.382E-03	3.152E-02
12	2.292E-01	7.188E-02	-4.191E-01	-8.006E-01
13	-5.574E-01	-2.920E-01	6.652E-01	3.319E-01
14	2.505E-01	-3.445E-01	8.368E-02	2.156E-01
15	2.976E-02	-5.119E-01	2.524E-01	2.630E-01
16	-7.116E-01	-3.825E-01	-8.537E-01	-6.600E-02

Table A5.2: Values of the weight matrix W_{ij}^2 between A_1, A_2 and A_5, A_6 with

$$P_g L_{c,ij} = 30 \text{ kPa-m (continued).}$$

	w^3	b^1	b^2
i = 1	-7.163E-01	-3.145E+00	1.936E+00
2	-4.656E-01	-2.750E+00	1.652E+00
3	2.371E-01	-3.095E+00	-1.190E+00
4	5.034E-01	-3.610E+00	1.136E+00
5	5.366E-01	2.002E+00	1.176E+00
6	-2.472E-01	2.973E+00	-6.081E-01
7	-4.615E-01	1.354E+00	8.374E-02
8	-2.952E-01	8.376E-01	1.608E-02
9	-3.259E-01	-1.001E+00	-1.313E+00
10	3.346E-01	-3.573E-01	-1.114E+00
11	5.709E-01	-4.068E-01	8.209E-01
12	3.275E-01	-4.141E-01	-4.698E-01
13	-1.059E-01	1.359E+00	8.748E-01
14	-2.716E-02	-8.274E-01	-8.814E-01
15	-1.759E-01	-2.004E+00	1.226E+00
16	1.251E+00	-1.567E+00	-1.137E+00
17		2.679E+00	
18		-2.944E+00	
19		1.124E+00	

Table A5.3: Values of the vectors W^3, b^1, b^2 between A_1, A_2 and A_5, A_6 with $P_g L_{c,ij} = 30$ kPa-m.

	j=1	2	3	4
i= 1	2.555E+00	3.100E+00	2.879E+00	-4.145E+00
2	1.783E+00	5.760E-01	-3.839E+00	2.016E+00
3	-1.671E+00	-2.162E+00	8.539E-02	-2.122E-01
4	1.673E+00	1.032E+00	-2.591E+00	1.230E+00
5	7.472E-01	1.777E+00	8.826E-01	-1.402E+00
6	-1.315E+00	4.523E-01	7.382E-01	7.468E-02
7	-3.773E-01	1.141E+00	-1.718E+00	-6.627E-02
8	-2.233E-01	1.145E+00	-2.339E-01	1.838E+00
9	8.923E-01	-6.096E-01	3.146E-01	1.458E+00
10	1.479E+00	2.908E-01	4.026E-01	-3.689E-01
11	-1.168E+00	-6.800E-01	1.524E+00	-1.678E+00
12	5.771E-01	5.406E-01	7.073E-01	-3.320E-01
13	1.650E+00	-1.843E+00	-1.005E+00	-1.265E+00
14	2.643E-01	-1.386E+00	6.361E-01	7.826E-01
15	5.894E-01	-1.511E+00	1.195E+00	-1.775E+00
16	-7.508E-01	-5.175E-01	-4.069E-01	5.719E-01
17	1.747E-01	2.094E+00	-2.054E+00	-8.793E-01
18	6.709E-01	6.621E-01	-3.982E-01	1.139E+00
19	9.641E-02	-5.272E-01	2.720E+00	-9.847E-02

Table A6.1: Values of the weight matrix W_{ij}^1 between A_3 , A_4 and A_5 , A_6 with
 $P_g L_{c,ij} = 10$ kPa-m.

	j= 1	2	3	4	5	6
i=1	-1.007E+00	1.921E-01	3.558E-01	1.689E-01	8.546E-01	4.283E-01
2	5.269E-01	-1.672E-01	-4.971E-02	5.799E-01	7.185E-02	7.847E-01
3	1.884E-01	7.348E-01	-4.374E-01	-8.901E-01	-5.116E-01	-4.380E-01
4	-3.584E+00	-1.514E-01	-2.027E+00	-1.565E+00	5.902E-01	7.226E-01
5	-6.494E-01	4.534E-01	-5.848E-01	-1.581E-01	-8.603E-01	1.048E+00
6	-4.628E-01	-5.365E-02	-5.363E-01	2.227E-01	-1.910E-01	-3.141E-01
7	-2.370E-01	8.638E-02	-3.386E-02	6.185E-01	-2.401E-02	3.802E-01
8	4.770E-01	1.567E-01	5.332E-03	-1.579E-01	-2.887E-01	5.390E-02
9	7.042E-01	-6.710E-02	2.659E-01	-5.850E-02	-5.671E-01	-6.649E-02
10	5.387E-01	-1.102E-01	1.786E-01	-4.521E-01	3.449E-01	3.630E-01
11	-6.585E-01	-2.332E-01	-2.020E+00	-1.466E+00	7.862E-01	8.725E-01
12	-1.232E+00	1.319E-01	7.790E-02	-1.095E-01	5.587E-02	2.897E-01
13	5.870E-01	-2.836E+00	-2.683E+00	3.240E+00	1.872E+00	-2.779E-01
14	-1.264E-01	2.407E-02	4.128E-01	1.009E-01	1.217E+00	-1.704E-01
15	-1.070E+00	6.154E-02	-7.754E-01	-4.166E-02	2.864E-01	-2.839E-01
16	-1.834E+00	1.636E-01	1.460E-01	7.540E-02	2.139E-01	2.093E-01

Table A6.2: Values of the weight matrix W_{ij}^2 between A_3 , A_4 and A_5 , A_6 with

$$P_g L_{c,ij} = 10 \text{ kPa-m.}$$

	j = 7	8	9	10	11	12
i=1	5.838E-01	4.241E-01	1.779E-02	-1.465E-02	-1.900E-02	3.930E-01
2	-1.064E-01	-3.038E-01	2.184E-02	6.870E-01	-4.851E-01	-5.237E-01
3	-2.126E+00	7.326E-02	6.616E-01	-9.726E-01	-2.009E-01	9.317E-02
4	-3.089E+00	3.305E-01	-6.137E-02	-6.687E-01	-2.013E+00	8.805E-01
5	3.971E-01	5.676E-02	2.101E-01	7.605E-01	-2.435E-01	-4.538E-01
6	2.930E-01	6.270E-02	2.405E-02	-5.182E-01	1.023E-02	8.531E-01
7	-2.265E-01	-4.794E-01	-7.577E-01	-7.396E-01	-2.467E-01	-3.729E-01
8	5.561E-01	-4.539E-01	-6.304E-01	-6.654E-01	-6.195E-01	1.283E+00
9	-5.256E-01	8.806E-02	2.822E-01	4.621E-02	1.388E-01	-1.020E+00
10	-6.432E-01	1.628E-01	-8.839E-01	-6.019E-01	1.659E-02	6.666E-01
11	-1.276E+00	2.346E-01	-2.137E-01	-4.755E-01	-1.858E+00	9.284E-01
12	8.205E-02	-1.811E-01	-1.787E-01	4.195E-01	5.138E-02	-2.117E-01
13	1.721E-01	1.114E+00	8.743E-02	6.941E-01	1.687E-01	-3.949E-01
14	-3.408E-01	-1.677E-01	-8.300E-01	-2.803E-01	-5.791E-01	1.498E-01
15	-5.201E-01	-1.653E-01	-5.953E-01	-4.093E-01	7.042E-02	-7.481E-01
16	-1.149E-01	-4.462E-01	-4.019E-01	-5.057E-01	-1.565E-01	-2.233E-01

Table A6.2: Values of the weight matrix W_{ij}^2 between A_3 , A_4 and A_5 , A_6 with

$$P_g L_{c,ij} = 10 \text{ kPa-m (continued)}$$

	j = 13	14	15	16	17	18	19
i= 1	-3.116E-01	3.774E-01	-6.515E-01	-3.503E-01	6.260E-01	8.215E-02	3.328E-02
2	1.356E-01	5.531E-01	1.550E-02	-5.955E-01	-3.690E-01	4.050E-01	-8.478E-01
3	-1.685E-01	-6.313E-01	-1.028E+00	-8.064E-01	4.750E-01	-6.747E-01	1.085E-01
4	1.679E+00	-3.531E-02	-2.718E-01	-5.650E-01	-1.342E+00	7.217E-01	1.052E+00
5	-8.328E-01	1.164E+00	-4.561E-01	-7.811E-01	3.482E-02	6.725E-01	-2.129E-01
6	2.763E-01	6.613E-02	2.424E-01	-1.292E-01	1.553E-01	5.565E-01	3.194E-01
7	1.061E-01	-5.228E-01	5.836E-01	3.001E-01	4.731E-01	1.166E+00	5.335E-02
8	3.619E-01	1.272E-01	1.648E-01	-4.065E-01	-2.737E-01	9.904E-02	-1.618E-01
9	-1.371E-01	-1.863E-01	-7.518E-02	-9.482E-02	2.696E-02	-7.887E-02	1.219E-01
10	3.749E-01	-6.175E-01	-4.339E-01	-1.291E+00	1.087E+00	-3.053E-01	1.528E-01
11	1.613E+00	2.504E-01	-3.896E-01	-5.297E-01	-1.485E+00	9.882E-01	8.100E-01
12	-1.372E-01	-2.418E-01	5.779E-02	4.042E-01	4.012E-01	-1.852E-01	-2.791E-01
13	-7.878E-01	1.376E+00	9.031E-01	4.544E-01	-2.074E+00	-1.327E+00	2.321E-01
14	-6.674E-02	1.115E+00	9.430E-02	-5.111E-01	-8.330E-01	-7.940E-02	-1.108E+00
15	-4.719E-01	2.209E-01	4.791E-01	-4.908E-01	-9.727E-02	8.106E-01	3.207E-01
16	5.006E-02	-5.683E-01	3.407E-01	1.475E-03	4.357E-01	6.661E-01	-1.834E-01

Table A6.2: Values of the weight matrix W_{ij}^2 between A_3, A_4 and A_5, A_6 with $P_g L_{c,ij} = 10$ kPa-m (continued)

	w^3	b^1	b^2
i = 1	-2.675E-01	-7.898E+00	1.265E+00
2	-4.211E-01	-3.122E+00	1.444E+00
3	8.887E-01	2.928E+00	-6.445E-01
4	-1.424E+00	-2.357E+00	4.034E-01
5	2.498E-01	-3.018E+00	3.262E-01
6	8.339E-01	8.660E-01	-2.225E-01
7	4.159E-01	1.589E+00	-3.510E-01
8	3.326E-01	1.635E-01	-1.634E-01
9	1.246E+00	-2.379E-01	-1.660E-01
10	-7.788E-02	3.549E-01	-4.290E-01
11	1.430E+00	6.852E-03	1.601E+00
12	1.481E+00	-3.320E-01	-3.130E-01
13	1.201E+00	1.639E+00	-1.589E+00
14	3.698E-01	-2.841E-01	1.843E+00
15	-3.327E-01	1.370E+00	-1.199E+00
16	-1.029E+00	-6.228E-01	-1.592E+00
17		-3.337E+00	
18		1.963E+00	
19		2.290E+00	

Table A6.3: Values of the vectors W^3, b^1, b^2 between A_3, A_4 and A_5, A_6 with $P_g L_{c,ij} = 10$ kPa-m (continued)

	j = 1	2	3	4
i = 1	1.148E+00	-2.980E-01	-2.552E+00	-5.387E-01
2	-2.974E-01	-7.184E-01	-2.579E+00	2.612E-01
3	-4.109E-01	5.828E-01	-4.380E-01	-2.343E-01
4	3.164E+00	3.566E-01	-3.026E-01	1.408E+00
5	-1.022E+00	-1.917E+00	-1.569E+00	1.838E+00
6	1.461E+00	-2.032E+00	7.146E-01	-1.487E+00
7	1.622E+00	6.063E-02	2.561E+00	3.382E-01
8	-1.415E-01	-2.171E+00	1.119E+00	-1.563E+00
9	5.912E-01	-1.225E+00	1.047E+00	-3.503E+00
10	-2.040E+00	-9.767E-01	1.229E+00	4.693E-01
11	6.432E-01	6.715E-01	8.732E-01	-2.572E-02
12	2.663E+00	8.237E-01	3.390E-01	2.042E+00
13	1.059E+00	-7.115E-01	2.097E+00	8.724E-01
14	-2.095E+00	1.934E+00	-2.136E+00	-2.304E+00
15	-9.975E-01	-3.735E-01	1.737E-01	-6.435E-01
16	8.362E-01	-1.701E+00	-1.917E+00	5.752E-01
17	-1.031E+00	-2.207E-01	-3.116E-01	1.512E-01
18	-5.011E-02	4.620E-01	-2.159E+00	5.783E-01
19	2.395E-01	-2.309E-01	-5.472E-01	-3.594E+00

Table A7.1: Values of the weight matrix W_{ij}^1 between A_3 , A_4 and A_5 , A_6 with
 $P_g L_{c,ij} = 30$ kPa-m.

	j = 1	2	3	4	5
i = 1	-6.771E-01	-1.439E+00	-3.291E-01	4.809E-01	-1.722E+00
2	2.587E-01	6.440E-01	8.915E-01	-3.771E-01	-1.185E+00
3	3.690E-01	-6.572E-01	-4.746E-01	-3.949E-01	4.900E-01
4	5.401E-01	-4.729E-01	-5.316E-01	-2.950E-02	-6.486E-01
5	1.296E-01	5.702E-02	-3.244E-01	1.577E-01	4.507E-01
6	3.375E-01	-5.162E-01	-9.165E-01	3.484E-01	-7.853E-01
7	2.850E-01	2.112E-01	-6.389E-02	-6.969E-03	2.135E-01
8	3.677E-01	-5.317E-01	-8.760E-01	-4.325E-01	3.910E+00
9	-7.049E-02	2.167E-01	-2.533E-01	-3.920E-01	3.505E+00
10	-9.944E-02	-2.083E-01	4.307E-01	4.594E-02	-5.899E-01
11	6.637E-02	4.669E-03	-7.001E-02	-1.133E-01	3.866E-01
12	-4.884E-01	8.022E-01	-1.131E+00	-1.478E+00	2.534E+00
13	9.234E-02	6.489E-03	-2.408E-01	1.633E-01	1.011E+00
14	-1.269E+00	-8.914E-02	-2.232E-02	8.401E-01	-3.214E+00
15	5.923E-01	4.317E-01	1.330E+00	-2.531E-01	-8.143E-01

Table A7.2: Values of the weight matrix W_{ij}^2 between A_3, A_4 and A_5, A_6 with
 $P_g L_{c,ij} = 30$ kPa-m.

	j = 6	7	8	9	10
i = 1	-3.780E-01	-7.346E-01	1.244E-01	-2.934E-01	-1.214E-01
2	2.507E-01	-1.717E+00	1.521E+00	-1.305E+00	9.748E-01
3	1.372E-01	-9.888E-01	2.314E-01	1.768E-01	5.088E-01
4	1.415E-02	-1.012E-02	3.316E-01	1.528E-01	-4.981E-01
5	3.864E-01	2.338E-01	-9.601E-02	-2.535E-01	3.325E-02
6	-8.887E-01	2.590E-01	6.000E-01	-2.381E-01	-7.818E-01
7	3.444E-01	-4.115E-01	-9.362E-02	-2.620E-01	1.075E-01
8	3.447E-02	-1.496E+00	3.336E-01	1.181E-01	6.192E-01
9	4.179E-01	-1.136E+00	7.008E-02	1.180E-01	7.280E-01
10	-2.598E-01	2.886E-01	7.857E-02	1.525E-01	8.727E-02
11	1.749E-02	-2.512E-01	4.877E-02	5.789E-02	8.808E-03
12	2.605E+00	-2.801E-01	1.649E-01	5.197E-01	-2.228E-01
13	5.272E-01	1.852E-01	-1.358E-01	-2.487E-01	-6.233E-02
14	1.789E-02	1.347E+00	-3.607E-01	4.767E-01	-4.757E-02
15	-1.659E-01	-3.157E-01	9.608E-02	9.955E-02	2.689E-01

Table A7.2: Values of the weight matrix W_{ij}^2 between A_3 , A_4 and A_5 , A_6 with $P_g L_{c,ij} = 30$ kPa-m (continued) .

	j = 11	12	13	14	15
i = 1	1.556E+00	-4.003E-01	-6.325E-01	4.210E-02	1.442E+00
2	8.370E-01	-1.018E+00	3.713E-01	-4.837E-01	-6.585E-01
3	-9.264E-01	-4.067E-01	1.080E+00	-1.639E-01	-2.523E-01
4	9.080E-01	2.431E-01	-5.515E-01	-2.522E-01	-1.964E-01
5	4.558E-01	1.810E-02	-5.786E-01	6.981E-03	-7.756E-02
6	8.530E-01	5.810E-01	-2.412E-01	1.110E+00	1.332E-01
7	-2.111E-01	1.508E-01	1.602E+00	-1.977E-01	2.760E-01
8	-1.172E-01	-5.743E-01	1.116E+00	-2.776E-01	3.123E-01
9	2.176E-01	-6.606E-01	6.740E-01	-8.313E-01	6.778E-01
10	4.675E-01	-1.006E-01	-1.269E+00	1.944E-01	-2.389E-01
11	-8.755E-02	2.573E-02	1.708E-01	-9.715E-03	1.915E-01
12	-5.017E-02	-1.404E+00	-8.054E-01	-9.435E-01	-5.902E-01
13	5.409E-01	5.990E-02	-3.926E-01	9.608E-03	-1.197E-01
14	1.680E+00	8.268E-01	-2.008E+00	-1.740E-01	9.057E-01
15	1.988E-01	-5.397E-02	1.446E-01	-5.207E-02	5.715E-02

Table A7.2: Values of the weight matrix W_{ij}^2 between A_3, A_4 and A_5, A_6 with $P_g L_{c,ij} = 30$ kPa-m (continued) .

	j = 16	17	18	19
i = 1	6.763E-01	-1.223E+00	-2.504E-01	7.778E-02
2	1.512E+00	-3.990E-01	-9.299E-01	-3.540E-01
3	-1.030E+00	-6.964E-02	3.891E-01	-5.288E-01
4	1.367E+00	1.558E+00	6.816E-01	2.092E-01
5	-3.771E-01	1.178E+00	-4.535E-02	-2.998E-01
6	6.684E-01	1.211E-01	-5.278E-01	-7.006E-02
7	-1.111E-01	-8.812E-01	-7.968E-01	-8.561E-01
8	-4.272E-01	2.277E-01	5.987E-01	-4.005E-01
9	3.520E-01	5.238E-01	6.743E-01	-9.204E-02
10	1.549E-01	4.639E-01	5.603E-01	6.095E-01
11	2.361E-01	-3.919E-01	1.216E-01	-6.470E-02
12	6.375E-01	-6.657E-01	4.840E-01	-1.993E+00
13	-4.213E-01	1.304E+00	1.483E-01	-3.868E-01
14	8.127E-01	1.718E-01	-1.159E+00	7.085E-01
15	-3.793E-02	-1.260E+00	3.710E-01	-2.412E-01

Table A7.2: Values of the weight matrix W_{ij}^2 between A_3, A_4 and A_5, A_6 with $P_g L_{c,ij} = 30$ kPa-m (continued) .

	w^3	b^1	b^2
i = 1	-1.335E+00	-2.845E+00	-2.645E+00
2	1.655E+00	-1.266E+00	1.861E+00
3	-1.493E+00	8.595E-01	1.924E+00
4	-1.580E+00	-3.443E+00	-8.417E-01
5	1.144E+00	4.393E+00	3.834E-01
6	-1.118E+00	-7.829E-01	-1.506E+00
7	-5.346E-01	-9.704E-01	-5.027E-02
8	2.746E+00	4.178E-01	-1.832E-01
9	-2.486E+00	9.419E-02	3.807E-01
10	-6.876E-01	1.791E-01	2.229E-01
11	1.459E+00	-6.803E-01	-1.453E+00
12	-1.830E+00	3.219E-01	8.827E-01
13	-9.454E-01	-1.260E+00	2.028E-01
14	1.548E+00	-1.476E+00	-1.437E+00
15	-3.559E-01	-1.161E+00	1.014E+00
16		2.352E+00	
17		-8.462E-01	
18		-2.774E+00	
19		-3.457E+00	

Table A7.3: Values of the vectors W^3, b^1, b^2 between A_3, A_4 and A_5, A_6 with $P_g L_{c,ij} = 10$ kPa-m (continued)

List of Figures (Appendix A)

Figure A1: Structure of a three-layer neural network used in the correlation of the excess absorptance, $\Delta\alpha(T_w, T_g, P_{CO_2}L, P_{H_2O}L, f_vL)$ A-44

Three Layers of Neurons

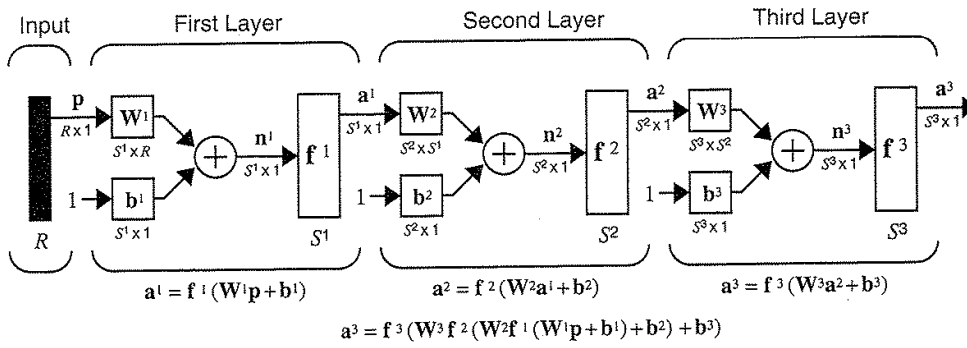


Figure A1: Structure of a three-layer neural network used in the correlation of the excess absorptance, $\Delta\alpha(T_w, T_g, P_{CO_2} L, P_{H_2O} L, f_v L)$

Appendix B

Model Description for BERHT

B.1 Solar Gains

In this section, the models for external and internal heat gain will be presented.

B.1.1 Solar Geometry

To obtain the shortwave solar radiation incident on an arbitrary surface, solar time and solar declination will first have to be determined.

The position of the sun is a function of location of a specific site, time of a day, and day of the year. In order to evaluate the solar position, the apparent solar time, *AST*, must be determined. *AST* is a function of local standard time, equation of time, local standard meridian, and longitude of the site. For a more detailed discussion, see EPlus (2011), Kreider and Rabl (1994), and Rabl (1985).

Equation of time

The equation of time, *ET*, accounting for the Earth's orbital velocity variation throughout the year, is approximated by:

$$ET = 2.2918 \left(\begin{array}{l} 0.0075 + 0.1868 \cos(N_{day}) - 3.2077 \sin(N_{day}) \\ -1.4615 \cos(2N_{day}) - 4.089 \sin(2N_{day}) \end{array} \right) \quad (B.1)$$

with

$$N_{day} = (day - 1)(360 / 365) \quad (B.2)$$

where *day* is the day of the year from 1 to 365. The apparent solar time is then given by:

$$AST = LST + ET \pm \frac{4\{\text{min}\}}{1\{\text{deg}\}} \left(\left| \frac{15\{\text{deg}\}}{1\{\text{hour}\}} \cdot GMTD \right| - LON \right) \quad (B.3)$$

with the time being added for site to the east of Greenwich and subtracted for site to the west where

AST = solar time {min}

LST = local standard time {min}

ET = equation of time {min}

GMTD = time difference between local site and Greenwich Mean Time {hour}

LON = longitude of site {degree}

Hour angle and declination angle

The solar time is used to determine a quantity known as the hour angle, H_{angle} , which is the angular distance between the site location and the meridian. H_{angle} is defined as the difference between the apparent solar time and the solar noon, SN :

$$H_{angle} = \frac{1\{\text{deg}\}}{4\{\text{min}\}} \left| ST - 12\{\text{hour}\} \cdot \frac{60\{\text{min}\}}{1\{\text{hour}\}} \right| \quad (B.4)$$

where the hour angle is in unit of degree. The last required quantity for the determination of the solar position is the declination of sun, which is the angular distance to the site location measured from the equator. The value of sun declination varies throughout the year and is approximated by:

$$\delta_s = \left[\begin{array}{l} 0.3963723 - \\ 22.9132745 \cos(N_{day}) + 4.0254304 \sin(N_{day}) - \\ 0.3872050 \cos(2N_{day}) + 0.05196728 \sin(2N_{day}) - \\ 0.1545267 \cos(3N_{day}) + 0.08479777 \sin(3N_{day}) \end{array} \right] \{\text{deg}\} \quad (\text{B.5})$$

with N_{day} defined identically in Eqn. (B.2). Now, elevation angle and azimuth angle can be evaluated to obtain the angle of incidence for further calculation for the solar incidence.

Solar elevation angle and solar azimuth angle

As shown in Figure B.1, the solar elevation angle, β_s , and solar azimuth angle, ϕ_s , describe the position of the sun in respect to an arbitrary surface on the horizontal plane. The solar elevation angle is, varying from 0° to 90° , defined as the angular height of the sun in the sky measured from the plane and the relative azimuth angle is defined as the angular difference between the solar azimuth ϕ_s and the surface azimuth Ψ_s . Using the hour angle along with the local latitude, LAT , the elevation angle can be determined by the expression in (ASHRAE, 2009):

$$\beta_s = \sin^{-1} \left(\sin(\delta_s) \sin(LAT) + \cos(\delta_s) \cos(LAT) \cos(H_{angle}) \right) \{\text{deg}\} \quad (\text{B.6})$$

and the solar azimuth angle measured respect to the south:

$$\phi_s = \cos^{-1} \left(\frac{\cos(H_{angle}) \cos(\delta_s) \sin(LAT) - \sin(\delta_s) \cos(LAT)}{\sin(\beta_s)} \right) \{deg\} \quad (B.7)$$

such that $\varphi_s = \phi_s - \Psi_s$ where Ψ_s is defined as the displacement between the true south on the plane and the surface normal.

Solar angle of incidence

The angle of incidence, θ_s , for an arbitrary surface will be obtained (Sellers, 1965):

$$\theta_s = \cos^{-1} \left\{ \begin{array}{l} \cos(\Sigma) \left[\cos(\delta_s) \cos(H_{angle}) \cos(LAT) + \sin(\delta_s) \sin(LAT) \right] + \\ \sin(\Sigma) \sin(\varphi_s) \cos(\delta_s) \sin(H_{angle}) + \\ \sin(\Sigma) \cos(\varphi_s) \left[\cos(\delta_s) \cos(H_{angle}) \sin(LAT) - \sin(\delta_s) \cos(LAT) \right] \end{array} \right\} \{deg\} \quad (B.8)$$

where

Σ is surface tilted angle measured from the plane; values above 90° indicates surfaces facing to ground. The angle of incidence is the angle between the sun's rays irradiated on a surface and this quantity will be used while the shortwave solar radiation incident on an arbitrary surface is being determined.

B.1.2 Shortwave Solar Incidence

We will now present models for the shortwave solar incidence. The total shortwave solar radiation incident on an arbitrary surface is consisted of three components: 1) beam solar incidence, $q''_{s,beam}$, 2) sky diffuse solar incidence, $q''_{s,sky}$, and 3) ground reflected diffuse solar incidence, $q''_{s,gnd}$ (Eplus, 2011).

B.1.2a Beam Solar Incidence

The beam solar radiation, q''_{beam} , for surfaces normal to the sun in a clear day is approximated by the following correlation (ASHRAE, 2005):

$$q''_{beam} = A_s / \exp\left(\frac{B_s}{\sin(\beta_s)}\right) \{W/m^2\} \quad (B.9)$$

where

A_s = apparent solar irradiation

B_s = atmospheric extinction coefficient

β_s = elevation angle defined in Eqn. (B.6).

The average apparent solar irradiation and the atmospheric extinction coefficient for each month are listed in Table. B.1. To obtain the beam solar incidence, $q''_{s,beam}$, on an arbitrary surface, the Lambert's cosine law, which states that the irradiation received by a surface is equal to the intensity impinging on the projected surface area, is applied such that (Eplus, 2011):

$$q''_{s,beam} = q''_{beam} \cos(\theta_s) \quad (B.10)$$

where θ_s is the angle of incidence defined in Eqn. (B.8).

B.1.2b Sky Diffuse Solar Incidence

The diffuse sky radiation, q''_{sky} , is simply given by (ASHRAE, 2005):

$$q''_{sky} = C_s \cdot q''_{beam} \{ \text{W/m}^2 \} \quad (\text{B.11})$$

where C_s is the diffuse radiation factor (Table. B.1). In BERHT, the Perez's sky model (1990) is implemented for the determination of the diffuse solar incidence on an arbitrary surface. In this model, the diffuse solar incidence is characterized by three distributions (Figure B.2): 1) $R_{s,dome}$, isotropic dome that covers radiance from the entire sky hemisphere, 2) $R_{s,circumsolar}$, circumsolar brightening represented as a point source at the sun, and 3) $R_{s,horizon}$, horizon brightening represented as a line source at the horizon:

$$R_{s,dome} = (1 - G_{s,1}) \frac{(1 + \cos(\Sigma))}{2} \quad (\text{B.12})$$

$$R_{s,circumsolar} = G_{s,1} \frac{a_s}{b_s} \quad (\text{B.13})$$

$$R_{s,horizon} = G_{s,2} \sin(\Sigma) \quad (\text{B.14})$$

The proportion of these distributions is established by two quantities: circumsolar brightening coefficients, $G_{s,1}$, and horizon brightening coefficients, $G_{s,2}$. To obtain $G_{s,1}$ and $G_{s,2}$, sky brightness, which depends on relative air mass, and sky clearness are needed to be computed. The relative air mass is (Perez, 1999):

$$m_{s,air} = \frac{1}{\cos(\beta_s) + 0.15 * (93.9 - \beta_s)^{-1.253}} \quad (\text{B.15})$$

The sky brightness factor Δ_s , from 0 to 1, is (Perez, 1990):

$$\Delta_s = q''_{sky} m_{s,air} / I_E \quad (\text{B.16})$$

where

I_E = extraterrestrial irradiance (Table. B.1)

The sky clearness factor, ε_s , is (Perez, 1990):

$$\varepsilon_s = \frac{(q''_{sky} + q''_{beam}) / q''_{sky} + 1.041\beta_s}{1 + 1.041\beta_s^3} \quad (\text{B.17})$$

with sky clearness factor of 1 indicates an overcast sky and sky clearness factor of 8 indicates a clear sky. The circumsolar brightening coefficients and horizon brightening coefficients can be computed as:

$$G_{s,1} = G_{s,11}(\varepsilon_s) + G_{s,12}(\varepsilon_s)\Delta_s + G_{s,13}(\varepsilon_s)\beta_s \quad (\text{B.18})$$

$$G_{s,2} = G_{s,21}(\varepsilon_s) + G_{s,22}(\varepsilon_s)\Delta_s + G_{s,23}(\varepsilon_s)\beta_s \quad (\text{B.19})$$

with $G_{s,ij}$ are the tabulated values shown Table. B.2, $i \in \{1, 2\}$ and $j \in \{1, 2, 3\}$.

In Eqn. (B.13), the term, $G_{s,1} a_s/b_s$, accounts for the circumsolar region, with

$$a_s = \max(0, \cos(\theta_s)) \quad (\text{B.20})$$

$$b_s = \max(\cos(85^\circ), \cos(\theta_s)) \quad (\text{B.21})$$

Together with Eqn. (B.12), (B.13), and (B.14), the governing equation for the diffuse solar incidence on an arbitrary surface is, $q''_{s,sky}$,

$$q''_{s,sky} = [R_{s,dome} + R_{s,circumsolar} + R_{s,horizon}] q''_{sky} \quad (B.22)$$

B.1.2c Ground Reflected Diffuse Solar Incidence

The diffuse ground reflected solar radiation, q''_{gnd} , is the sum of beam and diffuse sky solar irradiation reflected by the ground (ASHRAE, 2005):

$$q''_{gnd} = \rho_{s,gnd} \cdot q''_{beam} (C_s + \sin(\beta_s)) \{W/m^2\} \quad (B.23)$$

where

$\rho_{s,gnd}$ = ground reflectivity.

The ground reflected diffuse solar incidence on an arbitrary surface, $q''_{s,gnd}$, is the product of surface-to-ground view factor and diffuse reflected solar irradiation:

$$q''_{s,gnd} = F_{gnd} \cdot q''_{gnd} \quad (B.24)$$

with

$$VF_{surf,gnd} = \frac{1 - \cos(\Sigma)}{2} \quad (B.25)$$

The total incident solar radiation on a building exterior surface, $q''_{s,tot}$, is equal to the sum of the beam solar incidence, sky diffuse solar incidence, ground reflected diffuse solar incidence:

$$q''_{s,tot} = q''_{s,beam} + q''_{s,sky} + q''_{s,gnd} \{W/m^2\} \quad (B.26)$$

B.1.2d Solar Gain for Exterior Surfaces

The solar gain for exterior surfaces, $q''_{o,sol}$, is simply the absorbed total incident solar radiation (Eplus, 2011):

$$q''_{o,sol} = \alpha_{sol} \cdot q''_{s,tot} \quad (\text{B.27})$$

where α_{sol} is the solar absorptivity.

B.1.3 Solar Gain for Interior Surfaces

As mentioned above, shortwave solar radiation has two key components: the beam and diffuse solar radiation. In the presence of glazing, solar radiation incident on the glazing will be reflected, absorbed, or transmitted. The transmitted solar radiation will be absorbed by the interior surfaces. Depending on the surface condition, a portion of the solar radiation will be reflected and redistributed to other surfaces. In the absence of other shortwave radiation sources, such as interior lightings, the heat gain of an interior surface is the combination of the absorbed transmitted-solar-radiation and the absorbed reflected-solar-radiation. In this section, the calculation of the transmitted solar radiation, namely the transmitted beam solar radiation and the transmitted diffuse solar radiation, and the distribution of the transmitted solar radiation and reflected solar radiation will be presented.

In order to compute the transmitted solar radiation, the glazing optical properties will first have to be evaluated to determine the amount of solar radiation transmitted through. The angular dependent and hemispherical optical properties will be evaluated and the

evaluation used in this simulation is similar to WINDOW 4 (Finlayson et al., 1993). Note that, only an uncoated, spectral average, single-paned glazing is considered. For uncoated glasses, the reflectance in both sides is identical. For multi-paned glazing and coated windows, detailed description can be found in Furler (1991) and Finlayson et al. (1993).

B.1.3a Optical Properties for Glazing

Two glass optical properties, 1) transmittance at normal incidence, $T_{g,o}$, and 2) reflectance at normal incidence, $R_{g,o}$, are required to initiate the evaluation. The transmittance and the reflectance in any arbitrary angle, θ_g ranging from 0° to 90° , are related to the transmissivity and the reflectivity through the following relations (Furler, 1991):

$$T_{g,\theta_g} = \frac{\tau_{g,\theta_g}^2 e^{-\alpha d_g / \cos(\theta_g)}}{1 - \rho_{g,\theta_g}^2 e^{-2\alpha d_g / \cos(\theta_g)}} \quad (\text{B.28})$$

and

$$R_{g,\theta_g} = \rho_{g,\theta_g} \left(1 + T_{g,\theta_g} \cdot e^{-\alpha d_g / \cos(\theta_g)} \right) \quad (\text{B.29})$$

where d_g is the thickness of the glass. ρ_{g,θ_g} is the glass reflectivity and τ_{g,θ_g} is the glass transmissivity and their properties are defined below.

The angular dependent absorptance, A_{g,θ_g} , is given by:

$$A_{g,\theta_g} = 1 - R_{g,\theta_g} - T_{g,\theta_g} \quad (\text{B.30})$$

Using the Frensel's equations assuming unpolarized incident radiation, the reflectivity is calculated from:

$$\rho_{g,\theta_g} = \frac{1}{2} \left(\left(\frac{n \cdot \cos(\theta_g) - \sqrt{1 - \frac{1 - \cos^2(\theta_g)}{n^2}}}{n \cdot \cos(\theta_g) + \sqrt{1 - \frac{1 - \cos^2(\theta_g)}{n^2}}} \right)^2 + \left(\frac{n \cdot \sqrt{1 - \frac{1 - \cos^2(\theta_g)}{n^2}} - \cos(\theta_g)}{n \cdot \sqrt{1 - \frac{1 - \cos^2(\theta_g)}{n^2}} + \cos(\theta_g)} \right)^2 \right) \quad (\text{B.31})$$

where n is the ratio of glass index of refraction to air index of refraction and this transmissivity is calculated from the reflectivity such that:

$$\tau_{g,\theta_g} = 1 - \rho_{g,\theta_g} \quad (\text{B.32})$$

The index of refraction can be obtained by inverting a special form of Eqn. (B.31) evaluated at normal incidence:

$$n = \frac{1 + \sqrt{\rho_{g,o}}}{1 - \sqrt{\rho_{g,o}}} \quad (\text{B.33})$$

The spectral absorption coefficient, α , appeared in both Eqn. (B.28) and (B.29) is defined as:

$$\alpha = 4\pi\kappa_\lambda / \lambda \quad (\text{B.34})$$

where κ_λ is the dimensionless extinction coefficient and λ is the wavelength and κ_λ is evaluated in the following expression at normal incidence:

$$\kappa_\lambda = -\frac{\lambda}{4\pi d_g} \ln \frac{R_{g,o} - \rho_{g,o}}{\rho_{g,o} T_{g,o}} \quad (\text{B.35})$$

In order to solve for Eqn. (B.34) and (B.35), the reflectivity at normal incidence must be known and its value is determined by combining Eqn. (B.28) and (B.29) to eliminate the exponential factor, resulting in the following expressing:

$$\rho_{g,o} = \frac{\beta_g - \sqrt{\beta_g^2 - 4(2 - R_{g,o})R_{g,o}}}{2(2 - R_{g,o})} \quad (\text{B.36})$$

where

$$\beta_g = T_{g,o}^2 - R_{g,o}^2 + 2R_{g,o}^2 + 1 \quad (\text{B.37})$$

The transmittance and reflectance are obtained using the above equations for $\theta_g \in 0^\circ, 10^\circ, 20^\circ, \dots, 90^\circ$. A fourth order polynomial least square fit method is used to generate a correlation to recover the angular dependent properties at other angles. The hemispherical values are computed as:

$$T_{g,\cup} = 2 \int_0^{\frac{\pi}{2}} T_{g,\theta_g} \cos(\theta) \sin(\theta) d\theta = \int_0^{\frac{\pi}{2}} T_{g,\theta_g} \sin(2\theta) d\theta \quad (\text{B.38})$$

$$R_{g,\cup} = \int_0^{\frac{\pi}{2}} R_{g,\theta_g} \sin(2\theta) d\theta \quad (\text{B.39})$$

The above equations are integrated numerically using the trapezoidal rule.

B.1.3b Transmitted Solar Radiation

Given with the evaluated shortwave beam solar incidence in Eqn. (B.10) and shortwave diffuse solar incidence, including sky diffuse solar incidence in Eqn. (B.22) and ground reflected diffuse solar incidence in Eqn. (B.24), the transmitted beam solar radiation and

the transmitted diffuse solar radiation through a glazing can be obtained in the following expressions (Eplus, 2011):

$$q''_{ts,beam} = \tau_{g,\theta_g} q''_{s,beam} \quad (B.40)$$

$$q''_{ts,dif} = \tau_{g,\cup} (q''_{s,sky} + q''_{s,gnd}) \quad (B.41)$$

where τ_{g,θ_g} and $\tau_{g,\cup}$ is the directional transmittance and the hemispherical transmittance of the glazing evaluated in Eqn. (B.28) and Eqn. (B.29), respectively.

To compute the solar gains for an interior surface, we assume that all beam solar radiation entering the room first hits the floor and that the floor diffusely reflects the radiation to other surfaces. We neglect any multiple reflections and all reflected solar radiation is evenly distributed to other surfaces. For N number of glazing, the transmitted-beam-solar radiation absorbed by an arbitrary interior surface is modeled as follows (Eplus, 2011):

$$q''_{int,beam} = \frac{\alpha_{sol}}{A_{rec}} \cdot \sum_{i=1}^N \Omega_{sf} \cdot \tau_{g,\theta_g,i} \cdot A_{g,i} \cdot q''_{s,beam,i} \quad \{W / m^2\} \quad (B.42)$$

where α_{sol} is the surface solar absorptivity, A_{rec} is the area of receiving surface, A_g is the area of the glazing with Ω_{sf} , the fraction of beam radiation absorbed by each “floor” surface:

$$\Omega_{sf} = A_{floor} / A_{totfloor} \quad (B.43)$$

The transmitted-diffuse-solar radiation absorbed by an arbitrary interior surface is:

$$q''_{int,dif} = \frac{\alpha_{sol}}{A_{rec}} \cdot \sum_{i=1}^N F_{rec,i} \cdot \tau_{g,\cup,i} \cdot A_{g,i} \cdot (q''_{s,sky,i} + q''_{s,gnd,i}) \{W / m^2\} \quad (B.44)$$

where $F_{i,j}$ is the exact surface-to-surface direct exchange factor evaluated based on analytical expression from Siegel and Howell (2002).

The total reflected transmitted-solar-radiation absorbed is the sum of transmitted beam solar radiation and the sum of the transmitted diffuse solar radiation reflected by all interior surfaces (Eplus, 2011):

$$q''_{ref} = \sum_{i=1}^{N_{surf}} \frac{(1 - \alpha_{sol,i})}{\alpha_{sol,i}} (q''_{int,beam,i} + q''_{int,dif,i}) \quad (B.45)$$

The distribution factor that accounts for the reflected solar radiation distribution assumption is approximated by:

$$\Omega_{sd} = \frac{1}{\sum_{i=1}^{N_{surf}} A_i \alpha_{sol,i}} \quad (B.46)$$

Therefore, the total reflected transmitted-solar-radiation absorbed by an arbitrary interior surface is:

$$q''_{int,ref} = \Omega_{sd} q''_{ref} \quad (B.47)$$

Together, the total solar gain for an arbitrary interior surface, q''_{sol} , is equal to the sum of the absorbed transmitted-beam solar radiation, transmitted-diffused radiation, and total-reflected solar radiation:

$$q''_{sol} = q''_{int,beam} + q''_{int,dif} + q''_{int,ref} \quad (B.48)$$

B.2 Climate Condition

In this section, the calculation for the drybulb (air) temperature, sky temperature, ground temperature, as well as the local wind speed will be presented.

B.2.1 Drybulb Temperature

The daily maximum drybulb (db) temperature, $T_{db,max}$, temperature range, T_{range} , and hourly temperature variation profile, $T_{multiplier}$, are included in the weather profile. With these information, the db temperature for each hour, T_{db} , can be approximated as follows (Eplus, 2011):

$$T_{db} = T_{max} - T_{range} \cdot T_{multiplier} \quad \{\text{°C}\} \quad (\text{B.49})$$

An example of the hourly temperature variation profile can be found in Figure B.3. T_{db} in minutes can be obtained by the use of linear interpolation.

B.2.2 Sky Temperature

The sky temperature, T_{sky} , is approximated by the following correlation:

$$T_{sky} = \left(\frac{I_{Hori IR}}{\sigma} \right)^{\frac{1}{4}} - 273.15 \{\text{°C}\} \quad (\text{B.50})$$

where σ is the Stefan Boltzmann constant $\{5.667\text{E-}8 \text{ W/m}^2\text{K}^4\}$ and the horizontal infrared radiation intensity, $I_{Hori IR} \{\text{W/m}^2\}$.

B.2.3 Ground temperature

The monthly average ground temperature is provided in the weather file.

The drybulb, sky, and ground temperature will be used while the longwave radiative heat exchange between the ambient and the building exterior surfaces is being evaluated.

B.2.4 Local Wind Speed

The averaged local wind speed, V_z , at wall height z_v is calculated by applying terrain and height corrections to the measured wind speed V_{met} from a nearby meteorological station (ASHRAE, 2005):

$$V_z = V_{met} \left(\frac{\delta_{met}}{z_{met}} \right)^{\alpha_{met}} \left(\frac{z_v}{\delta_v} \right)^{\alpha_v} \quad \{\text{m/s}\} \quad (\text{B.51})$$

The wind boundary layer thickness, δ_v , and wind profile exponent, α_v , for the local building terrain, and δ_{met} and α_{met} for the meteorological station are determined from Table. B.3. V_{met} is generally measured at height, usually 10m above ground, in a flat and open terrain. In this regard, δ_{met} , α_{met} , and z_{met} is 270m, 0.14, and 10m, respectively (category 3 in Table. B.3).

B.3 Building Thermal Models

B.3.1 Conduction in Opaque Surfaces

Buildings are exposed to continuously changing solar radiation, ambient temperatures, and wind conditions. Since the building envelop has the capacity to store some amount

of heat, these unsteady conditions are moderated by the envelope and propagate with a time lag. As a result steady state calculation will not provide a realistic assessment of the building energy requirements. To compute the transient conductive heat flow in an element, we assume heat conduction in one dimension since the thickness of building surfaces is generally much smaller than the width and the height. The solution for the transient one dimensional conductive heat transfer (Seem, 1987):

$$q_{ki}'' = -Z_{CTF,0}T_i^t - \sum_{j=1}^{N_z} Z_{CTF,j}T_i^{t-j} + Y_{CTF,0}T_o^t + \sum_{j=1}^{N_z} Y_{CTF,j}T_o^{t-j} + \sum_{j=1}^{N_q} \Phi_{CTF,j}q_{ki}^{t-j} \quad (\text{B.52})$$

for the inside heat flux, and

$$q_{ko}'' = -Y_{CFT,0}T_i^t - \sum_{j=1}^{N_z} Y_{CFT,j}T_i^{t-j} + X_{CFT,0}T_o^t + \sum_{j=1}^{N_z} X_{CFT,j}T_o^{t-j} + \sum_{j=1}^{N_q} \Phi_{CFT,j}q_{ko}^{t-j} \quad (\text{B.53})$$

for the outside heat flux.

Eqn. (B.52) and (B.53) are the conduction transfer function solution for transient one dimensional conductive heat transfer. The X , Y , and Z are the CTF coefficients of outside, cross, and inside terms. The Φ is the history terms of CTF coefficients.

B.3.2 Convective Heat Transfer for Exterior Surfaces

Heat transfer from surface convection is modeled using the classical formulation (Eplus, 2011):

$$q_{o,c}'' = h_{o,c}(T_{air} - T_i) \quad (\text{B.54})$$

where

$q''_{o,c}$ = exterior convective heat flux

$h_{o,c}$ = exterior convective heat transfer coefficient

T_{air} = outdoor air temperature

T_o = exterior surface temperature.

The exterior convection is divided into two components: 1) natural convection and 2) forced convection. The natural convection model correlates the convection coefficient to the heat flow direction, the surface orientation, and the temperature difference between the surface and the air (Walton, 1983). The natural convection coefficient, h_n , is calculated as the followings:

$$h_n = \left\{ \begin{array}{l} 1.310 |T_{air} - T_{surf}|^{1/3}, \text{ for vertical surface} \\ \frac{9.482 |T_{air} - T_{surf}|^{1/3}}{7.283 - |\cos(\Sigma)|}, \text{ for horizontal surf., enhanced conv.} \\ \frac{1.810 |T_{air} - T_{surf}|^{1/3}}{1.382 + |\cos(\Sigma)|}, \text{ for horizontal. surf., reduced conv.} \end{array} \right\} \quad (B.55)$$

Enhanced convection indicates that the heat transfer is in the direction of the heat flow and reduced convection indicates that the heat transfer is on the opposite direction of the heat flow where Σ is the surface tilt angle.

The forced convection component, h_f , is modeled based on the Sparrow's correlation (1979):

$$h_f = 2.537W_f R_f \left(\frac{PV_z}{A} \right)^{\frac{1}{2}} \quad (\text{B.56})$$

where

R_f = surface roughness multiplier as shown in Table. B.4 (ASHRAE 1981)

P = parameter of the surface

A = area of the surface

V_z = local velocity on the surface

with the wind modification multiplier, W_f , given in (Walton 1981):

$$W_f = \begin{cases} 0.5, & \text{for } |\Psi_s - W_{dir}| > 100^\circ \\ 1, & \text{otherwise} \end{cases} \quad (\text{B.57})$$

for Ψ_s is the surface azimuth and W_{dir} is the wind direction.

The exterior convection coefficient, $h_{o,c}$, is the sum of the natural component and the forced component:

$$h_{o,c} = h_n + h_f \quad (\text{B.58})$$

B.3.3 Convective Heat Transfer for Interior Surfaces

The interior surface convection, $q''_{i,c}$, is modeled as:

$$q''_{i,c} = h_{i,c} (T_i - T_z) \quad (\text{B.59})$$

where

$h_{i,c}$ = interior convection coefficient

T_z = zone air temperature

Since we assume no wind in the interior, the interior convective heat transfer coefficient only takes into account for the natural convection. Therefore, $h_{i,c} = h_n$.

B.3.4 Radiative Heat Transfer on Exterior Surfaces

To calculate the longwave radiative flux exchange between the building exterior surfaces and the surrounding, we assume the surrounding as an enclosure with much larger area than the building surface. The enclosure is divided into 3 surfaces: air, sky, and ground. Assuming that the surroundings act as a blackbody, the heat exchange is (McClellan and Pedersen, 1997):

$$q''_{o,lr} = q''_{r,air} + q''_{r,sky} + q''_{r,gnd} \quad (\text{B.60})$$

Applying the Stefan-Boltzmann Law to each component yields:

$$q''_{o,lr} = \varepsilon\sigma F_{air} (T_{air}^4 - T_{surf}^4) + \varepsilon\sigma F_{sky} (T_{sky}^4 - T_{surf}^4) + \varepsilon\sigma F_{gnd} (T_{gnd}^4 - T_{surf}^4) \quad (\text{B.61})$$

where

ε = longwave emissivity of the surface

σ = Stefan-Boltzmann constant

F_{air} = air-to-surface view factor

F_{sky} = sky-to-surface view factor

F_{gnd} = ground-to-surface view factor

T_{surf} = exterior surface temperature

T_{air} = air temperature

T_{sky} = sky temperature

T_{gnd} = ground surface temperature

We linearize Eqn. (B.61) to obtain:

$$q''_{o,lr} = h_{r,air} (T_{air} - T_{surf}) + h_{r,sky} (T_{sky} - T_{surf}) + h_{r,gnd} (T_{gnd} - T_{surf}) \quad (\text{B.62})$$

with the linearized radiative heat transfer coefficient as:

$$h_{r,air} = \frac{\varepsilon \sigma F_{air} (T_{air}^4 - T_{surf}^4)}{(T_{air} - T_{surf})}$$
$$h_{r,sky} = \frac{\varepsilon \sigma F_{sky} (T_{sky}^4 - T_{surf}^4)}{(T_{sky} - T_{surf})} \quad (\text{B.63})$$
$$h_{r,gnd} = \frac{\varepsilon \sigma F_{gnd} (T_{gnd}^4 - T_{surf}^4)}{(T_{gnd} - T_{surf})}$$

List of Tables (Appendix B)

Table B1: Extraterrestrial solar irradiance and related data.....	B23
Table B2: Perez model coefficients for irradiance.....	B23
Table B3: Wind speed profile coefficients.....	B24
Table B4: Surface roughness multipliers	B24

Extraterrestrial Solar Irradiance and Related Data				
	$I_o, \{W/m^2\}$	$A_s, \{W/m^2\}$	$B_s, \{--\}$	$C_s, \{--\}$
Jan	1416	1202	0.141	0.103
Feb	1401	1187	0.142	0.104
Mar	1381	1164	0.149	0.109
Apr	1356	1130	0.164	0.120
May	1336	1106	0.177	0.130
June	1336	1092	0.185	0.137
July	1336	1093	0.186	0.138
Aug	1338	1107	0.182	0.134
Sep	1359	1136	0.165	0.121
Oct	1380	1166	0.152	0.111
Nov	1405	1190	0.144	0.106
Dec	1417	1204	0.141	0.103

Note: Data are for 21st day of each month during the base year of 1964.

Table B1: Extraterrestrial solar irradiance and related data (ASHRAE, 2009).

Perez Model Coefficients for Irradiance						
ϵ bin	G_{11}	G_{12}	G_{13}	G_{21}	G_{22}	G_{23}
$\epsilon < 1.065$	-0.0083117	0.5877285	-0.0620636	-0.0596012	0.0721249	-0.0220216
$1.065 < \epsilon < 1.230$	0.1299457	0.6825954	-0.1513752	-0.0189325	0.0659650	-0.0288748
$1.230 < \epsilon < 1.500$	0.3296958	0.4868735	-0.2210958	0.0554140	-0.0639588	-0.0260542
$1.500 < \epsilon < 1.950$	0.5682053	0.1874525	-0.2951290	0.1088631	-0.1519229	-0.0139754
$1.950 < \epsilon < 2.800$	0.8730280	-0.3920403	-0.3616149	0.2255647	-0.4620442	0.0012448
$2.800 < \epsilon < 4.500$	1.1326077	-1.2367284	-0.4118494	0.2877813	-0.8230357	0.0558651
$4.500 < \epsilon < 6.200$	1.0601591	-1.5999137	-0.3589221	0.2642124	-1.1272340	0.1310694
$6.200 < \epsilon$	0.6777470	-0.3272588	-0.2504286	0.1561313	-1.3765031	0.2506212

Table B2: Perez model coefficients for irradiance (Perez, 1990).

Wind Speed Profile Coefficients		
Terrain Description	Exponent, α {--}	Boundary Layer Thickness, δ {m}
<i>Flat, open country</i>	0.14	270
<i>Rough, wooded country</i>	0.22	370
<i>Towns and cities</i>	0.33	460
<i>Ocean</i>	0.10	210
<i>Urban, industrial, forest</i>	0.22	370

Table B3: Wind speed profile coefficients (ASHRAE, 2005).

Surface Roughness Multipliers		
Roughness Index	R_f	Example Material
<i>1 (Very Rough)</i>	2.17	Stucco
<i>2 (Rough)</i>	1.57	Brick
<i>3 (Medium Rough)</i>	1.52	Concrete
<i>4 (Medium Smooth)</i>	1.13	Clear pine
<i>5 (Smooth)</i>	1.11	Smooth Plaster
<i>6 (Very Smooth)</i>	1.00	Glass

Table B4: Surface roughness multipliers (ASHRAE, 2005).

List of Figures (Appendix B)

Figure B1: Solar angles corresponding to an arbitrary surface.....	B26
Figure B2: Schematic of sky solar radiance distribution components.....	B26
Figure B3: Daily temperature range multipliers	B27

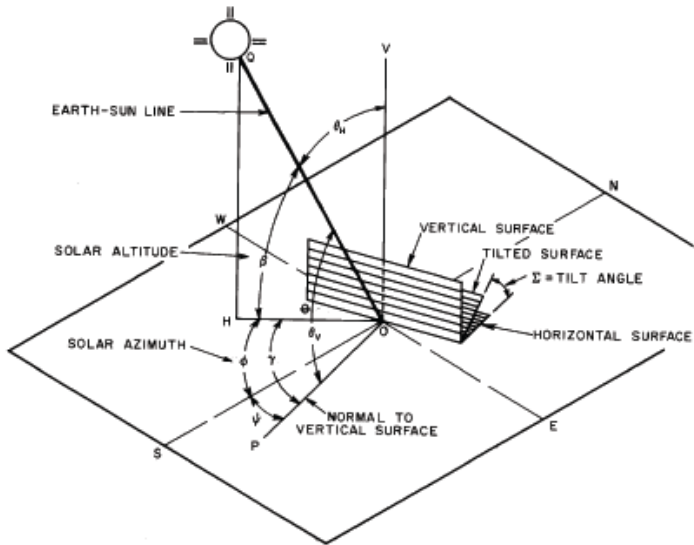


Figure B1: Solar angles corresponding to an arbitrary surface (ASHRAE, 2009).

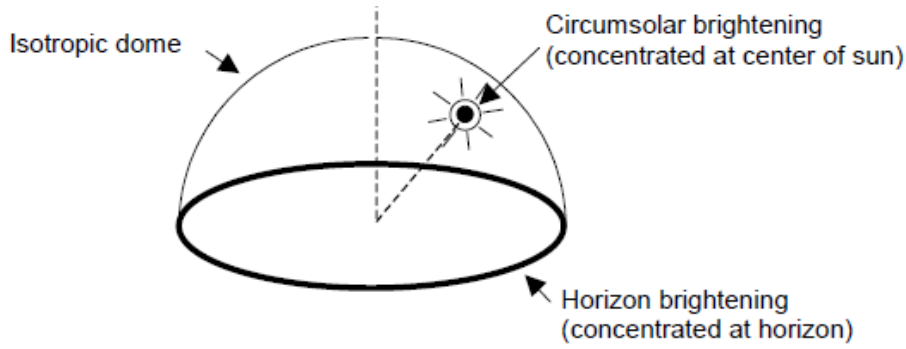


Figure B2: Schematic of sky solar radiance distribution components (Eplus, 2011).

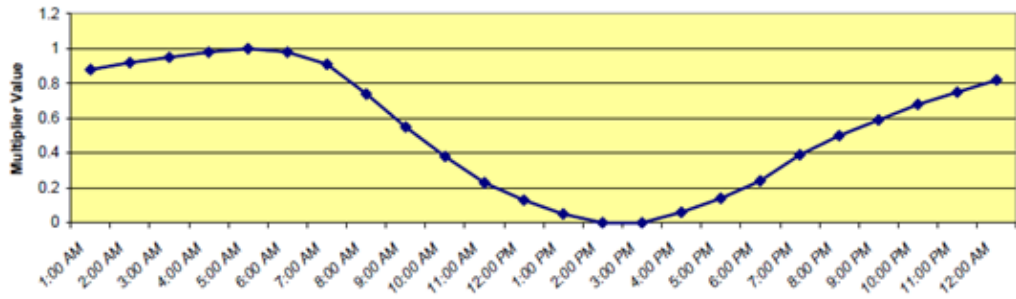


Figure B3: Daily temperature range multipliers (Eplus, 2011).